PHONON DYNAMICS AND THERMAL TRANSPORT IN SURFACE-DISORDERED NANOSTRUCTURES

by

Leon Nathaniel Maurer

A dissertation submitted in partial fulfillment of
the requirements for the degree of

Doctor of Philosophy

(Physics)

at the

UNIVERSITY OF WISCONSIN–MADISON

2016

Date of final oral examination: 8/1/2016

The dissertation is approved by the following members of the Final Oral Committee:
Irena Knezevic, Professor, Electrical & Computer Engineering
Mark A. Eriksson, Professor, Physics
Max G. Lagally, Professor, Material Science & Engineering
Maxim G. Vavilov, Professor, Physics
Michael J. Winokur, Professor, Physics

ACKNOWLEDGMENTS

This dissertation — the product of nearly eight years in the UW-Madison physics department — was only possible thanks to the help and support of those around me.

First and foremost, I would like to thank my advisor Irena Knezevic. I know of no other advisor who cares so much about the future of his or her graduate students. Irena, thank you for the guidance, support, and patience that made all of this research possible. I am especially grateful to Irena for giving me the opportunity to explore the uncharted lands of finite differences and chaotic phonons.

I would also like to thank our former postdoc Zlatan Aksamija. When I started in our group, I barely knew what a phonon was or why I should care. Zlatan helped me to get my bearings and showed me how humble lattice vibrations can do such cool things.

My groupmates have been a strong source of help and support. For much of my time here, Song Mei has been the other half our of group's phonon team, and she has been a great collaborator. I also owe a debt to Edwin Ramayya and Amirhossein Davoody for helping me get started with phonon Monte Carlo. In addition, let me thank my other groupmates, past and present: Alex Gabourie, Jason Hsu, Olafur Jonasson, Farhad Karimi, Bozidar Novakovic, Yanbing Shi, Sina Soleimanikahnoj, Nishant Sule, and Amanda ZuVerink.

Fortunately, there is more to life than research. I am grateful to my old friends and the many friends that I made in Madison — especially those in my entering class in the physics department. Friendships forged during Jackson problem sets are not easily broken. One of us had to be the last one out, and I look forward to joining you in the real world. The outdoors has always been my main escape from work, and hope to long remember the many friends I biked, hiked, camped, skied, paddled, and backpacked with.

Finally, I thank my family for their continuous support. My parents both survived grad school, and I would not have survived without their guidance. I also thank my girlfriend, Genya, for providing on-the-ground support and giving me something wonderful to look forward to after graduating.

TABLE OF CONTENTS

Page

Appendix

Page

LIST OF TABLES

LIST OF FIGURES

Figure Page

Appendix
Figure Page

Appendix
Figure Page

Appendix
Figure Page

Appendix
Figure Page

Appendix
Figure Page

Appendix
Figure Page

Appendix
Figure Page

NOMENCLATURE

Γ Scattering rate

Δ Root mean square (RMS) roughness

Δt Duration of simulation timestep

κ Thermal conductivity (due to phonons if not otherwise specified)

λ Lamé's first parameter

Λ Geometric Mean Free Path

μ Lamé's second parameter (also known as the shear modulus)

ξ Roughness correlation length

ρ Density

$\boldsymbol{\sigma}$ Strain tensor

$\boldsymbol{\tau}$ Stress tensor

τ Relaxation time or mean free time between scattering events (reciprocal of Γ)

ϕ Scalar potential

$\mathbf{\Psi}$ Vector potential

$\omega_{j,\mathbf{k}}$ Angular frequency of phonon in branch j with wave vector $\mathbf{k}$

A Area

c_l Longitudinal elastic wave velocity

c_t Transverse elastic wave velocity

$\mathcal{E}_i$ Total energy of phonons in cell i of a phonon Monte Carlo (PMC) simulation

h Grid cell size

j Index for phonon branch

$\mathbf{J}$ Heat-current density

$\mathbf{k}$ Wavevector

k_B Boltzmann's constant

L Length

$\hat{\mathbf{n}}$ Surface normal unit vector

$n_{\mathbf{BE}}$ Equilibrium phonon distribution function (Bose-Einstein distribution)

n_j Nonequilibrium phonon distribution function for phonon branch j

N_c Number of cells in a PMC simulation

$\mathcal{N}_i$ Number of phonons in cell i of a phonon Monte Carlo simulation

P Power

p Probability or probability distribution

$p_{\mathbf{GOE}}$ GOE (Wigner) distribution

$p_{\mathbf{P}}$ Poisson distribution

PR Participation ratio

$\mathbf{Q}$ Heat current

t Time

T Temperature

$\mathbf{u}$ Displacement

$\mathbf{v}$ Velocity

V Volume

W Ribbon or wire width

$\mathbf{x}$ Position

ABSTRACT

Nanoscale phonon transport is a developing field, made possible by recent advances in nanofabrication. The field has been driven primarily by the search for efficient thermoelectric devices, but the research has raised many questions that are interesting in their own right. In particular, experimental results have highlighted important gaps in our understanding of how disorder (especially surface disorder) affects phonon transport. This dissertation examines the effects of surface disorder on phonon dynamics through two different but complementary approaches.

The first approach is a phonon Monte Carlo (PMC) simulation, which treats phonons as semi-classical point particles that move through nanostructures and scatter in real space with random, rough surfaces. PMC proves to be an excellent tool for studying nanostructures of experimentally relevant sizes. We detail our PMC method, including improvements we have made over previous PMC simulations. We investigate why rough silicon nanowires (SiNWs) have measured thermal conductivities about two orders of magnitude lower than predicted and comparable to amorphous materials. The mechanism for this reduction remains an open question, but we show that it can be largely explained through scattering from rough surfaces, where extreme roughness causes a qualitative change in how phonons interact with boundaries.

During this project, we uncovered the utility of the geometric mean free path (GMFP), which is a concept developed in the study of chaotic billiards. The GMFP is the average distance a particle will travel between surface scattering events (in the absence of other scattering mechanisms), and we show that the thermal conductivities obtained from our PMC simulations are a function of the GMFP.

Our second approach for investigating the effects of surface disorder on phonon dynamics is to study two-dimensional elastic nanoribbons with finite-difference methods. Elastic materials make

good model systems for studying lattice dynamics because elastic materials capture wave behavior, and, in the long-wavelength limit, phonons behave like elastic waves. Our elastic-medium finite-difference time-domain simulation allows us to efficiently model relatively large structures while treating phonons as waves, rather than particles.

We develop a technique to calculate the thermal conductivity of elastic nanoribbons by coupling our finite-difference time-domain simulation with the Green-Kubo formula. We also employ a time-independent finite-difference method to solve for and study individual modes of our system. We find that rough surfaces can have an outsize impact on phonon dynamics. Surfaces do not simply scatter phonons; rough surfaces can also trap energy and cause all modes throughout the system to localize. The energy trapping and localization coincide with reduced thermal conductivity. We also investigate the effects of Rayleigh (surface) waves, a type of nonbulk mode that is missing from many phonon transport simulations, but which occurs naturally in our system.

Finally, we extend our use of time-independent finite-difference methods to search for signs of wave chaos in nanoribbons. We again find an interesting connection between the GMFP and thermal conductivity, which points the way towards future work.

Chapter 1

Introduction and Background

Recent interest in thermoelectric devices for energy generation has driven research into nanoscale phonon transport [12]. Phonons are quanta of energy in vibrational normal modes (lattice waves in the case of crystals) and are the dominant carriers of heat in semiconductors. While the study of phonons dates back to the late 1920s and the pioneering work of Rudolf Peierls [13, 14] and Igor Tamm [15, 16], much of the work since then has focused on bulk materials – not nanostructures. Phonon–surface scattering plays an important role in nanostructures, but the effects of surfaces are poorly understood. The interaction between phonons and surfaces was first modeled by Hendrik Casimir in the late 1930s [17], and his theory was extended by John Ziman and collaborators in the 1950s [18, 19]. Their model remains in use to this day because, until recently, it could explain most experimental results. However, experiments in the last decade on silicon nanowires (SiNWs) with intentionally roughened surfaces [20, 9] have produced results that are incompatible with Casimir's model.

The essence of Casimir's model and its descendants is that when a phonon encounters a surface, which is modeled as being flat, the phonon can either scatter specularly or diffusely. The case where all scattering is diffuse is known as the Casimir limit, which results in the most intense phonon–surface scattering possible in Casimir-like models. However, SiNW measurements demonstrated that phonon–surface scattering can cause thermal conductivities below the Casimir limit [20, 9].

There is still no framework suitable to replace Casimir's model. While advanced, atomistic phonon models exist (including atomistic Green's functions [21] and molecular dynamics [22, 1]),

most experimentally relevant nanostructures are too large to model using atomistic methods. The challenge is to develop models that can scale to large nanostructures but still capture the effects that are causing Casimir's model to fail. One of the most important challenges is to capture the effects of disorder in nanostructures — particularly the surface disorder that is critically important for understanding phonon dynamics in rough nanowires.

The theme of my research and this thesis is to better understand how surfaces affect phonons in nanostructures. We have developed two models suitable for large, surface-disordered nanostructures: a phonon Monte Carlo (PMC) model [23] and an elastic medium finite-difference time-domain (FDTD) model [24]. The two models complement each other: the former method considers the "ray optics" limit, where phonons are treated as semiclassical point particles, while the latter method treats phonons as classical waves.

We will start by providing a summary of my work and results. The remainder of this chapter will be a review of relevant physics and mathematics.

1.1 Summary of Results

In the first part of my work, we developed a phonon Monte Carlo simulation to model SiNWs of width 20-70 nm with real-space, correlated rough surfaces. We explain and document many of the important details and optimizations for the PMC method (Chapter 2), many of which are my original work and were published in a book chapter [25]. This work also was used in several projects in my group that made use of the PMC method [26, 8, 27].

We showed that [23], with real-space roughness, thermal conductivity well below the diffusive (Casimir) limit can be obtained for a wide range of roughness parameters (RMS roughness and correlation length) for Gaussian and exponential surface roughness autocorrelation functions. Our calculated thermal conductivity values for exponentially correlated surfaces are close to experimental results [9] for similar roughness parameters.

We introduced the normalized geometric mean free path (GMFP) $\bar{\Lambda}$ (with $0 < \bar{\Lambda} < 1$), which is related to the wire volume-to–surface area ratio and serves as a universal quantifier of roughness for a given correlation type. We find that thermal conductivities below the Casimir limit

correspond to $\bar{\Lambda} < 1/2$. With increasing roughness (decreasing $\bar{\Lambda}$), $\kappa(\bar{\Lambda})$ shows a crossover between exponential dependence at low-to-moderate roughness (high $\bar{\Lambda}$), where internal scattering randomly interrupts phonon bouncing across the NW, and linear dependence at high roughness (low $\bar{\Lambda}$), where multiple scattering events at the same surface dominate phonon transport and results in ultralow thermal conductivities. The linear dependence at high roughness can be captured through a simple relaxation rate. The results derived from the PMC simulation were published in [23].

In the second part of the work, we introduced a novel technique to calculate thermal conductivities in disordered nanostructures: a finite-difference time-domain solution of the elastic wave equation combined with the Green-Kubo formula. This combination of FDTD and Green-Kubo proves a versatile technique that captures phonon wave behavior and scales well to nanostructures that are too large or too surface disordered to simulate with many other techniques. We use related finite-difference methods to solve for individual normal modes so that we can compare the transport properties of the wire as a whole to the properties of the vibrational modes.

We use these techniques to study graphenelike nanoribbons with surface disorder. The ability to study wavelike behavior on a relatively large scale allows us to study the impact of Rayleigh (surface) waves. We investigate the role of Rayleigh waves and surface disorder on thermal transport by imposing free (allowing Rayleigh waves) and fixed (prohibiting Rayleigh waves) boundary conditions. We find that free edges result in a significantly lower thermal conductivity than fixed ones. By studying the vibrational modes, we see that free edges both introduce Rayleigh waves and cause all low-frequency modes (including bulk modes) to become more localized. Increasing surface disorder on free edges draws energy away from the center of the ribbon and toward the disordered edges, where the energy is less likely to propagate. These effects are not seen in ribbons with fixed boundary conditions and illustrate the importance of phonon surface modes in nanostructures. The results from my FDTD work are to be published in [24].

Finally, we study the normal modes of nanoribbons in more detail and find that ribbons with a range of edge roughness parameters effectively form chaotic cavities. (This work will soon be submitted for publication.) We also see a transition from nonchaotic to chaotic and from chaotic to

disordered behavior as the roughness parameters are varied. We also find an interesting relationship betwen the geometric mean free path and the thermal conductivity. We finish by investigating frequency-dependent properties of the cavities — setting the stage for future work.

1.1.1 Organization of Thesis

The remainder of this chapter provides relevant background for this thesis. Much of it reviews basic facts about phonons, but we emphasize some nonobvious connections between basic phonon models and my work, such as the connection between finite differences and phonon equations of motion. We also cover the two (equivalent) definitions of thermal conductivity that we use. Finally, we explain the properties and generation of rough surfaces, which are essential to the rest of my work.

Chapter 2 details the workings of our PMC simulation from generating random variates to the minutiae of conserving energy. We emphasize the flexibility of the PMC method by illustrating multiple solutions to several problems. We also highlight seemingly minor mistakes that can render the whole simulation unstable.

Chapter 3 reviews the physics of elastic continuum materials and finite-difference methods. We show how the FDTD method can be combined with the Green-Kubo formula to calculate the thermal conductivities of nanoribbons. We also note the relevance of elastic and elastic FDTD models to 2D materials.

Chapter 4 contains the main results of my work including sections on PMC results (Sec. 4.1), FDTD results (Sec. 4.2), and chaotic properties of nanoribbons (Sec. 4.3).

Chapter 5 is a brief conclusion that considers possibilities for future work.

1.2 Thermoelectricity and Thermoelectric Nanostructures

Although my work only applies to thermal transport, roughened SiNWs were developed in hopes that they would be good thermoelectric materials, so we provide a brief overview of thermoelectricity and thermoelectric nanostructures for context.

The thermoelectric effect was originally discovered as two different effects: the Seebeck effect (where a temperature gradient leads to an electrical voltage) and the Peltier effect (where an electrical current leads to a temperature difference). These two effects were later unified by Lord Kelvin [28] as a single thermoelectric effect.

The Seebeck effect can be understood as a diffusion process [29, 28]. An intuitive [29] (but wrong) model treats the charge carriers in the material as a classical gas. Consider an object with a temperature gradient across it. Charge carriers at the hot end will have more kinetic energy than charge carriers at the cold end. Consequently, more charge carriers will diffuse from the hot end to the cold end than vice versa, and an electrical voltage is created by the charge imbalance. This model is incorrect because the charge carriers follow Fermi-Dirac statistics, and a better model is that the temperature difference causes a difference in the chemical potential across the structure, and this difference in chemical potential causes the charge carriers to migrate from one side of the structure to the other [28]. The Peltier effect can be understood similarly.

The thermoelectric effect has several appealing applications. In particular, efficient thermoelectric materials could be a simple and cost-effective way to increase energy efficiency by capturing "waste heat". For example, internal combustion engines in cars send potentially recoverable energy out the tailpipe as heat; surrounding the tailpipe with thermoelectric materials could capture some of this thermal energy that would otherwise be wasted. Other applications include using the Peltier effect to make refrigerators without moving parts or dangerous refrigerants.

The problem is that cost-effective thermoelectric materials do not yet exist. Strictly speaking, all materials are thermoelectric materials, but the thermoelectric effect in most materials is extremely weak. The usefulness of a thermoelectric material is often judged by the dimensionless thermoelectric figure of merit

$$ZT = \frac{S^2 T \sigma}{\kappa}, \tag{1.1}$$

where S is the Seebeck coefficient, T is the absolute temperature, σ is the electrical conductivity, and κ is the thermal conductivity due to both electrons and phonons. A "good" thermoelectric material has $ZT > 1$.

The challenge is that, in many materials, S, σ, and κ are all closely related. In metals, almost all the heat is carried by electrons, so the thermal and electrical conductivities are closely linked by the Wiedemann-Franz law [29], which locks the ratio $^{T\sigma}/_{\kappa}$ to an unfavorable value.

So, we are limited to materials where the heat and charge are primarily carried by different particles, so that the thermal and electrical properties are largely decoupled. Semiconductors fit the bill because the heat in semiconductors is mostly carried by phonons, rather than electrons. The most efficient bulk thermoelectric materials are currently semiconductors that include rare and expensive elements such as tellurium, so there is an ongoing search for cheaper materials [30, 31].

One possible solution is to create semiconductor nanostructures that suppress phonon transport (reducing κ) without having a large impact on electrical transport [30, 20]. In semiconductors like silicon, phonons have a much longer mean free path (MFP) than electrons, so creating a SiNW with a diameter smaller than the phonon MFP, but larger than the electron MFP, should increase phonon scattering (thus lowering κ) while having little impact on the electrons. Silicon is an appealing material because it is cheap and we have decades of experience modeling and fabricating silicon devices.

Initial measurements of SiNWs showed thermal conductivities much lower than bulk silicon [32], but the reduction in κ was not large enough to make useful thermoelectric devices. However, later measurements on intentionally roughened SiNWs produced unexpectedly low thermal conductivities, close to the amorphous limit [31], resulting in $ZT \approx 1$ [20, 9]. However, no existing models could adequately explain the large drop in κ.

1.3 Phonons, the Continuum Limit, and Finite Differences

It is instructive to review a simple phonon model because, besides serving as a refresher, it shows connections between phonons, finite differences, and continuum mechanics that will be important later. The model is of a one-dimensional monoatomic lattice with periodic boundary conditions (described in [29, 33]). We begin with a classical description.

1.3.1 The Monoatomic 1D Lattice

Consider a chain of N point particles (atoms) connected by springs of equilibrium length h and spring constant K. Periodic boundary conditions connect the first and last particle, and the particles are restricted to move in one dimension, along the axis of the springs. The potential energy in this chain is

$$U = \frac{1}{2}K \sum_n \left[u\left(hn\right) - u\left(hn + h\right)\right]^2, \tag{1.2}$$

where $u\left(hn\right)$ is the displacement of the nth particle from its equilibrium position of hn. We use this somewhat cumbersome notation for reasons that will be clear shortly. The equations of motion are then

$$m\ddot{u}\left(hn\right) = -\frac{\partial U}{\partial u_n} = K\left[u\left(hn - h\right) - 2u\left(hn\right) + u\left(hn + h\right)\right]. \tag{1.3}$$

1.3.2 Finite Differences and the Continuum Limit

Note that the right side of Eq. (1.3) looks very similar to a finite difference for the second derivate. The second derivative of a function $f\left(x\right)$ is

$$\frac{\partial^2 f}{\partial x^2} = \lim_{h \to 0} \frac{f\left(x - h\right) - 2f\left(x\right) + f\left(x + h\right)}{h^2}, \tag{1.4}$$

and a finite difference is simply an approximation where h goes to a finite value instead of zero. A finite difference is a good approximation of a derivative if h is small relative to the length scale over which $f\left(x\right)$ varies. We will soon verify that the equation of motion has wavelike solutions, so u will vary over length scales similar to the wavelength. In other words, if the wavelength is much larger than h then the "finite difference" in Eq. (1.3) can be replaced with a second derivative to yield

$$\ddot{u} = \frac{h^2 K}{m} \frac{\partial^2 u}{\partial x^2}, \tag{1.5}$$

which is the form of a common scalar wave equation (seen, for example, in waves on a continuum string). The case where the wavelength is much larger than h is called the *continuum limit*.

These results indicate two things:

1. Long-wavelength waves in atomic materials behave like waves in continuum materials [29, 34].

2. Quadratic interatomic potentials result in equations similar to finite differences, as seen in Eq. (1.3), so finite differences can result in dispersion relations similar to those seen in atomic materials both inside and outside the continuum limit. (More in Secs. 1.3.3 and 3.2.1.2.)

1.3.3 Dispersion

To solve Eq. (1.3), we guess that solutions are of the form

$$u\left(x,t\right) \propto e^{i(kx-\omega t)}. \tag{1.6}$$

Substituting Eq. (1.6) into Eq. (1.3) yields

$$\begin{aligned} -m\omega^2 e^{i(khn-\omega t)} &= K\left[e^{i(k(n-1)h-\omega t)} - 2e^{i(knh-\omega t)} + e^{i(k(n+1)h-\omega t)}\right] \\ &= K\left(e^{-ikh} - 2 + e^{ikh}\right) e^{i(knh-\omega t)} \\ &= -2K\left(1-\cos kh\right) e^{i(knh-\omega t)}. \end{aligned} \tag{1.7}$$

Eliminating the time-dependent term and solving for ω yields a nonlinear dispersion relation

$$\omega = \sqrt{\frac{2K}{m}\left(1-\cos kh\right)} = 2\sqrt{\frac{K}{m}}\left|\sin {}^{kh}\!/_{2}\right|. \tag{1.8}$$

We will see a very similar dispersion relation arising from the FDTD method in Sec. 3.2.1.2.

In the limit where kh is small, the sine in Eq. (1.8) can be approximated away to yield

$$\omega = h\sqrt{\frac{K}{m}}\left|k\right|. \tag{1.9}$$

This is also the dispersion that results from the wave equation in Eq. (1.5), which should not be surprising since both Eq. (1.5) and Eq. (1.9) are in the long-wavelength (small-k) limit.

1.3.4 Higher Dimensions and Phonon Types

Since this example lattice is monoatomic, and the atoms move only in one dimension, there is only one dispersion relation. In lattices with more than one atom in each unit cell and atoms that can move in more than one dimension, there will be more dispersion relations, each corresponding to a different "type" (or branch) of phonon.

Acoustic branches have dispersion relations where $\lim_{|\mathbf{k}|\to 0} \omega_{\mathbf{k}} = 0$, but optical branches have dispersion relations that do not go to zero in that limit. (Optical phonons are present in crystals with more than one atom per unit cell.) Branches can also be classified by the motion of their atoms relative to the direction of propagation. Longitudinal branches have atoms that move roughly in the direction of the wavevector while transverse modes will have atoms that move roughly transverse to the wave vector.

The phonon group velocity for branch j is $\mathbf{v}_{j,\mathbf{k}} = \nabla_{\mathbf{k}} \omega_{j,\mathbf{k}}$, and acoustic phonons typically have the largest $|\mathbf{v}|$ at small $|\mathbf{k}|$ while optical phonons typically have a fairly flat dispersion relation, so the $|\mathbf{v}|$ is low for all optical phonons. Since optical phonons generally move slowly, they typically contribute little to the heat current and are often ignored in thermal transport problems.[1] In contrast, optical phonons are very important for calculating the heat capacity, since the optical phonons store energy even though they transport it slowly.

So far, we have just discussed phonons that are present in bulk materials, but there are numerous phonon modes at surfaces [35, 34], interfaces [36, 34], and in finite structures. Even a simple structure like a nanowire can have a great variety of structure-dependent modes, including dilatational, torsional, and bending modes [37, 38]. Moreover, there can be multiple dispersion relations for each type of structure-dependent mode: seven different edge modes have been identified in armchair graphene nanoribbons and twelve in zigzag graphene nanoribbons, in addition

[1] However, optical phonons are often important for phonon–phonon scattering and thus have an impact on the scattering rates for acoustic phonons. These scattering rates are included in thermal transport problems.

to multiple bending and twisting modes. Sometimes these modes do not interact with bulk modes, but sometimes they do, which can lead to phonon scattering.

Finally, there are also modes due to defects. Unlike the previously mentioned modes, defect modes are localized in space and cannot be associated with a dispersion curve. Still, these defect modes can be of great importance by trapping energy and causing extended modes to scatter [39, 40].

1.3.5 Quantization of Lattice Waves

So far, we have avoided the fact that lattice waves in real materials are quantized, but that simply goes to show that many properties of lattice waves (e.g., dispersion and branches) can be understood classically. For completeness, I review the quantum-mechanical treatment of the monoatomic lattice considered earlier. I largely follow the derivation from [33]. First we write the Hamiltonian with operators rather than classical positions

$$\hat{H} = \sum_n \frac{\hat{p}_n^2}{2m} + \sum_n \frac{K}{2} \left(\hat{u}_n - \hat{u}_{n-1}\right)^2, \tag{1.10}$$

where $\hat{u}_n$ is the operator for the displacement of the nth atom from its equilibrium position[2] and $\hat{p}_n$ is the momentum operator for the same particle.

We rewrite the Hamiltonian in terms of modes of the whole system rather than coordinates of the individual atoms. We again guess that the system has oscillatory solutions [just as we did for the classical problem in Eq. (1.6)]. We introduce new operators

$$\hat{P}_k = \frac{1}{\sqrt{N}} \sum_n e^{ikn} \hat{p}_n \Longleftrightarrow \hat{p}_n = \frac{1}{\sqrt{N}} \sum_k e^{-ikn} \hat{P}_k, \tag{1.11}$$

$$\hat{U}_k = \frac{1}{\sqrt{N}} \sum_n e^{ikn} \hat{u}_n \Longleftrightarrow \hat{u}_n = \frac{1}{\sqrt{N}} \sum_k e^{-ikn} \hat{U}_k. \tag{1.12}$$

We can then rewrite the Hamiltonian as

[2] We avoid the cumbersome notation of $\hat{u}\,(nh)$ because we no longer need to stress the similarity with a finite difference.

$$\hat{H} = \frac{1}{2m}\sum_k \hat{P}_k\hat{P}_{-k} + K\sum_k \hat{U}_k\hat{U}_{-k}\left(1-\cos k\right), \tag{1.13}$$

$$= \frac{1}{2}\sum_k \left(\frac{1}{m}\hat{P}_k\hat{P}_k^\dagger + 2K\left(1-\cos k\right)\hat{U}_k\hat{U}_k^\dagger\right), \tag{1.14}$$

where $\hat{U}_k^\dagger$ is the complex conjugate of $\hat{U}_k$, and $\hat{U}_k^\dagger = \hat{U}_{-k}$.

We define the annihilation and creation operators

$$\hat{a}_k = \sqrt{\frac{1}{2}m\hbar\omega\hat{a}_k}\hat{P}_k - i\sqrt{\frac{K\left(1-\cos k\right)}{\hbar\omega\hat{a}_k}}\hat{U}_k^\dagger, \tag{1.15}$$

$$\hat{a}_k^\dagger = \sqrt{\frac{1}{2}m\hbar\omega\hat{a}_k}\hat{P}_k^\dagger + i\sqrt{\frac{K\left(1-\cos k\right)}{\hbar\omega\hat{a}_k}}\hat{U}_k. \tag{1.16}$$

The interpretation is that our system can be thought of as independent vibrational modes and that these annihilation and creation operators act to remove or add quanta of energy (phonons) from the various modes. So, we can describe the system by how many quanta are in each mode $|n_0, n_1, n_2 \ldots\rangle$, where n_k is the number of phonons in the kth mode. The annihilation and creation operators act on only one mode at a time, so we can just write $|n_k\rangle$ if we only care about mode k.

The annihilation and creation operators have the usual properties

$$\hat{a}_k^\dagger\left|n_k\right\rangle = \sqrt{n_k+1}\left|n_k+1\right\rangle, \tag{1.17}$$

$$\hat{a}_k\left|n_k\right\rangle = \sqrt{n_k}\left|n_k-1\right\rangle, \tag{1.18}$$

and we also define the number operator $\hat{n}_k = \hat{a}_k^\dagger\hat{a}_k$, which has the property that $\hat{n}_k\left|n_k\right\rangle = n_k\left|n_k\right\rangle$

Finally, we can rewrite the Hamiltonian once more as

$$\hat{H} = \frac{1}{2}\sum_k \hbar\omega\left(\hat{a}_k^\dagger\hat{a}_k + \hat{a}_k\hat{a}_k^\dagger\right). \tag{1.19}$$

The total energy in the system is

$$E = \left\langle n_0, n_1, n_2 \ldots\right|\hat{H}\left|n_0, n_1, n_2 \ldots\right\rangle = \sum_k \left(n_k + \frac{1}{2}\right)\hbar\omega_k. \tag{1.20}$$

The interpretation is that the energy of the system is the total energy of all the phonons plus the zero-point energy in each mode ($\hbar\omega_k/2$). The zero-point energy cannot be extracted from the modes and thus will not contribute to transport.

1.3.6 Phonon Scattering in Bulk Materials

While it is convenient to treat a bulk material with harmonic potentials, this approximation leads to an infinite thermal conductivity [29, 33]; quadratic potentials allow for the superposition principle to hold, and waves can pass right through each other without interacting. As a consequence, any mode in the system will propagate forever without interruption. Real interatomic potentials are anharmonic, which leads to finite thermal conductivities in bulk materials.

Any interatomic potential can be expanded as [29]

$$U(\mathbf{x}) = U(\mathbf{0}) + \mathbf{x}\cdot\nabla\, U(\mathbf{x})|_{\mathbf{x}=\mathbf{0}} + \frac{1}{2!}(\mathbf{x}\cdot\nabla)^2\, U(\mathbf{x})|_{\mathbf{x}=\mathbf{0}} + \frac{1}{3!}(\mathbf{x}\cdot\nabla)^3\, U(\mathbf{x})|_{\mathbf{x}=\mathbf{0}} + \ldots, \quad (1.21)$$

where $\mathbf{x}$ is the displacement from the equilibrium atomic separation. The first term in the expansion is simply an offset that will not create a force. The second term in the expansion must be zero for $\mathbf{x} = \mathbf{0}$ to be an equilibrium position. The third term is the harmonic potential. All higher-order terms represent the anharmonicity.

In most cases, the displacement from equilibrium will be small, so higher-order terms are typically small. Anharmonic terms are then treated as perturbations to the harmonic term. We can see that a quadratic term in the potential leads to products of two annihilation/creation operators in the 1D Hamiltonian [Eq. (1.19)], and it turns out [33] that cubic terms lead to the product of three annihilation/creation operators (e.g., $\hat{a}_{\mathbf{k}_1,j_1}\hat{a}_{\mathbf{k}_2,j_2}\hat{a}^\dagger_{\mathbf{k}_3,j_3}$, where j_n is the branch), quartic terms lead to the product of four annihilation/creation operators, etc.

To calculate scattering rates caused by anharmonic terms, one turns to time-dependent perturbation theory and Fermi's golden rule [41]

$$S_{i\to f} = \frac{2\pi}{\hbar}\left|\langle i|\,\hat{H}'\,|f\rangle\right|^2 \delta(E_f - E_i), \quad (1.22)$$

where $S_{i\to f}$ is the transition rate from initial state $|i\rangle$ to final state $|f\rangle$ (both assumed to be eigenstates of $\hat{H}$), $\hat{H}'$ is the perturbing Hamiltonian (e.g., anharmonic terms), E_f is the energy of state $|f\rangle$, and E_i is the energy of state $|i\rangle$.

Often, only cubic terms are included in the perturbing Hamiltonian, so the transition rates include terms such as $\langle i|\,\hat{a}_{\mathbf{k}_1,j_1}\hat{a}_{\mathbf{k}_2,j_2}\hat{a}^\dagger_{\mathbf{k}_3,j_3}\,|f\rangle$, which are nonzero only for $\langle i| = \langle n_{\mathbf{k}_1,j_1}, n_{\mathbf{k}_2,j_2}, n_{\mathbf{k}_3,j_3}|$ and $|f\rangle = |n_{\mathbf{k}_1,j_1}-1, n_{\mathbf{k}_2,j_2}-1, n_{\mathbf{k}_3,j_3}+1\rangle$. In other words, the transition annihilates two phonons (one with wavevector $\mathbf{k}_1$ and branch j_1 and the other with wavevector $\mathbf{k}_2$ and branch j_2) and creates one phonon (with wavevector $\mathbf{k}_3$ and branch j_3). This can be thought of as a three-phonon process, where two phonons "merge" into a third. Likewise, other transitions allow for one phonon to "split" in two. Fig. 1.1 shows schematics of splitting and merging three-phonon processes.

Only some transitions are allowed because energy must be conserved and the crystal momentum must be conserved up to a reciprocal lattice vector [33]. For merging, necessary conditions are

$$0 = -\omega_{\mathbf{k}_0,j_0} - \omega_{\mathbf{k}_1,j_1} + \omega_{\mathbf{k}_2,j_2}, \tag{1.23}$$

$$\mathbf{g} = -\mathbf{k}_0 - \mathbf{k}_1 + \mathbf{k}_2, \tag{1.24}$$

where $\mathbf{g}$ is a reciprocal lattice vector. There are two important classes of three-phonon processes: those where $\mathbf{g} = \mathbf{0}$ (called normal scattering) and those where $\mathbf{g} \neq \mathbf{0}$ (called umklapp scattering).

Normal scattering has subtle effects because, in the absence of dispersion, the heat current[3] [42, 22, 43]

$$\begin{aligned}\mathbf{Q} &= \sum_{\mathbf{k},j} (\text{\# phonons}) \times (\text{Phonon energy}) \times (\text{Group velocity}), \\ &= \sum_{\mathbf{k},j} n_{\mathbf{k},j}\hbar\omega_{\mathbf{k},j}\mathbf{v}_{\mathbf{k},j}\end{aligned} \tag{1.25}$$

[3] $\mathbf{Q}$ has units of W · m. The heat current density $\mathbf{J}$ is the heat current per unit volume (units of $^{\mathrm{W}}/_{\mathrm{m}^2}$). The power flux P passing through a surface A is $P = \int_A \mathbf{J}\cdot d\mathbf{A}$. However, since we mostly consider quasi-1D structures, we will often treat $\mathbf{Q}$ as a scalar quantity because it will have only one nonzero component.

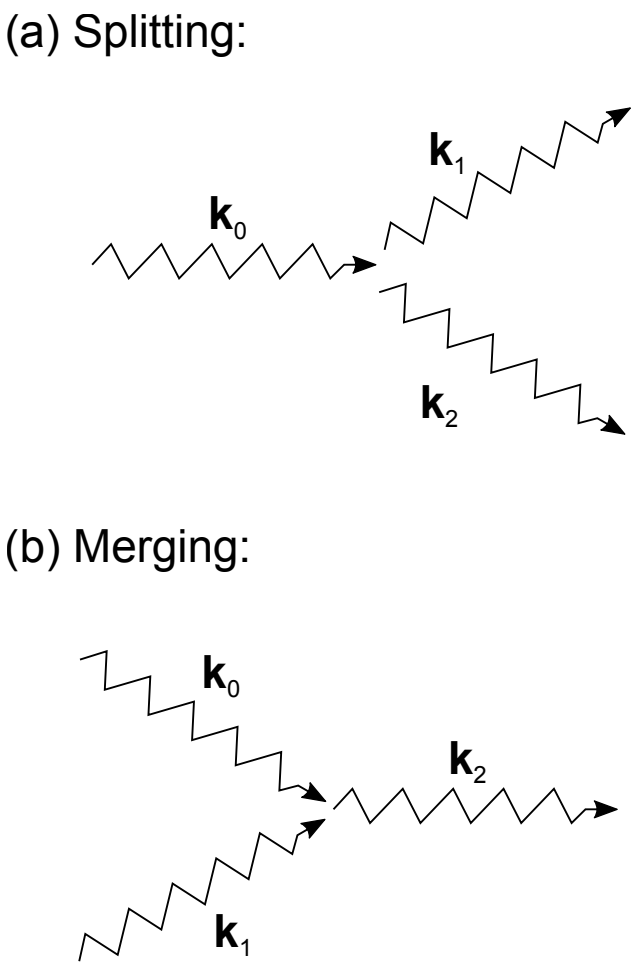

Figure 1.1: Schematics of splitting (a) and merging (b) three-phonon processes. $\mathbf{k}_0, \mathbf{k}_1, \mathbf{k}_2$ indicate the wavevectors of the three phonons. For splitting, $\mathbf{g} = -\mathbf{k}_0 + \mathbf{k}_1 + \mathbf{k}_2$, where $\mathbf{g}$ is a reciprocal lattice vector. For merging, $\mathbf{g} = -\mathbf{k}_0 - \mathbf{k}_1 + \mathbf{k}_2$.

is unchanged by normal scattering [33, 14]. However, normal scattering stills plays an important role in thermal conductivity because it can enhance umklapp (or other types of) scattering.

Scattering due to impurities, defects in the crystal lattice, etc., is handled with the same basic approach (time-dependent perturbation theory and Fermi's golden rule).

1.3.7 Diffuse Surface Scattering

The microscopic model of phonon–phonon scattering described in the previous section was developed during the birth of phonon transport models [13, 14], but it was not until about a decade latter that the first useful model of phonon–surface scattering was developed by Casimir [17]. Casimir's model was phenomenological and treated surfaces as blackbodies that absorbed all incident phonons before re-emitting them with a blackbody distribution.[4] Casimir was able to reduce this model to an effective relaxation time that could reproduce trends in experimental data.

Casimir's model was reinterpreted and extended by Ziman and collaborators in the 1950s [18, 19] by introducing the concept of a "specularity parameter", the probability that a phonon hitting a surface would scatter specularly; otherwise, the phonon would scatter diffusely. Again, this was a phenomenological model, but its adjustable specularity parameter made the model quite successful. The model was made somewhat more rigorous by having the specularity parameter be a function of the surface roughness and phonon wavevector [19, 2, 44].

However, all specularity-parameter models attempt to make flat surfaces mimic rough surfaces by randomizing the outgoing phonon momentum. This leads to the "Casimir limit" where all phonons are scattered diffusely. However, in the last decade, intentionally roughened SiNWs produced thermal conductivities far below the Casimir limit [20, 9], so it became clear that rough surfaces must do more than simply randomize outgoing phonon momentum.

[4] Casimir's model is equivalent to having each phonon scatter diffusely from the surface.

1.4 Thermal Conductivity

Since a large portion of this work is dedicated to finding thermal conductivities in quasi-1D structures, it is useful to define the thermal conductivity in the context of Fourier's law in one dimension for a structure with two contacts at different temperatures,

$$P = \kappa \frac{A\Delta T}{L}, \tag{1.26}$$

where P is the heat power flowing through a sample, κ is the thermal conductivity,[5] L is the length of the structure, A is the cross-sectional area of the structure, and ΔT is the temperature difference across the structure.[6]

While the definition is simple, there are several caveats. In general, the thermal conductivity is temperature dependent, so ΔT must be small enough that the thermal conductivity does not vary significantly throughout the structure. Having a large temperature gradient is also problematic because, strictly speaking, the temperature is only defined in equilibrium. A small temperature gradient will keep the position-dependent phonon distribution $n(\mathbf{k}, \mathbf{x})$ (phonon wavevector $\mathbf{k}$, position $\mathbf{x}$) similar to the equilibrium (Bose-Einstein) phonon distribution

$$n_{\mathrm{BE}}(\omega, T) = \frac{1}{e^{\hbar\omega/k_B T} - 1} \tag{1.27}$$

so that we can define an effective position-dependent temperature $T_{\mathbf{x}}$.

The second caveat is due to length effects. κ should be independent of L. Changing L in Eq. (1.26) should cause corresponding changes in P such that κ is constant. That does not happen in structures with finite length [19], and defining κ through Eq. (1.26) will mean that κ appears to be a function of length. However, κ should converge to a finite value as L goes to infinity. In practice, that means our simulation domains must be long enough that increasing L has little effect on the thermal conductivity.

[5] κ is actually a tensor since thermal conductivity can be anisotropic. However, we will treat κ as a scalar here since we only consider 1D structures or isotropic dispersion relations.

[6] Fourier's law can also be written $\mathbf{Q} = -\kappa \nabla T$ [42, 43].

We make the final requirement that the system must be in steady state so that any transient in $n_j(\mathbf{k}, \mathbf{x})$ is gone.

While Eq. (1.26) is, arguably, the most practical and commonly used definition of κ, we note that there is another definition of κ for a system in equilibrium using the Green-Kubo formula

$$\kappa = \frac{1}{k_B T^2 V} \int_0^\infty \langle Q(0)\, Q(t) \rangle \, dt, \tag{1.28}$$

where V is the volume of the sample, and

$$\langle Q(0)\, Q(t) \rangle = \int_{-\infty}^{\infty} Q(t')\, Q(t+t')\, dt' \tag{1.29}$$

is the heat-current autocorrelation function (HCACF).

The HCACF quantifies how the heat current in the system changes direction over time and "forgets" the direction it was flowing. This can be a hard concept to grasp, and I found it useful to see an autocorrelation function in a more familiar context. The Drude model of electrical conductivity assumes that the mean free time between electrons colliding with ions has a fixed value τ. While the Drude model is often derived with arguments about electrons being accelerated by an electric field and then colliding [45], the model can also be approached by assuming an electron velocity autocorrelation function of $\langle v(0)\, v(t) \rangle = e^{-t/\tau}$ (i.e., the electrons forget their previous velocity at a constant rate). The velocity autocorrelation is applied to an equation similar to Eq. (1.28), and the Drude electrical conductivity emerges [46].

The Green-Kubo formula avoids the problem of defining a temperature in a nonequilibrium system (since the formula is used for a system in equilibrium) but does not solve the problem of length effects and introduces an integral over an infinite time period. However, $\langle Q(0)\, Q(t) \rangle$ will tend to zero if κ is well defined, and the integral over t can be cut off at a finite time with little effect on κ. Figure 1.2 shows an example HCACF.

The two definitions of κ in Eqs. (1.26) and (1.28) prove to be equivalent in the limit where ΔT goes to zero.

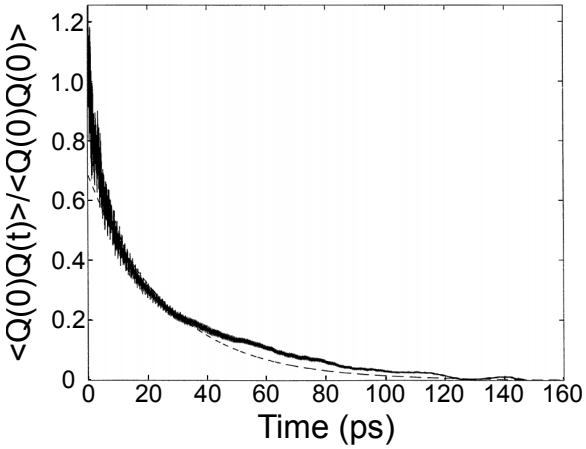

Figure 1.2: An example heat current autocorrelation function from a molecular dynamics simulation of crystalline β-SiC. The dashed line is an exponential decay for comparison. (Reprinted from [1] J. Nucl. Mater., 255, Li *et al.*, Atomistic modeling of finite-temperature properties of crystalline β-SiC, 139–152, Copyright (1998), with permission from Elsevier.)

We note that there is a third definition of conductance (and thus conductivity) using the relevant version of the Landauer formula [47], which defines the conductance in terms of the frequency-dependent transmission through a nanostructure [46]. However, we will not make use of this definition.

1.5 Rough Surfaces

The main focus of my work has been on the effects of rough surfaces, so it is important to understand how we model and generate rough surfaces. We assume that the roughness can be described by a single-valued function $z(\mathbf{x})$, which means that the surface cannot curve back on itself [Fig. 1.3(a)].[7]

A surface can be described by its autocorrelation function (ACF)

$$C(\mathbf{x}) = \int\int_S d^2\mathbf{x}' z(\mathbf{x}+\mathbf{x}')\, z(\mathbf{x}'), \tag{1.30}$$

which measures the relation between z at different points on the surface. We will consider two ACFs for roughness: the Gaussian ACF $C_g(\mathbf{x}) = \Delta^2 e^{-|\mathbf{x}|^2/\xi^2}$ and exponential ACF $C_e(\mathbf{x}) = \Delta^2 e^{-|\mathbf{x}|/\xi}$, where Δ is the RMS roughness (the characteristic height of surface features) and ξ is the correlation length (the characteristic width of surface features). Fig. 1.3 (b) illustrates Δ and ξ. Fig. 1.3 (c) and (d) show surfaces generated from Gaussian and exponential ACFs, respectively. For brevity, we will refer to them as Gaussian and exponential surfaces. The most striking difference between Gaussian and exponential surfaces is that exponential surfaces have much more short-scale roughness even though the large-scale features are similar.

We consider both Gaussian and exponential ACFs because both are widely used to model surface roughness. Most studies of phonon transport with surface disorder use either Gaussian [48, 49, 50, 51, 52] or Gaussian-based [53] ACFs. However, measurements of Si/SiO_2 interfaces found exponential [54] or exponential/Gaussian hybrid ACFs [55]. Hybrid ACFs have also been found on SiNWs [56, 9].

[7] Sometimes nanostructure surfaces do curve back on themselves [9], but this happens rarely so we do not consider it.

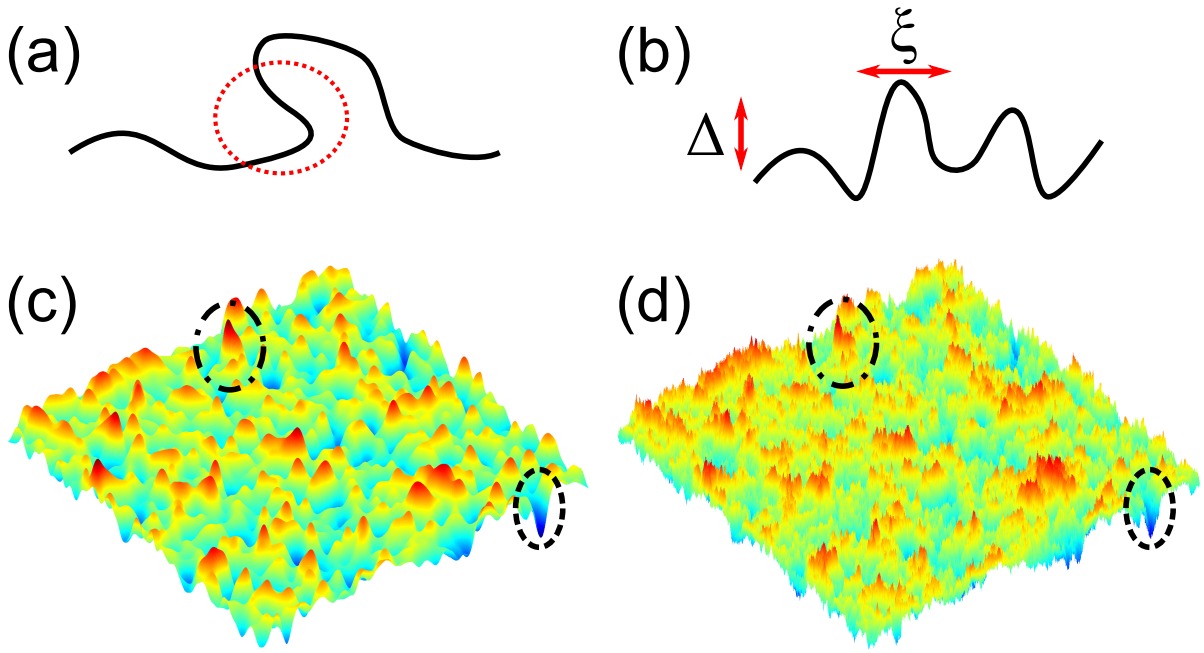

Figure 1.3: Illustrations of surface roughness. (a) A surface that "bends back on itself" and thus cannot be easily described with an ACF. (b) The RMS roughness Δ is the characteristic height of features on the surface while the correlation length ξ is the characteristic width of features. Surfaces generated from Gaussian (c) and exponential ACFs (d), respectively. Both surfaces were generated from the same set of random numbers and thus share the same large-scale features (e.g., compare the two pairs of circled features). However, it is clear that the exponential ACF leads to much more short-scale roughness.

It is straightforward to generate random surfaces from a given ACF $C(\mathbf{x})$ using Fourier transforms (denoted by $\mathcal{F}$) [26]. First, we define $z(\mathbf{p}) = \mathcal{F}(z(\mathbf{x}))$, which is the Fourier transform of the surface we desire. By the Wiener-Khinchin theorem [57], $\mathcal{F}(C(\mathbf{x})) = |z(\mathbf{p})|^2$. Now that we have $|z(\mathbf{p})|$, we can generate a random surface by multiplying in random phases $\Phi(\mathbf{p})$ and taking the inverse Fourier transform

$$z(\mathbf{x}) = \mathcal{F}^{-1}\left(|z(\mathbf{p})|\, e^{i\Phi(\mathbf{p})}\right). \tag{1.31}$$

The random phases $\Phi(\mathbf{p})$ take values $\in [0, 2\pi)$. $\Phi(\mathbf{p})$ must be an odd function in order for Eq. (1.31) to produce a real $z(\mathbf{x})$.[8]

In practice, the functions are all discretized for ease of computation, and the Fourier transform becomes a discrete Fourier transform (DFT) calculated with the Fast Fourier Transform algorithm. If we wish to generate a surface with $M \times N$ grid points, then the condition for the phases $\Phi_{i,j}$ to be odd are [26]

$$\begin{aligned}
\Phi_{0,0} = \Phi_{M/2,0} = \Phi_{0,N/2} = \Phi_{M/2,N/2} &= 0, \\
\Phi_{M-i,0} &= -\Phi_{i,0} \quad i = 1, 2, \ldots M/2 - 1, \\
\Phi_{0,N-j} &= -\Phi_{0,j} \quad j = 1, 2, \ldots N/2 - 1, \\
\Phi_{M-i,N-j} &= -\Phi_{i,j}.
\end{aligned} \tag{1.32}$$

These seemingly strange conditions are an artifact of how most computers compute DFTs and the order that they expect the array elements to be in.

The procedure is similar for generating a rough 1D edge.

1.6 Chaos

Chaos can take many forms, but generally, a dynamical system is considered "chaotic" if it is deterministic but has extreme sensitivity to initial conditions such that even a small change in the initial conditions leads to a significantly different state of the system at later times. We will be

[8] Another method that seems to work is to not require that $\Phi(\mathbf{p})$ is odd and then use $\mathrm{Re}\left(\sqrt{2}z(\mathbf{x})\right)$ as the surface. However, I have not tested this method thoroughly.

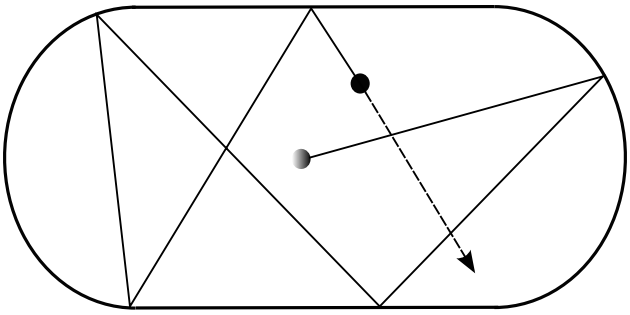

Figure 1.4: The Bunimovich stadium chaotic billiard. An example trajectory of a point particle is shown. (Modified from George Stamatiou CC BY 2.5 license.)

particularly interested in chaotic billiards (which results in ray chaos) [58] and the related concept of wave chaos [59].[9]

1.6.1 Chaotic Billiards

Chaotic billiards considers point particles, confined to some volume with zero potential (known as a "cavity" or "billiard"), that scatter specularly and elastically from the cavity's boundaries. Chaotic billiards are named for the similarity to billiard balls bouncing around a billiard table. However, a standard, rectangular billiard table is not chaotic: two particles with the same initial velocity but with slightly different initial positions will follow trajectories that parallel each other. If the particles were on a chaotic billiard, such as the Bunimovich stadium (Fig. 1.4), the positions of the two particles will initially separate exponentially, and their trajectories will become uncorrelated [58].[10] We note that any cavity with only piecewise flat boundaries cannot be chaotic, but computer simulations of nonchaotic cavities can introduce small errors that effectively make the cavities chaotic [60].

[9] Wave chaos is commonly known as "quantum chaos," because the Schrödinger equation was among the first wave equations to be considered. However, "quantum chaos" can be a confusing term because it applies to classical waves too [59]. For this reason, I will use the term "wave chaos".

[10] Note that there is a small set of initial conditions in the Bunimovich stadium where there will not be exponential separation: trajectories that bounce straight up and down between the flat sides of the stadium. However, almost all other trajectories show exponential separation.

For our purposes, the most useful concept from the study of ray chaos is the geometric mean free path (GMFP) Λ, which is the average distance a particle will travel between surface scattering events. There are simple, exact equations for the GMFP [58, 61]. In 3D

$$\Lambda_{\text{3D}} = \frac{4V}{A_s}, \tag{1.33}$$

where V is the cavity volume, and A_s is the surface area of the cavity boundary. In 2D

$$\Lambda_{\text{2D}} = \frac{\pi A}{L}, \tag{1.34}$$

where A is the area of the cavity, and L is the length of the perimeter of the cavity.

These formulas hold not only for chaotic billiards but also for an ensemble of particles in a nonchaotic cavity.

In some cases, these GMFPs can act like mean free paths in the relaxation-time approximation. In fact, the formula for Λ_{3D} was discovered experimentally in acoustics when researchers noticed that the relaxation time of sound in a populated or irregularly shaped auditorium is [62]

$$\tau = \frac{\Lambda_{\text{3D}}}{v\alpha}, \tag{1.35}$$

where v is the speed of sound and α represents the absorptivity of the auditorium walls.

The transport properties of chaotic billiards have also been studied numerically, but the results are not fully understood. Many of the studies have been on quasi-1D billiard channels — basically narrow, 2D ribbons with patterned edges. Both chaotic and certain nonchaotic channels can result in well-defined thermal conductivities [63, 64, 65, 66, 67], but the conditions for nonchaotic cavities to result in well-defined thermal conductivities are not fully understood. The takeaway is that specular, elastic surface scattering alone can lead to finite thermal conductivities.

1.6.2 Wave Chaos and Random Matrix Theory

Wave chaos is the study of waves in chaotic cavities and is a natural extension of chaotic billiards since point particles have the same dynamics as waves with vanishingly short wavelengths

(rays). Some of the first wave-chaos experiments were done with electrons and stadium-shaped quantum dots [68] taking the place of point particles and billiard tables. The electrons have relatively small wavelengths, so wave chaos was mostly a correction to point-particle-like dynamics. However, wave chaos applies to waves of all wavelengths, and the cavity shape has interesting consequences for long-wavelength modes, which have little in common with point particles. In particular, many properties of wave-chaotic systems follow the predictions of random matrix theory (RMT).

RMT was initially developed to study the properties of atomic nuclei. The idea was that the nuclei of large atoms were too complicated to model directly but that many statistical properties of nuclear spectra would match the statistical properties of certain ensembles of random matrices. One of the most famous results from RMT is the distribution of nearest-neighbor level spacings ("level spacings" for brevity). Two modes (with frequencies f_0 and f_1) are nearest neighbors if no other modes have a frequency $\in [f_0, f_1]$, and the nearest-neighbor level spacing is the difference in frequency (or energy) between nearest neighbors. For the Gaussian Orthogonal Ensemble (GOE) of random matrices, which is appropriate for systems with time-reversal symmetry, the level-spacing probability closely follows the Wigner distribution[11]

$$p_{\text{GOE}}(s) = \frac{\pi}{2} s e^{-\pi s^2/4}. \tag{1.36}$$

where s is the spacing between levels (normalized so that average spacing between neighboring levels is 1). We will refer to Eq. (1.36) as the "GOE distribution".[12] In other words, the probability of two neighboring levels being separated by s is $p(s)\,ds$. The GOE distribution peaks at $s = \sqrt{2/\pi}$, which is an effect of level repulsion.

In contrast, if the mode frequencies were drawn from a uniform random distribution (no level repulsion), then the level spacings follows a Poisson distribution

[11] There actually is not a closed-form solution for the level-spacing distribution of the GOE, but the Wigner distribution is an excellent fit to the real distribution.

[12] Using the "GOE distribution" instead of the "Wigner distribution" avoids confusion with the Wigner quasi-probability distribution.

$$p_{\mathrm{P}}(s) = e^{-s}. \tag{1.37}$$

Many types of nonchaotic systems have a Poisson distribution of level spacings. In specific, "integrable" systems have a Poisson distribution of level spacings [59]. We will not define the term "integrable" here and will instead simply note that ribbons with straight edges and wires with square or circular cross sections are integrable.

Although RMT was developed for atomic nuclei, it has been postulated that all chaotic systems with discrete modes will have properties matching the predictions of RMT [69]. This is an example of a universal property of chaos, and it is these universal properties that make chaos theory so useful.

We will further elaborate on wave chaos in Sec. 4.3.

Chapter 2

Phonon Monte Carlo Method

The purpose of this chapter is both to give an overview of the phonon Monte Carlo method and a number of important implementation details. While the overall method is mature and the general approach is well documented [70, 71, 4, 72, 73, 26, 27, 74], there are many important details and optimizations that are often left out of the literature — especially with regards to random variate generation, energy conservation, and surface scattering. I have documented many of these details in a forthcoming book chapter [25] (and to a lesser degree in several papers [26, 27, 8, 23]).

I begin with an overview of the phonon Boltzmann transport equation and phonon Monte Carlo method. Next, I review methods for generating random variates and put the methods to use efficiently and accurately generating and scattering phonons. I also note similarities between phonon generation and scattering with an eye towards reusing code in simulations. I also consider energy conservation. Finally, I comment on methods for normal scattering.

2.1 The Phonon Boltzmann Transport Equation

The phonon Boltzmann transport equation (PBTE)[1] is the basis for the oldest and, arguably, most successful method for calculating κ. The PBTE treats phonons as semiclassical particles that diffuse and scatter like particles in the original Boltzmann Transport equation [13, 14, 33]. While phonons are waves, approximating them as particles is justified for time scales longer than the

[1] Also known as as the Peierls-Boltzmann phonon transport equation.

relaxation time and length scales longer than the coherence length. A particle model is effectively the same as the ray limit, where the wavelength goes to zero.[2]

The PBTE,

$$\frac{\partial n_j(\mathbf{k},\mathbf{x},t)}{\partial t} + \mathbf{v}_{j,\mathbf{k}} \cdot \nabla_{\mathbf{x}} n_j(\mathbf{k},\mathbf{x},t) = \left.\frac{\partial n_j(\mathbf{k},\mathbf{x},t)}{\partial t}\right|_{\text{scatt}}, \tag{2.1}$$

gives the time evolution of the position-and-time-dependent phonon distribution function, $n_j(\mathbf{k},\mathbf{x},t)$, for branch j. The middle term captures particle diffusion while the right side captures changes to $n_j(\mathbf{k},\mathbf{x},t)$ due to scattering.[3] In steady state, the leftmost term is zero, so that the scattering and diffusion terms must balance

$$\mathbf{v}_{j,\mathbf{k}} \cdot \nabla_{\mathbf{x}} n_j(\mathbf{k},\mathbf{x},t) = \left.\frac{\partial n_j(\mathbf{k},\mathbf{x},t)}{\partial t}\right|_{\text{scatt}}. \tag{2.2}$$

If we can find $n_j(\mathbf{k},\mathbf{x},t)$, then it is straightforward to find the heat current density as [42]

$$\begin{aligned}\mathbf{J}(\mathbf{x},t) &= \sum_{\text{all modes}} (\text{\# of phonons in mode per unit volume}) \times (\text{phonon energy}) \times (\text{phonon velocity}) \\ &= \frac{1}{V}\sum_{\mathbf{k},j} n_j(\mathbf{k},\mathbf{x},t)\,\hbar\omega_{j,\mathbf{k}}\mathbf{v}_j.\end{aligned} \tag{2.3}$$

The heat current in a sample of volume V is $\mathbf{Q} = \int_V \mathbf{J}\cdot dV$, and the heat power flowing through a surface A is $P = \int_A \mathbf{J}\cdot d\mathbf{A}$.

The scattering term in Eq. (2.1) can be written in terms of the scattering rates calculated with Fermi's golden rule [41] (Sec. 1.3.6). However, the resulting integro-differential equation is very difficult to solve, so direct solutions are rarely attempted in phonon transport problems.

[2]It may seem counterintuitive that point particles behave the same as rays, which we often think of as lines or curves, but point particles can travel and scatter in the same way as rays. For this reason, particle models are often used in ray-propagation problems [75].

[3]For charged particles, the equivalent Boltzmann transport equation will have an additional "force" or "drift" term caused by electric or magnetic fields, but there is no force term for phonons.

2.1.1 The Linearized Phonon Boltzmann Transport Equation and the Relaxation-Time Approximation

In general, the PBTE can only be solved numerically, so before the advent of sufficiently powerful computers, various approximations were made to solve Eq. (2.2). It is instructive to consider one of the most common and successful approximations: linearizing the PBTE and using the relaxation-time approximation (RTA). The most important takeaway from this exercise is that the PBTE can lead to a well-defined κ in accordance with Fourier's law. We will also find it useful to compare our results to those from the RTA.

We assume that $n_j\left(\mathbf{k},\mathbf{x},t\right)$ differs only slightly from the equilibrium distribution $n_{\text{BE}}\left(\omega_{j,\mathbf{k}},T_{\mathbf{x}}\right)$, where $T_{\mathbf{x}}$ is the position-dependent effective temperature. It then makes sense to write

$$n_j\left(\mathbf{k},\mathbf{x},t\right)=n_{\text{BE}}\left(\omega_{j,\mathbf{k}},T_{\mathbf{x}}\right)+n'_j\left(\mathbf{k},\mathbf{x},t\right), \tag{2.4}$$

where $n'_j\left(\mathbf{k},\mathbf{x},t\right)$ is the departure from equilibrium.

For transport purposes, only $n'_j\left(\mathbf{k},\mathbf{x},t\right)$ matters because $n_{\text{BE}}\left(\omega_{j,\mathbf{k}},T_{\mathbf{x}}\right)$ is symmetric with respect to $\mathbf{k}$ [$n_{\text{BE}}\left(\omega_{j,\mathbf{k}},T_{\mathbf{x}}\right)$ has just as many phonons traveling left as right], so $n_{\text{BE}}\left(\omega_{j,\mathbf{k}},T_{\mathbf{x}}\right)$ drops out of the sum

$$\begin{aligned}\mathbf{J}\left(\mathbf{x},t\right)&=\frac{1}{V}\sum_{\mathbf{k},j}n_j\left(\mathbf{k},\mathbf{x},t\right)\hbar\omega_{j,\mathbf{k}}\mathbf{v}_j\\&=\frac{1}{V}\sum_{\mathbf{k},j}\left[n_{\text{BE}}\left(\omega_{j,\mathbf{k}},T_{\mathbf{x}}\right)+n'_j\left(\mathbf{k},\mathbf{x},t\right)\right]\hbar\omega_{j,\mathbf{k}}\mathbf{v}_j\\&=\frac{1}{V}\sum_{\mathbf{k},j}n'_j\left(\mathbf{k},\mathbf{x},t\right)\hbar\omega_{j,\mathbf{k}}\mathbf{v}_j.\end{aligned} \tag{2.5}$$

Since we assume that $n'_j\left(\mathbf{k},\mathbf{x},t\right)$ is small, on the *left* side of Eq. (2.2) we make the approximation

$$\begin{aligned}\mathbf{v}_{j,\mathbf{k}} \cdot \nabla_{\mathbf{x}} n_j\left(\mathbf{k}, \mathbf{x}, t\right) &\approx \mathbf{v}_{j,\mathbf{k}} \cdot \nabla_{\mathbf{x}} n_{\mathrm{BE}}\left(\omega_{j,\mathbf{k}}, T_{\mathbf{x}}\right) \\ &= \frac{\partial n_{\mathrm{BE}}\left(\omega_{j,\mathbf{k}}, T\right)}{\partial T} \mathbf{v}_{j,\mathbf{k}} \cdot \nabla_{\mathbf{x}} T_{\mathbf{x}} \\ &= \frac{\partial n_{\mathrm{BE}}\left(\omega_{j,\mathbf{k}}, T\right)}{\partial T} \mathbf{v}_{j,\mathbf{k}} \cdot \hat{\mathbf{x}} \frac{\Delta T}{L}.\end{aligned} \tag{2.6}$$

In the last step we assumed that the temperature gradient is constant in $\hat{\mathbf{x}}$, so the gradient is simply the temperature difference across the sample ΔT divided by the length of the sample L.

The RTA assumes that scattering causes $n_j\left(\mathbf{k}, \mathbf{x}, t\right)$ to "relax" towards $n_{\mathrm{BE}}\left(\omega_{j,\mathbf{k}}, T_{\mathbf{x}}\right)$ at a rate $\tau_{j,\mathbf{k}}^{-1}$ [42]

$$\left.\frac{\partial n_j\left(\mathbf{k}, \mathbf{x}, t\right)}{\partial t}\right|_{\text{scatt}} = \frac{n_{\mathrm{BE}}\left(\omega_{j,\mathbf{k}}, T_{\mathbf{x}}\right) - n_j\left(\mathbf{k}, \mathbf{x}, t\right)}{\tau_{j,\mathbf{k}}} = \frac{n_j'\left(\mathbf{k}, \mathbf{x}, t\right)}{\tau_{j,\mathbf{k}}}. \tag{2.7}$$

Applying the approximations in Eqs. 2.6 and 2.7 to Eq. 2.2 yields

$$\begin{aligned}\frac{n_j'\left(\mathbf{k}, \mathbf{x}, t\right)}{\tau_{j,\mathbf{k}}} &= \mathbf{v}_{j,\mathbf{k}} \cdot \hat{\mathbf{x}} \frac{\Delta T}{L} \frac{\partial n_{\mathrm{BE}}\left(\omega_{j,\mathbf{k}}, T\right)}{\partial T} \\ n_j'\left(\mathbf{k}, \mathbf{x}, t\right) &= \tau_{j,\mathbf{k}} \mathbf{v}_{j,\mathbf{k}} \cdot \hat{\mathbf{x}} \frac{\Delta T}{L} \frac{\partial n_{\mathrm{BE}}\left(\omega_{j,\mathbf{k}}, T\right)}{\partial T}.\end{aligned} \tag{2.8}$$

Putting that result into Eq. (2.5) and integrating over the cross-sectional area of the sample A yields P

$$\begin{aligned}P &= \int_A \mathbf{J} \cdot d\mathbf{A} \\ &= \frac{A\Delta T}{L} \frac{1}{V} \sum_{\mathbf{k},j} \tau_{j,\mathbf{k}} \left|\mathbf{v}_{j,\mathbf{k}}\right| \cos\left(\theta\right) \hbar\omega_{j,\mathbf{k}} \frac{\partial n_{\mathrm{BE}}\left(\omega_{j,\mathbf{k}}, T\right)}{\partial T} \mathbf{v}_{j,\mathbf{k}} \\ &= \frac{A\Delta T}{L} \frac{1}{V} \sum_{\mathbf{k},j} \tau_{j,\mathbf{k}} \left|\mathbf{v}_{j,\mathbf{k}}\right|^2 \cos^2\left(\theta\right) \hbar\omega_{j,\mathbf{k}} \frac{\partial n_{\mathrm{BE}}\left(\omega_{j,\mathbf{k}}, T\right)}{\partial T}\end{aligned} \tag{2.9}$$

where θ is the angle between $\mathbf{k}$ and $\hat{\mathbf{x}}$, and P is the heat power folowing through the sample.

Comparing with the definition of κ from Eq. (1.26) shows

$$\kappa = \frac{1}{V} \sum_{\mathbf{k},j} \tau_{j,\mathbf{k}} \left|\mathbf{v}_{j,\mathbf{k}}\right|^2 \cos^2\left(\theta\right) \hbar\omega_{j,\mathbf{k}} \frac{\partial n_{\mathrm{BE}}\left(\omega_{j,\mathbf{k}}, T\right)}{\partial T}. \tag{2.10}$$

Using the substitution $\sum_{\mathbf{k}} \rightarrow {}^{V}/_{(2\pi)^3} \int d^3\mathbf{k}$, Eq. (2.10) becomes

$$\kappa = \frac{1}{(2\pi)^3} \sum_j \int d^3\mathbf{k} \tau_{j,\mathbf{k}} \left|\mathbf{v}_{j,\mathbf{k}}\right|^2 \cos^2(\theta) \hbar\omega_{j,\mathbf{k}} \frac{\partial n_{\mathrm{BE}}(\omega_{j,\mathbf{k}}, T)}{\partial T}. \tag{2.11}$$

2.2 Overview of Phonon Monte Carlo

PMC is a method to solve the PBTE, and the PMC method is true to the essence of the PBTE. The PBTE treats the phonons as semiclassical particles that fly and scatter in real space, and that is exactly what happens in a PMC simulation. The simulation tracks an ensemble of phonons as they move through the simulation domain, and we can find $\mathbf{Q}$ simply by adding up the contributions from each phonon in the system.

An advantage of PMC is that it can model devices of practically any shape and size. PMC can easily handle different device geometries since the phonons are tracked in real space. PMC can also handle large structures in part because one phonon in the simulation can represent many phonons in the actual structure, so even a large nanostructure can be modeled with a reasonable number of simulated phonons.

In PMC simulations, it is common to only track acoustic phonons because optical phonons usually transport little heat due to their slow speed (Sec. 1.3.4). (However, in certain situations, optical phonons can contribute significantly to κ [76].) In acoustic branches, the phonon dispersion is often relatively isotropic, and an analytical isotropic phonon dispersion ($\omega_{j,\mathbf{k}}$ depends only on $|\mathbf{k}|$) can be adopted for simplicity. A quadratic isotropic dispersion[4] has been shown to be very accurate in simulating the thermal properties of silicon [71, 77, 26]. I will only consider isotropic dispersion relations here but it is possible to use full dispersion relations with PMC [8], which can be advantageous in very anisotropic materials such as graphene.

Figure 2.2 outlines a typical PMC simulation. The contents of the red box are the actions that make up a single time step.

[4] $\omega_{j,\mathbf{k}} = c_j k + d_j k^2$, where $k = |\mathbf{k}| \in [0, k_{\max}]$ is the allowed wavenumber, c_j is the speed of sound in the continuum limit, and d_j is a quadratic coefficient fitted from the full dispersion. The maximum allowed wavenumber $k_{\max}$ is $\frac{2\pi}{a_0}$, where a_0 is the lattice constant of the material.

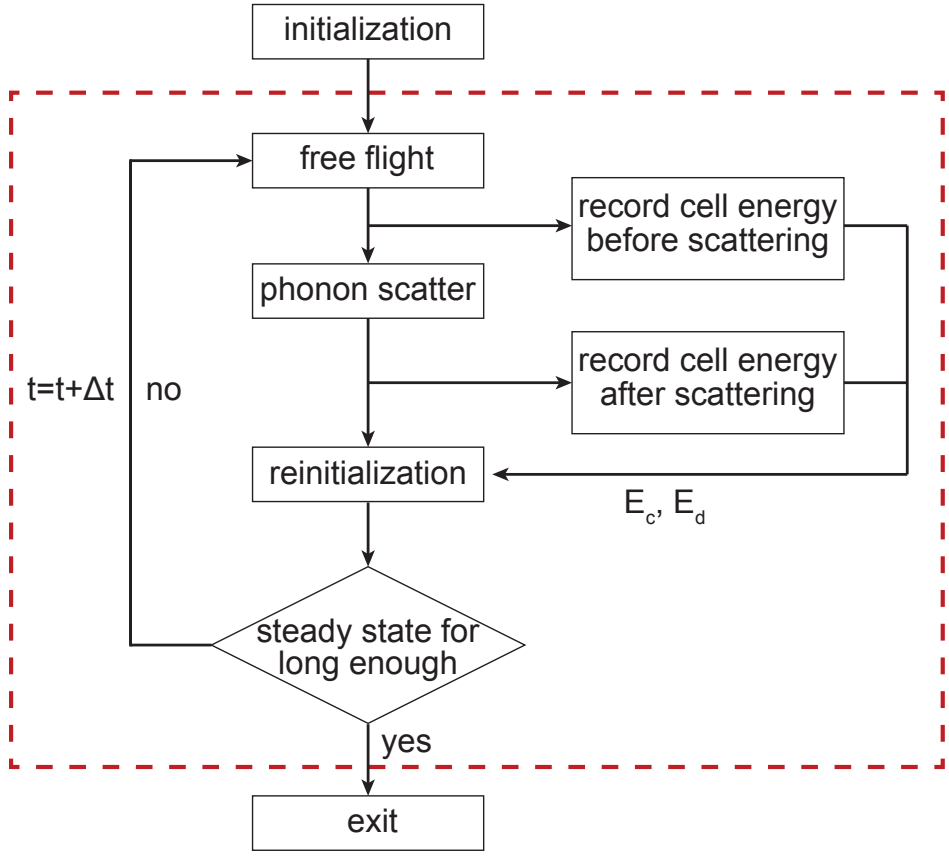

Figure 2.1: Flowchart of a PMC simulation. The dashed box encloses the transport kernel.

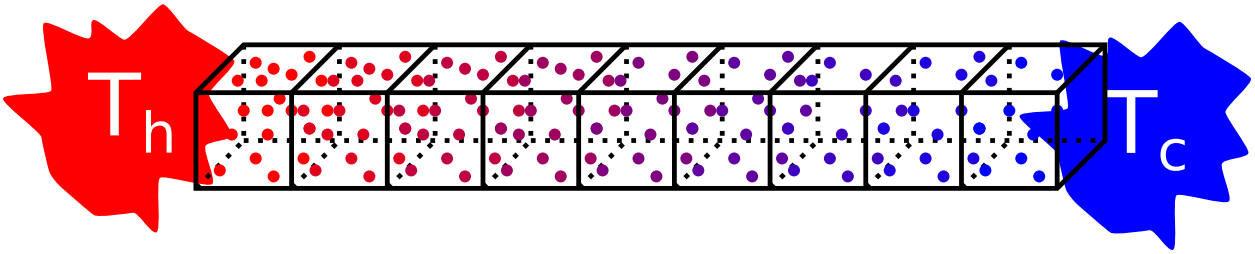

Figure 2.2: Simulation domain for a wire. The wire is divided into cells (shown as cubes, although they can be other shapes), and the first and last cells are connected to heat reservoirs held at temperatures T_h and T_c. The dots represent phonons in the simulation domain. The dot color represents the steady-state temperature profile.

From here on, we will consider only the case of a nanowire, but the method is similar in other geometries. The wire is divided into N_c cells along the direction of transport, and the first and last cells are connected to heat reservoirs held at slightly different temperatures (T_h and T_c for the hot and cold reservoirs, respectively). We will refer to the connections to the heat reservoirs as contacts, and we will describe their implementation in Sec. 2.8. T_h and T_c must be chosen with care. If the temperature difference is too large, the system will not have a meaningful local temperature. If the temperature difference is too small, the signal-to-noise ratio in Q will be large, and the simulation will be inaccurate. I found that choosing $T_h = 1.05T$ and $T_c = 0.95T$ worked well, where T is the desired average system temperature.

We define a local temperature T_i in each cell, where i is the cell index. $\mathcal{E}_i$ is the energy in cell i, and $\mathcal{N}_i$ is the number of phonons in cell i. In a cell at a temperature T_i we expect that

$$\mathcal{N}_i = V_i \sum_j \int \frac{d^3\mathbf{k}}{(2\pi)^3} n_{\text{BE}}\left(\omega_{j,\mathbf{k}}, T_i\right), \tag{2.12}$$

$$\mathcal{E}_i = V_i \sum_j \int \frac{d^3\mathbf{k}}{(2\pi)^3} \hbar\omega_{j,\mathbf{k}} n_{\text{BE}}\left(\omega_{j,\mathbf{k}}, T_i\right), \tag{2.13}$$

where the sum is over all phonon branches j, the integral is over all phonon wave vectors $\mathbf{k}$, and n_{BE} is the equilibrium phonon distribution [Eq. (1.27)]. At each time step, we find the total energy in each cell $\mathcal{E}_i$ by summing up the energies of all the phonons therein and numerically solve Eq. (2.13) for T_i. Specifically, we compute the integral with QUADPACK [78] and solve for T_i using Newton's method. T_i will play an important role in scattering, so it is important to solve for it accurately.

In steady state, we expect that T_i will vary linearly between T_h and T_c (as long as the domain is much longer than the phonon mean free path), so during initialization we set $T_i = T_h - {}^{i}/_{N_c}\left(T_h - T_c\right)$ and fill each cell with phonons from the equilibrium distribution function at T_i using the methods described in Sec. 2.8. That is all that happens during initialization.

During the free flight portion of the time step (with duration Δt), each phonon is simply displaced by $\mathbf{v}_{j,\mathbf{k}}\Delta t$ unless the phonon encounters a surface. Δt is chosen so that the phonons travel distances that are small compared to the system length scales. For example, most of the Silicon

nanowires that we consider in Sec. 4.1 are 70 nm in diameter, and the time step is 0.1 ps. The fastest phonons in the system travel a little less than 1 nm in that time.

If a phonon does encounter the surface during free flight, the simulation can handle the scattering in different ways, described in Sec. 2.5. Generally, the phonon hits a surface, is scattered into a new $\mathbf{k}$, and continues free flight in its new direction for the remainder of the time step.

Once the phonons are done with free flight and scattering from surfaces, they undergo "internal scattering" caused by impurities, alloys, and phonon–phonon interactions. The PBTE puts few restrictions on what happens in the scattering term $\left.\frac{\partial n_j(\mathbf{k},\mathbf{x},t)}{\partial t}\right|_{\text{scatt}}$, and PMC is likewise flexible and can accommodate many scattering mechanisms [74]. Phonon-phonon scattering is generally handled through a method inspired by the RTA. The phonons scatter at the same rates used in the RTA, and if a phonon scatters, it is removed from the simulation and replaced with a new phonon drawn from the equilibrium distribution. This process must be performed carefully because it does not guarantee energy conservation for individual scattering events. For this reason, it is important to record the energy before and after internal scattering, as shown in the flowchart (Fig. 2.2). The process of internal scattering and ensuring energy conservation is described in Sec. 2.6 and Sec. 2.7.

Finally, phonons that enter the contacts are removed and new phonons are injected from the contacts (Sec. 2.8).

The simulation is run until it reaches a steady state – when the power flux into and out of the system converges to the same value.[5] The simulation is then run a set number of additional time steps, and we calculate the net power through the system P at each time step. The values of P are then averaged and the thermal conductivity can be extracted from Fourier's Law (Sec. 1.4)

$$P = \kappa \frac{A\Delta T}{L}, \tag{2.14}$$

where $\Delta T = T_h - T_c$, A is the average cross-sectional area of the wire, and L is the length of the wire.

[5] I calculate the power flux at the contacts by summing up the energy that enters (exits) the wire each time step.

2.3 Generating Random Variates

This section is a quick overview of the methods used to generate random variates with a given probability distribution function (PDF). We assume that the computer used can generate random variates that are uniformly distributed over the interval $[0, 1]$.

There are two techniques for generating nonuniform random variates from uniform random variates: the inversion and rejection methods, which we explain below. (For more details on random-variate generation, see a book such as [79]).

Generally speaking, the inversion method requires more mathematical manipulation of the PDF than the rejection method. When the manipulations can be done analytically, the inversion method is usually the simpler of the two methods. While the inversion method can be performed numerically, the rejection technique is generally simpler to implement in cases when analytical inversion is not possible.

2.3.1 Inversion Method

Consider a PDF $p(x)$. The first step in the inversion method is to integrate the PDF into the cumulative distribution function (CDF)

$$F(x) = \int_{-\infty}^{x} dx' f(x') . \tag{2.15}$$

$F(x)$ is the probability that a random variate will have a value less than or equal to x.

Next, we solve $r = F(x)$ for x, i.e., we invert the CDF to get the quantile function $q(r) = F^{-1}(r)$. Then we generate a random variate r, which is uniformly distributed in $[0, 1]$. Finally, we solve $x = q(r)$ for x. The resulting x is a random variate that follows our original PDF [79]. The technique can be generalized to PDFs with multiple variables, but we will only consider PDFs that effectively depend only on a single variable.

For example, say we want to generate a random variate from the distribution given by Lambert's cosine law[6] in three dimensions, $p(\theta, \phi) = c \cos\theta$ for spherical coordinates $\theta \in [0, \pi/2], \phi \in$

[6]This is also known as Knudsen's cosine law in the context of gas molecules scattering from surfaces.

$[0, 2\pi)$ and a normalizing constant c [75]. Lambert's cosine law will prove important later (Secs. 2.8 and 2.5). First, we must properly normalize $p(\theta, \phi)$:

$$1 = \int_0^{\pi/2} \int_0^{2\pi} p(\theta', \phi') \sin\theta' d\theta' d\phi', \tag{2.16}$$

which yields $c = \pi^{-1}$. The CDF for θ is then

$$\begin{aligned} F(\theta) &= \int_0^{\theta} \int_0^{2\pi} p(\theta', \phi') \sin\theta' d\theta' d\phi' \\ &= \sin^2\theta. \end{aligned} \tag{2.17}$$

Note that our CDF only depends on θ because $p(\theta, \phi)$ does not depend on ϕ, but we keep the ϕ dependence to make clear that we still need to integrate over ϕ. Finally, we invert the CDF for a random variate r_θ that is uniformly distributed in $[0, 1]$:

$$\begin{aligned} F(\theta) &= r_\theta \,. \\ \theta &= \arcsin\left(\sqrt{r_\theta}\right). \end{aligned} \tag{2.18}$$

Using the same method, we can find the unsurprising result that $\phi = 2\pi r_\phi$, where r_ϕ is uniformly distributed in $[0, 1]$.

In this example, both the integration and inversion can be done analytically, which is the exception rather than the rule. It is possible to do both the integration and inversion numerically, but this reduces the accuracy and computational efficiency of the method. We will also encounter a case where the integration can be done analytically, but the inversion can only be done numerically (Sec. 2.5).

2.3.2 Rejection Method

In contrast with the inversion method, the rejection method does not require any integration or inversion steps. The rejection method requires three things:

- We calculate the PDF $p(x)$ for any x.

- There exists a bounding function $g(x)$ such that $\forall x, g(x) \geq p(x)$.
- We can generate random variates from a PDF that is proportional to $g(x)$.

The rejection technique does not require that $p(x)$ and $g(x)$ are normalized; they must simply be proportional to probability distribution functions. The largest drawback of the rejection method is that, unlike the inversion method, the rejection method generally requires the computer to generate several random variates that are uniformly distributed in $[0, 1]$. Choosing a $g(x)$ that closely resembles $p(x)$ will reduce the number of random variates that the computer will have to generate.

The rejection method to generate a random variate from $p(x)$ follows.

1. Generate a random variate x' from the PDF that is proportional to $g(x)$.
2. Generate a random variate y that is uniformly distributed in $[0, g(x')]$
3. If $y < p(x')$, then x' is the random variate generated from $p(x)$. Otherwise, return to step 1.

The third step ensures that the probability of choosing x' is proportional to $p(x')$, which is all that we require of a method to generate random variates from a distribution.

This procedure is easy to visualize if $p(x)$ is nonzero only on a finite interval $[a, b]$, and $p(x) \leq c$, where a, b, c are constants (Fig. 2.3). In this case, we can choose $g(x) = c$. Then the rejection method is equivalent to throwing a dart randomly and uniformly at the box defined by $x' \in [a, b], y \in [0, c]$. If $y \leq p(x')$, i.e., the dart falls below the curve $p(x)$, then we take x' as our random variate and repeat the procedure otherwise. The larger the area between $g(x)$ and $p(x)$, the more dart throws will be required on average for a dart to land below the curve $p(x)$, which reduces the efficiency of the rejection method. For this reason, even if $p(x) \leq c$, it may be wise to use a $g(x)$ other than $g(x) = c$. We do this in Sec. 2.5 when we consider Soffer's model for momentum-dependent boundary scattering [2].

We note that the rejection technique can work even if $p(x)$ diverges, which is common in physics problems (e.g., Van Hove singularities). Take the example of a probability distribution that might arise from the Bose-Einstein distribution in two dimensions (2D) and in polar coordinates:

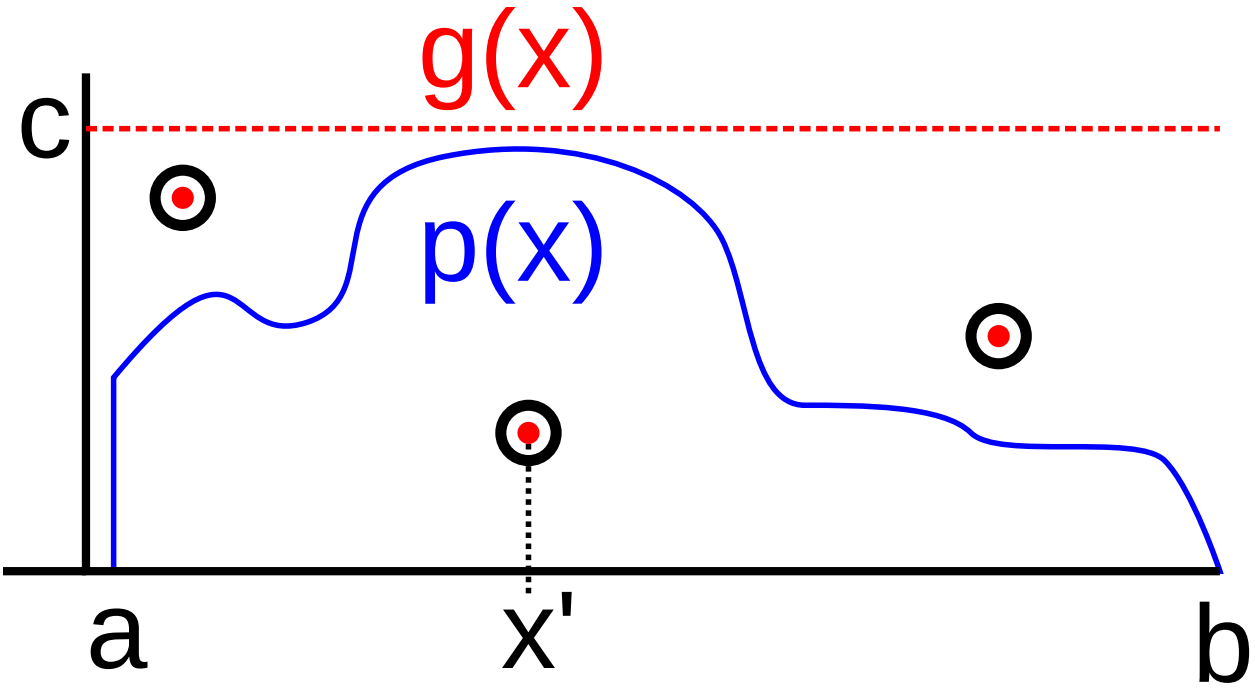

Figure 2.3: Illustration of the rejection method for a distribution $p(x)$ using a constant $g(x)$. For a constant $g(x)$, the rejection technique is the same as randomly throwing darts uniformly in the range $x \in [a, b], y \in [0, c]$. If the dart lands above the curve $p(x)$, then another dart is thrown. When a dart lands below the curve $p(x)$, then its x value, x', is accepted as the random variate. The figure depicts possible dart throws (marked with bullseyes). The throws above $p(x)$ are rejected, and x' is taken from the throw that lands below $p(x)$.

$$p(r,\theta) = \frac{1}{e^r - 1}. \tag{2.19}$$

Note that $p(r,\theta)$ is not normalized[7] and diverges at $r = 0$. Also note that $p(r,\theta) \leq r^{-1}$, so we choose $g(r,\theta) = r^{-1}$. Finally, suppose that we are considering the 2D domain $\theta \in [0, 2\pi), r \in [0, R]$, where R is a constant. On that domain, $g(r,\theta)$ and $p(r,\theta)$ are normalizable because the singularity at $r = 0$ is integrable: $\int_0^{2\pi}\int_0^R g(r,\theta)\, r dr d\theta = 2\pi R$, which is finite. Because the integrand $g(r,\theta)\, r$ is constant, the random variate r' is equally likely to take any value in $[0, R]$. So, it is quite simple to generate the random variates r' and θ': r' is uniformly distributed in $[0, R]$, and θ' is uniformly distributed in $[0, 2\pi)$.

Putting everything together, the rejection technique in this example works as follows:

1. Generate random variates r' and θ' that are uniformly distributed in $[0, R]$ and $[0, 2\pi)$, respectively.

2. Generate a random variate y that is uniformly distributed in $\left[0, (r')^{-1}\right]$

3. If $y < p(r', \theta') = \left(e^{r'} - 1\right)^{-1}$, then use r' and θ' as your random variates. Otherwise, return to step 1.

2.4 Generating Phonons

It is common to generate thermal phonons with isotropic dispersion relations using the inversion technique with numerical integration and inversion [71, 4, 26], although the rejection method is also occasionally used [70]. I believe that the rejection method is better suited to the task than the inversion method because the numerical integration and inversion can lead to a loss off accuracy or decreased computational performance [71]. So, I use the rejection method in my work [23]. Additionally, the rejection method does not require the density of states, which can be difficult to calculate, and the rejection technique is easy to apply to anisotropic dispersion relations. We will consider two branches, a TA branch and an LA branch, but the method can easily be generalized to

[7] $p(r,\theta)$ could be normalized, but that is not required for the rejection technique.

more branches. We will also assume $k_{\max} \geq |\mathbf{k}|$ is an upper bound on the wave-vector magnitude. The rejection method works as follows.

At temperature T, the number of phonons from branch j in each infinitesimal unit of reciprocal space is

$$n_{\mathrm{j}}\left(\mathbf{k}, T\right) = \frac{d^3\mathbf{k}}{\left(2\pi\right)^3} n_{\mathrm{BE}}(\omega_{j,\mathbf{k}}, T). \tag{2.20}$$

For an isotropic dispersion relation, n_j can be reduced to a function of $k = |\mathbf{k}|$ alone by integrating over the polar and azimuthal angles θ and ϕ

$$\begin{aligned} n_{\mathrm{iso},j}\left(k, T\right) &= \int_0^{2\pi} \int_0^{\pi} \frac{k^2 \sin\theta dk d\theta d\phi}{\left(2\pi\right)^3} n_{\mathrm{BE}}(\omega_{j,k}, T) \\ &= \frac{k^2}{2\pi} n_{\mathrm{BE}}(\omega_{j,k}, T) dk. \end{aligned} \tag{2.21}$$

Although n_{BE} diverges at $k = 0$, $\lim_{k\to 0} n_j\left(k\right) = 0$ because of the k^2 term. Thus, the maximum value of $n_{\mathrm{iso},j}\left(k, T\right)$ is finite, and we can use the bounding function $g\left(k\right) = C$ as described in Sec. 2.3.2, where C is any number greater than the maximum value of $n_{\mathrm{iso,TA}}\left(k, T\right) + n_{\mathrm{iso,LA}}\left(k, T\right)$. The maximum value of $n_j\left(k, T\right)$ is temperature dependent, but instead of finding a new C whenever the temperature changes, simply find a C that works for a temperature higher than any conceivable temperature in the simulation. Once C is found, the rejection method follows the familiar pattern:

1. Generate a random variate k' that is uniformly distributed in $[0, k_{\max}]$
2. Generate a random variate y that is uniformly distributed in $[0, C]$
3. If $y < n_{\mathrm{iso,TA}}\left(k', T\right)$, then generate a TA phonon with wavenumber k'. If $n_{\mathrm{iso,TA}}\left(k', T\right) < y < n_{\mathrm{iso,TA}}\left(k', T\right) + n_{\mathrm{iso,LA}}\left(k', T\right)$, then generate an LA phonon with wavenumber k'. Otherwise, return to step 1.

Once we know the wavenumber k of the new phonon, we need to choose a direction. In equilibrium, all directions are equally likely [$p\left(\theta, \phi\right) = d$, where d is a constant], and we can use the inversion technique to choose a direction. First, we normalize the distribution to find d

$$
\begin{aligned}
1 &= \int_0^{\pi} \int_0^{2\pi} p\left(\theta', \phi'\right) \sin\theta' d\theta' d\phi' \\
d &= \left(4\pi\right)^{-1}.
\end{aligned}
\tag{2.22}
$$

The CDF is

$$
\begin{aligned}
P\left(\theta\right) &= \int_0^{\theta} \int_0^{2\pi} p\left(\theta', \phi'\right) \sin\theta' d\theta' d\phi' \\
&= \frac{1 - \cos\theta}{2}.
\end{aligned}
\tag{2.23}
$$

Inverting for a random variate r_θ that is uniformly distributed in $[0, 1]$

$$
\theta = \arccos\left(1 - 2r_\theta\right). \tag{2.24}
$$

ϕ is uniformly distributed in $[0, 2\pi]$. All together, the wavevector of the new phonon is

$$
\mathbf{k} = k' \begin{pmatrix} \sin\left(\theta\right)\cos\left(\phi\right) \\ \sin\left(\theta\right)\sin\left(\phi\right) \\ \cos\left(\theta\right) \end{pmatrix}. \tag{2.25}
$$

The above approach to generating phonons is very general and does not depend on a specific distribution function for $\mathbf{k}$ or a specific angular distribution function. So, there is nothing preventing us from replacing Eq. (2.21) or Eq. (2.24) with other functions. Indeed, for internal scattering (Sec. 2.6) we will change the distribution function for $\mathbf{k}$ while keeping the angular distribution function the same, and for boundary contacts (Sec. 2.8.2), we will change both the distribution function for $\mathbf{k}$ and the angular distribution function. The code behind the simulation should likewise be flexible so that it can be easily reused to generate phonons from different distributions.

2.5 Surface Scattering

A good example of the flexibility in the PMC method is the ability to use a range of surface scattering mechanisms for real-space surfaces. I will mostly make use of a straightforward method:

phonons scatter specularly from the real space surfaces (generated as described in Sec. 1.5) and do not change branch of frequency. The PMC method can also implement nonspecular scattering where phonons change branches [80].

However, as we noted in Chapter 1, a common class of phonon–surface scattering models are based on the idea of a "specularity parameter," which gives the probability that a phonon will scatter specularly from a surface. Phonons that do not scatter specularly are instead scattered diffusely in accordance with Lambert's cosine law (Sec. 2.3.1). This is the basis of Casimir's model [17] (and its extensions [18, 19, 2]) that were mentioned in Chapter 1. Specularity parameter models are almost always used together with a smooth surface,[8] and the basic idea is to make a smooth surface act like a rough one by randomizing the outgoing phonon direction.

Since we will compare our results to those from specularity-parameter models, we detail how to implement specularity parameter models in PMC. We consider both models where the specularity parameter is constant [18] or dependent on the phonon momentum and surface roughness [19, 2]. Our work is the first example of momentum-dependent specularity parameter models used in PMC, and their implementation requires a good understanding of the random variate generation techniques described in Sec. 2.3. Later, we will see that specularity-parameter models fail when the surfaces are very rough (Sec. 4.1).

2.5.1 Diffuse Surface Scattering and Specularity Parameters

All phonon–surface scattering models must respect detailed balance in equilibrium: the number of phonons scattered into any solid angle must be equal to the number of phonons incident on the surface from the same solid angle. Consider a flat surface with a surface normal vector $\hat{\mathbf{n}}$. In this section, θ will refer to the angle between a phonon's wave vector $\mathbf{k}$ and $\hat{\mathbf{n}}$. (We will assume that the dispersion relation is isotropic so that $\mathbf{k}$ is in the same direction as the velocity.) Phonons with larger $\cos\theta$ will strike the surface more frequently (Fig. 2.4), and in equilibrium this leads to Lambert's cosine law: the number of phonons incident on a surface at an angle θ must also be

[8] Although specularity parameter models can be used with rough surfaces.

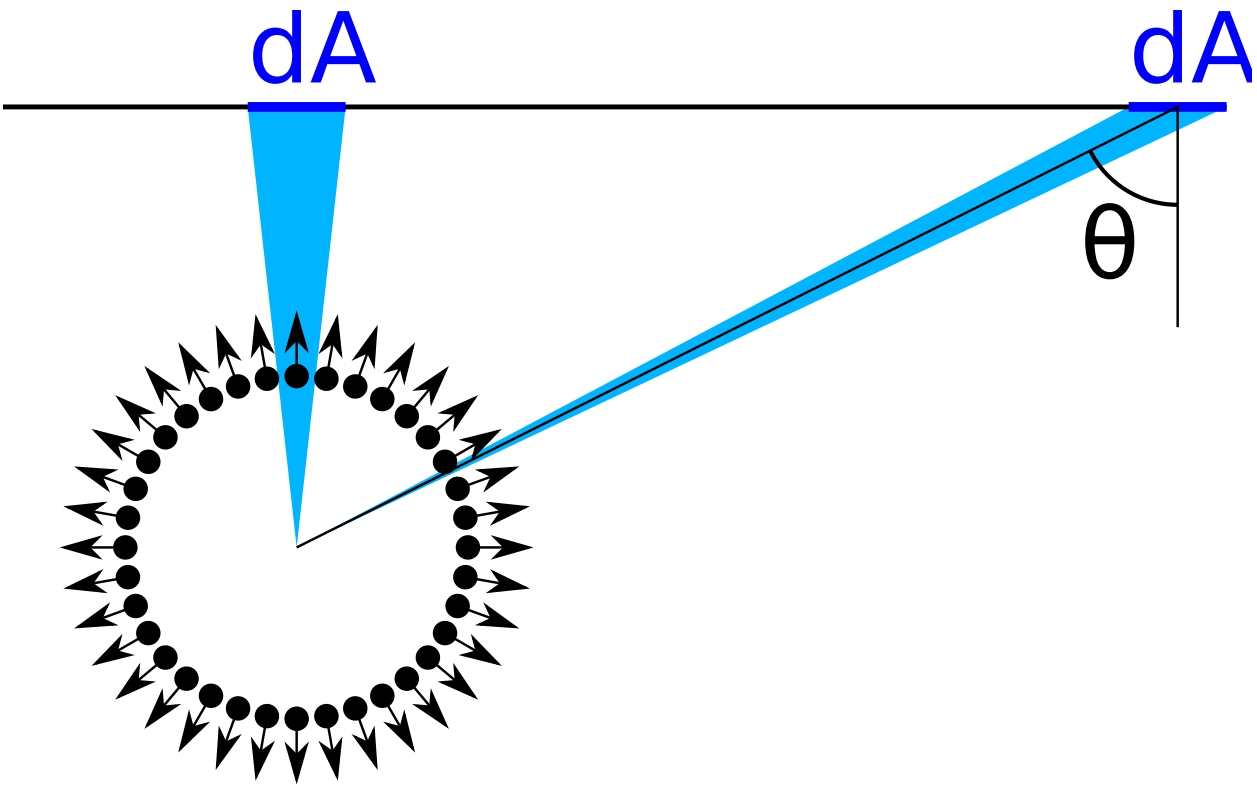

Figure 2.4: Illustration of Lambert's cosine law. An equilibrium ensemble of phonons is depicted as a group of particles with uniform angular distribution (lower left). The number of phonons striking a small patch of surface dA at an angle θ (measured from the surface normal) is proportional to the angle subtended by the shaded wedges. This angle is proportional to $\cos\theta$ (if dA is small), which is the basis for Lambert's cosine law.

proportional to $\cos\theta$. Because of detailed balance, the number of phonons being scattered into an angle θ also must be proportional to $\cos\theta$.

For specular scattering, detailed balance in equilibrium holds automatically. For totally diffuse scattering (known as the "Casimir limit"), the inversion method can be used to generate random wave vectors that satisfy Lambert's cosine law (Sec. 2.3.1) with the result given in Eq. (2.18). For the constant-specularity-parameter model, one simply chooses a probability p of specular scattering before running the simulation. Then, each time a phonon strikes the surface, the phonon is specularly scattered with probability p and is otherwise diffusely scattered into a randomly chosen direction chosen in accordance with Lambert's cosine law.

The situation is somewhat more complicated for momentum-dependent specularity-parameter models. Take Soffer's model [2], which accounts for uncorrelated roughness (i.e., correlation length $\xi = 0$) when the RMS roughness Δ is small [44]. The probability that a phonon scatters specularly is

$$p(\theta, \phi) \propto e^{-(2\Delta|\mathbf{k}|\cos\theta)^2}. \tag{2.26}$$

Because the probability of diffuse scattering now depends on the angle of incidence, the outgoing phonon distribution no longer follows a simple cosine law (Fig. 2.5). We will first attempt to use the inversion technique to find the correct distribution of scattered phonons; after encountering difficulties, we will turn to the rejection technique.

The angular distribution of phonons incident on the surface is still proportional to $\cos\theta$, and the probability of diffuse scattering is $1 - p(\theta, \phi)$, so the distribution of incoming phonons that will be diffusely scattered is

$$\begin{aligned} f(\theta, \phi) &= C\cos\theta\,(1 - p(\theta, \phi)) \\ &= C\cos\theta\left(1 - e^{-(2\Delta k\cos\theta)^2}\right), \end{aligned} \tag{2.27}$$

where $k = |\mathbf{k}|$, and C is a normalization constant given by

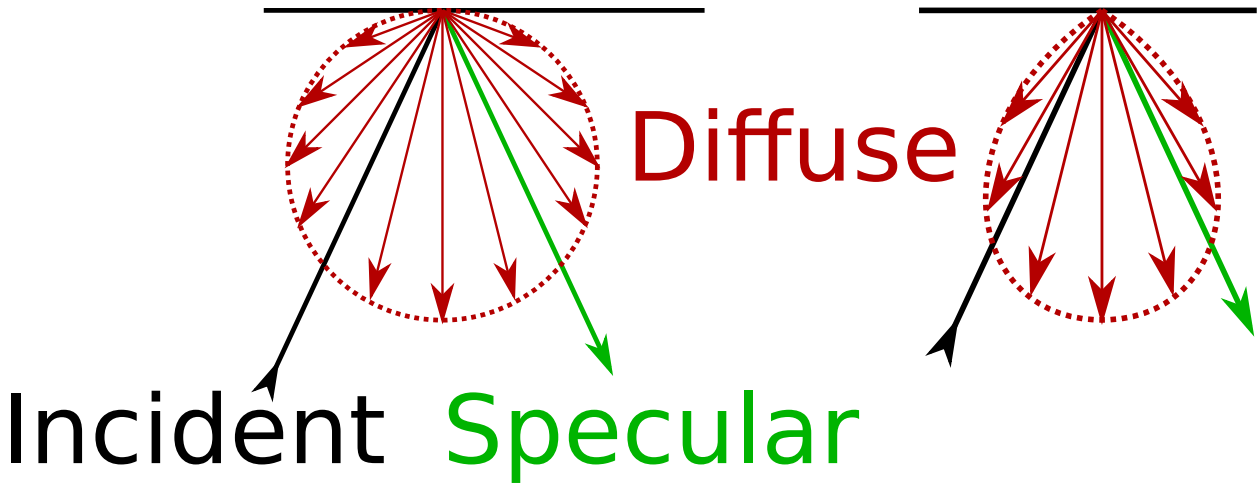

Figure 2.5: Polar plots of the angular distribution of the outgoing phonon momentum upon diffuse scattering from a surface with (left) a constant specularity parameter and (right) Soffer's momentum-dependent specularity parameter, Eq. (2.26) [2]. Soffer's momentum-dependent specularity parameter reduces the chance of diffuse scattering as θ (the angle between the phonon wave vector and the surface normal) increases. To satisfy detailed balance, the distribution of outgoing phonons must match the probability of diffuse scattering. The result is a teardrop-shaped distribution, which suppresses scattering at large θ.

$$\begin{aligned} 1 &= \int_0^{\pi/2} \int_0^{2\pi} f\left(\theta', \phi'\right) \sin\theta' d\theta' d\phi', \\ C^{-1} &= 2\pi \left(1 - \frac{1 - e^{-4\Delta^2 k^2}}{4\Delta^2 k^2}\right). \end{aligned} \tag{2.28}$$

Now that C is known, we can find the CDF

$$\begin{aligned} F\left(\theta\right) &= \int_0^{\theta} \int_0^{2\pi} f\left(\theta', \phi'\right) \sin\theta' d\theta' d\phi' \\ &= \frac{\frac{e^{-4\Delta^2 k^2} - e^{-4\Delta^2 k^2 \cos^2(\theta)}}{4\Delta^2 k^2} + \sin^2\left(\theta\right)}{1 - \frac{1 - e^{-4\Delta^2 k^2}}{4\Delta^2 k^2}}. \end{aligned} \tag{2.29}$$

We have been able to do the integration step analytically, but we cannot do the inversion step analytically. So,

$$r_\theta = \frac{\frac{e^{-4\Delta^2 k^2} - e^{-4\Delta^2 k^2 \cos^2(\theta)}}{4\Delta^2 k^2} + \sin^2\left(\theta\right)}{1 - \frac{1 - e^{-4\Delta^2 k^2}}{4\Delta^2 k^2}} \tag{2.30}$$

would have to be solved numerically, for example with Newton's method (which requires computing $\frac{dF}{d\theta}$), the bisection method, or a 2D lookup table as an approximation [2D since Eq. (2.30) is a function of both k and θ].

The other option is to use the rejection technique. This is particularly appealing because we already have a good distribution function $g\left(\theta, \phi\right) \geq f\left(\theta, \phi\right)$, namely $g\left(\theta, \phi\right) = \cos\theta$, which is the distribution we use for the constant-specularity parameter model.[9] The rejection method to find the outgoing angle θ' of a scattered phonon is then:

1. Generate a random variate $\theta' = \arcsin\left(\sqrt{r_\theta}\right)$ where r_θ is uniformly distributed in $[0, 1]$.
2. Generate a random variate y that is uniformly distributed in $[0, \cos\theta']$
3. If $y < f\left(\theta', \phi\right) = \cos\theta' \left(1 - e^{-(2\Delta k \cos\theta')^2}\right)$, then use θ' as your random variate. Otherwise, return to step 1.

[9] We could also use a constant distribution function for $g\left(\theta, \phi\right)$ as described in Sec. 2.3.2, but that would result in reduced performance.

Because we have a good $g(\theta, \phi)$, and because the inversion method will require an iterative solution or a less accurate lookup table, the rejection method is both faster and simpler to implement, and likely more accurate.

2.5.2 Casimir's Model as a Test

Casimir's model provides a useful test of our PMC simulation because Casimir's model can be reduced to a relaxation rate that can be used in the RTA. Casimir derived his model in a clever way by considering blackbody radiation emitted by the interior surface of a long tube with a small temperature gradient along its axis. By calculating the blackbody radiation energy flux through the wire [75], Casimir was able to extract an equation that looks identical to the RTA expression for thermal conductivity [Eq. (2.11)] with a relaxation time of

$$\tau_{j,k} = \frac{d}{v_{j,k}} \tag{2.31}$$

for a round wire of diameter d and

$$\tau_{j,k} = \frac{2}{\sqrt{\pi}} \frac{W}{v_{j,k}} \approx 1.13 \frac{W}{v_{j,k}} \tag{2.32}$$

for a square wire of width W.

These relaxation rates have a simple interpretation. We will later see that, in the absence of internal scattering, particles in a square wire will travel an average distance W before hitting the surface (Sec. 4.1). So Casimir's effective relaxation rates can be interpreted to mean that the phonons will, on average, travel a distance W between being surface scattering events.[10]

So, a logical test is to run the PMC simulation with diffuse boundary scattering (and without internal scattering) and compare the results to those found with the RTA (Eq. 2.11). The outcome of this test is shown in Fig. 2.6. The simulation reproduces Casimir's result.

[10] The factor of $2/\sqrt{\pi} \approx 1.13$ does not have an easy interpretation. It can probably be thought of as a small correction to the simple interpretation in the text.

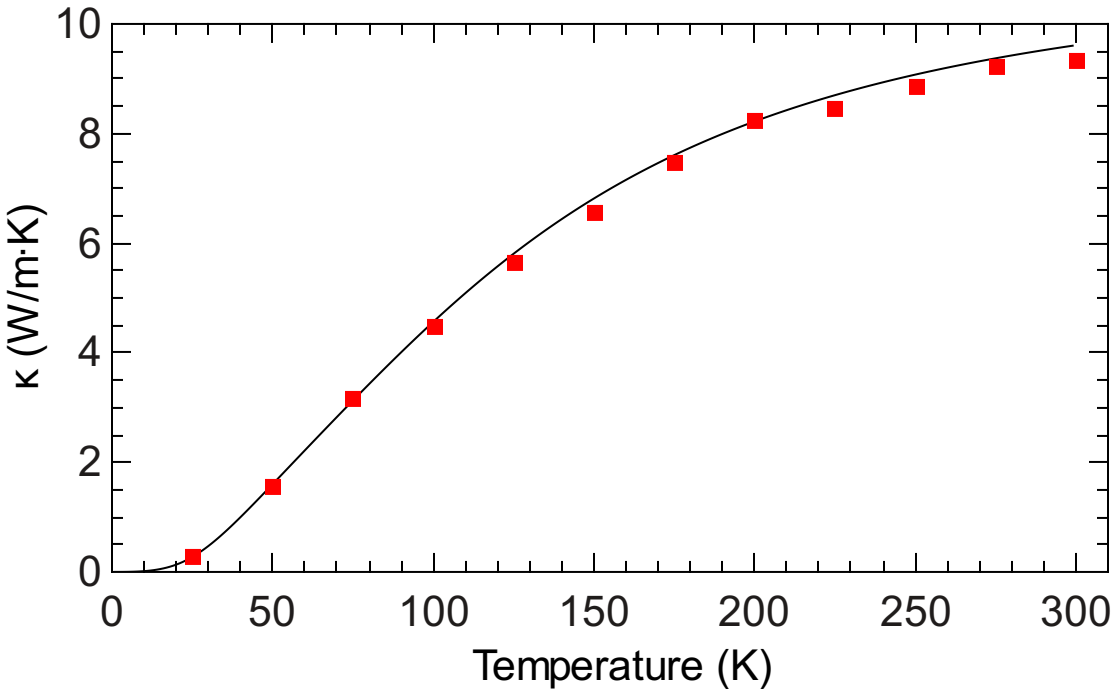

Figure 2.6: Thermal conductivity in the Casimir limit of totally diffuse surface scattering for a silicon nanowire of 10x10 nm^2 cross-section without internal scattering. The curve is from Eq. (2.11), numerically integrated with the effective Casimir relaxation time [Eq. (2.32)]. The points are the results of the PMC simulation with materials parameters described in Sec. 4.1. The results are in good agreement.

2.6 Internal Scattering

We define "internal scattering" to mean any scattering that would happen in a bulk material (i.e., everything except surface scattering). Because of the flexibility of the PMC method, we can tailor the implementation of the scattering mechanisms to match their underlying physics.

The first step is to calculate the scattering rates for each phonon. We considered impurity scattering and phonon–phonon scattering.

We use an impurity scattering rate of

$$\Gamma_I(\omega) = (A_{iso} + A_{\delta R} + A_{\delta M})\,\omega^4, \tag{2.33}$$

where $A_{iso} = 1.32 \times 10^{-45}\text{s}^3$ is the isotope scattering constant [3, 81]. $A_{\delta R}$ and $A_{\delta M}$ can account for the relative displacement and mass difference due to dopants, respectively, but both were set to zero for simulating SiNWs, which can be grown with very low dopant densities [9].

We tried phonon–phonon scattering rates from Holland [3] with Lacroix's modifications [4], Ward and Broido [5], and Morelli *et al.* [6]. We found that Holland's rates did not reproduce the bulk thermal conductivities well (Fig. 2.7). The other two did better, with the rates from Morelli *et al.* doing an excellent job below 350 K. (Ward and Broido's rates were developed for temperatures above 300 K [5].) So, we used the rates from Morelli *et al*.

The rates are [6]

$$\Gamma_{T,N}(\omega, T) = B_{TN}\omega T^4, \tag{2.34}$$

$$\Gamma_{T,U}(\omega, T) = B_{TU}\omega^2 T e^{-\frac{\Theta_T}{3T}}, \tag{2.35}$$

$$\Gamma_{L,N}(\omega, T) = B_{LN}\omega^2 T^3, \tag{2.36}$$

$$\Gamma_{L,U}(\omega, T) = B_{LU}\omega^2 T e^{-\frac{\Theta_L}{3T}}, \tag{2.37}$$

where the subscripts N, U, T, and L denote normal, umklapp, transverse, and longitudinal, respectively. $\Theta_T = 240$ K and $\Theta_L = 586$ K are the Debye temperatures for the two modes [6]. $B_{TN} = 3.29 \times 10^{-13}\,\text{K}^{-4}$, $B_{TU} = 4.63 \times 10^{-20}\,\text{sK}^{-1}$, $B_{LN} = 1.11 \times 10^{-24}\,\text{sK}^{-3}$, and

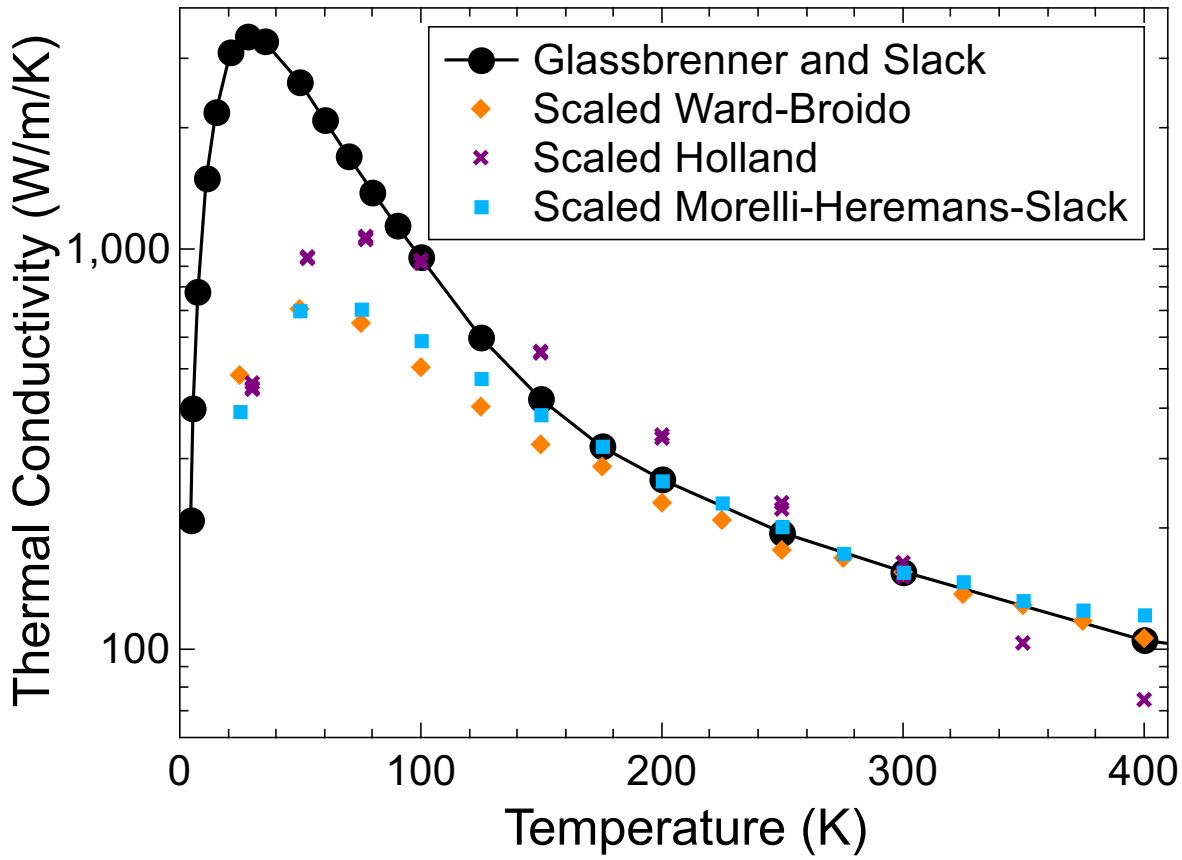

Figure 2.7: Thermal conductivity results from PMC simulations of bulk silicon (i.e., a smooth wire with 100% specular scattering) using rates from Holland [3] with modifications from Lacroix *et al.* [4] (purple 'x's), Ward and Broido [5] (orange diamonds), and Morelli *et al.* [6] (blue squares). The black line shows measured bulk thermal conductivity [7]. The phonon–phonon scattering rates were scaled so that they match the bulk values at 300 K. The mean free path increases at low temperatures — eventually exceeding the length of the simulated wire. This causes the measured and simulated thermal conductivities to diverge at low temperatures. This is not an issue when boundary scattering is added. The rates from Morelli *et al.* provide an excellent fit below 350 K.

$B_{LU} = 2.55 \times 10^{-20}$ sK^{-1}. These are the constants from Morelli *et al.*. scaled together by 0.463 so that the simulation correctly reproduces the thermal conductivity of bulk silicon at 300 K. This scaling is necessary in part because those rates assume a different dispersion relation and use Callaway's model for normal scattering [82]. (We address normal scattering in Sec. 2.6.1.)

The total internal scattering rate for a phonon in branch j is

$$\Gamma_j(\omega, T) = \Gamma_{j,U}(\omega, T) + \Gamma_{j,T}(\omega, T) + \Gamma_I(\omega, T). \tag{2.38}$$

The probability of scattering during a time step of duration Δt is [71]

$$P_{\text{scatt},j}(\omega, T) = 1 - e^{-\Gamma_j(\omega,T)\Delta t}. \tag{2.39}$$

If the phonon scatters, we randomly select a scattering method with a probability proportional to the method's scattering rate. E.g., the probability that a scattered phonon undergoes umklapp scattering is Γ_U/Γ. Now that a scattering mechanism has been chosen, the details of the scattering process depend on that mechanism.

Impurity scattering is largely a two-phonon process: one phonon enters and one leaves. Consequently, the incoming and outgoing phonons have the same energy (and k for isotropic dispersion relations) but travel in different directions. So, for impurity scattering, we simply keep the phonon's branch and k the same but choose a new direction for $\mathbf{k}$ using Eq. (2.25) [71].

Normal and umklapp scattering are handled in a way similar to the RTA: scattered phonons are deleted and replaced with new phonons drawn from the equilibrium distribution. So, it might be tempting simply to remove the scatted phonons and replace them with new phonons generated according to the procedure described in Sec. 2.4. However, there is a subtle flaw with that logic. We can see from Eq. (2.34) that high frequency phonons have a high scattering rate. However, high frequency phonons are uncommon in equilibrium, so the procedure in Sec. 2.4 produces few high frequency phonons. In short, if we are not careful, we would remove more high frequency phonons than we would add and thus drive our system away from equilibrium.

To avoid this problem, we adopt the method of Lacroix *et al.* [4]: instead of generating phonons from an equilibrium distribution, we use the same procedure but use a modified distribution

$$n_{\text{scatt},j}(\omega,T) = n_{\text{iso},j}(\omega,T)\, P_{\text{scatt},j}(\omega,T)\, \frac{\Gamma_{j,N}(\omega,T) + \Gamma_{j,U}(\omega,T)}{\Gamma_j(\omega,T)}, \tag{2.40}$$

which is the equilibrium distribution from Sec. 2.2 multiplied by the probability of normal or umklapp scattering. This ensures that detailed balance holds: phonons that are more likely to be scattered in equilibrium are also more likely to be generated.

So, if a phonon undergoes umklapp scattering, it is deleted and a new phonon is generated in its place using the procedure in Sec. 2.2 except using $n_{\text{scatt},j}$ instead of $n_{\text{iso},j}$.

2.6.1 Normal Scattering

Normal scattering plays a complicated role in thermal transport because, in the case of linear dispersion relations, normal scattering alone cannot cause a finite thermal conductivity [33, 83] (Sec. 1.3.6). However, normal scattering does have an effect on κ by enhancing other scattering mechanisms [33, 83, 82, 42], but it is not clear how to best capture that effect in PMC.

If there is only normal scattering, the equilibrium phonon distribution is not given by Eq. (1.27) but instead is [83]

$$n_j(\mathbf{k},T,\boldsymbol{\lambda}) = \frac{1}{e^{\left(\hbar\omega_{j,\mathbf{k}} + \boldsymbol{\lambda}\cdot\mathbf{k}\right)/k_BT} - 1}, \tag{2.41}$$

where $\boldsymbol{\lambda}$ represents a convective "flow" of the phonons; since normal scattering conserves crystal momentum, the phonons can have a net current even in equilibrium. $\boldsymbol{\lambda}$ is determined by the condition [83]

$$\sum_{\mathbf{k}} \mathbf{k} n_j(\mathbf{k},T) = \sum_{\mathbf{k}} \mathbf{k} n_j(\mathbf{k},T,\boldsymbol{\lambda}). \tag{2.42}$$

In other words, $\boldsymbol{\lambda}$ must be chosen so that the net crystal momentum in the system is the same as the net crystal momentum expected from $n_j(\mathbf{k},T,\boldsymbol{\lambda})$.

Arguably, the best way to include normal scattering in PMC is to generate new phonons from $n_j(\mathbf{k},T,\boldsymbol{\lambda})$ during normal scattering, since normal scattering should cause our system to relax

towards $n_j\left(\mathbf{k}, T, \boldsymbol{\lambda}\right)$. However, that would require us to solve for both T_i and $\boldsymbol{\lambda_i}$ for every cell each time step, which is not trivial to do.

Another option is to treat normal scattering like umklapp scattering, even though we know that they are quite different. As long as $\boldsymbol{\lambda}$ is small, this could be a passable approximation. However, there are situations where $\boldsymbol{\lambda}$ is quite large [84, 85] (the "hydrodynamic regime").

Instead, we adopt the method of Lacroix *et al.* [4]: normal scattering follows the same procedure as umklapp scattering except that we make the newly generated phonon travel in the same direction as the phonon that scattered. While Lacroix's method will not perfectly conserve crystal momentum, it is easy to implement and is an improvement over treating normal scattering like umklapp scattering. Fig. 2.8 shows that there are significant differences between the method of Lacroix *et al.* and treating normal scattering like umklapp scattering. The method of Lacroix *et al.* is clearly the more accurate of the two.

2.7 Energy Conservation

The internal scattering procedure described in Sec. 2.6 will not exactly conserve energy because the procedure relies on replacement phonons drawn at random from a distribution, so there will be some variation in energy due to the randomness. While the energy should be conserved on average, to ensure that the simulation is stable, we add or delete phonons as needed to enforce energy conservation after internal scattering. After the phonons are done with free flight but before internal scattering, we record the energy in each cell $\mathcal{E}_{\mathrm{b},i}$.

When deleting or adding phonons it is very important that the procedure not be biased in any way; deleted phonons must be chosen at random and new phonons must be generated from the equilibrium distribution. These restrictions preclude enforcing exact energy conservation because adding or deleting phonons without bias will not lead to exact energy conservation (except in exceedingly rare circumstances).

Even a very subtle bias can have significant consequences in a PMC simulation. For example, suppose that a cell had too little energy. We then add phonons from the equilibrium distribution until adding a phonon causes the current energy in the cell $\mathcal{E}_i > \mathcal{E}_{\mathrm{b},i}$. So, we could discard the

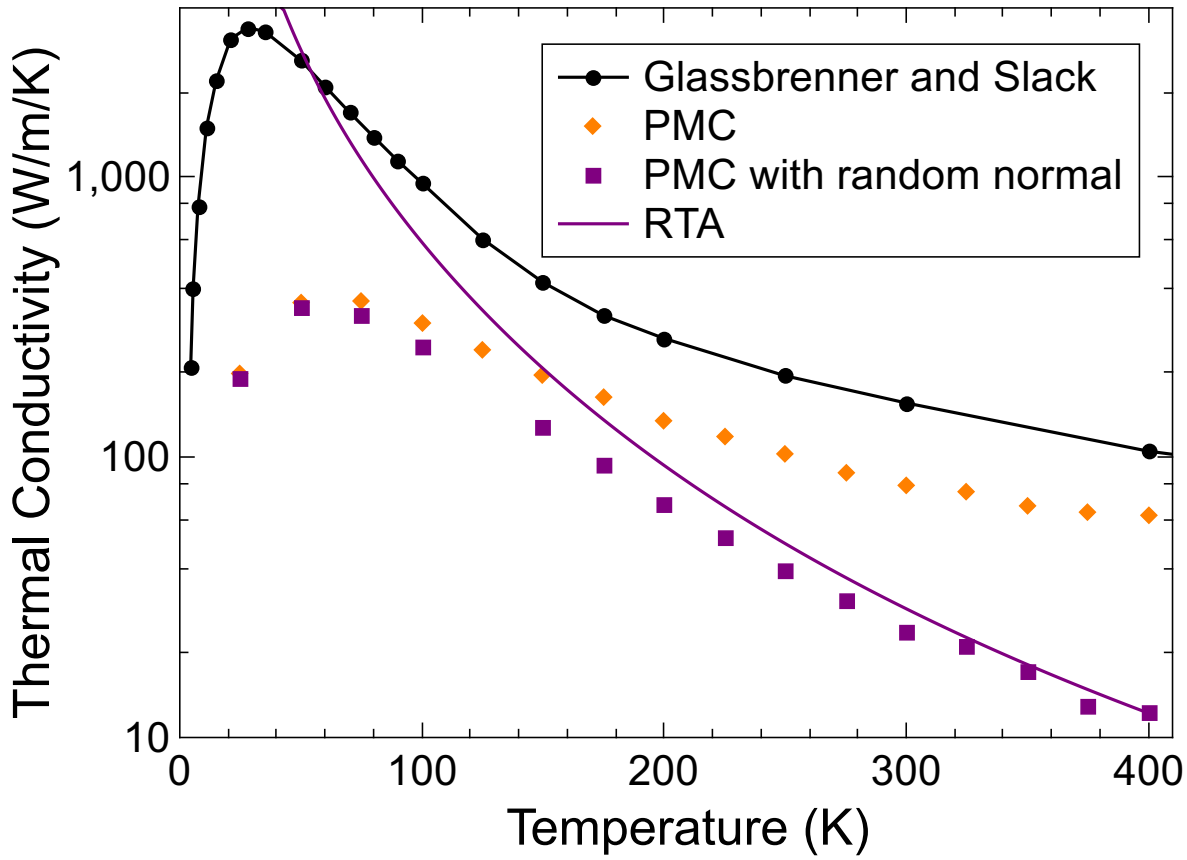

Figure 2.8: Effects of normal scattering seen in the thermal conductivity results from PMC simulation of bulk material (i.e., a wire with 100% specular scattering) using unscaled rates from Morelli *et al.* [6]. The black line shows measured bulk thermal conductivity data [7]. (Because the rates are unscaled, the simulation and experimental results will not match.) The purple squares show the results from the PMC simulation when normal scattering is treated like umklapp scattering (see Sec. 2.6.1). These results are similar to the RTA results (purple line) but are significantly different than the method of Lacroix *et al.* [4] (orange diamonds). Clearly, treating normal and umklapp scattering the same way makes it more difficult to match experimental results. [Recall that, when scaled, Lacroix's model fits the experimental results well (Fig. 2.7).]

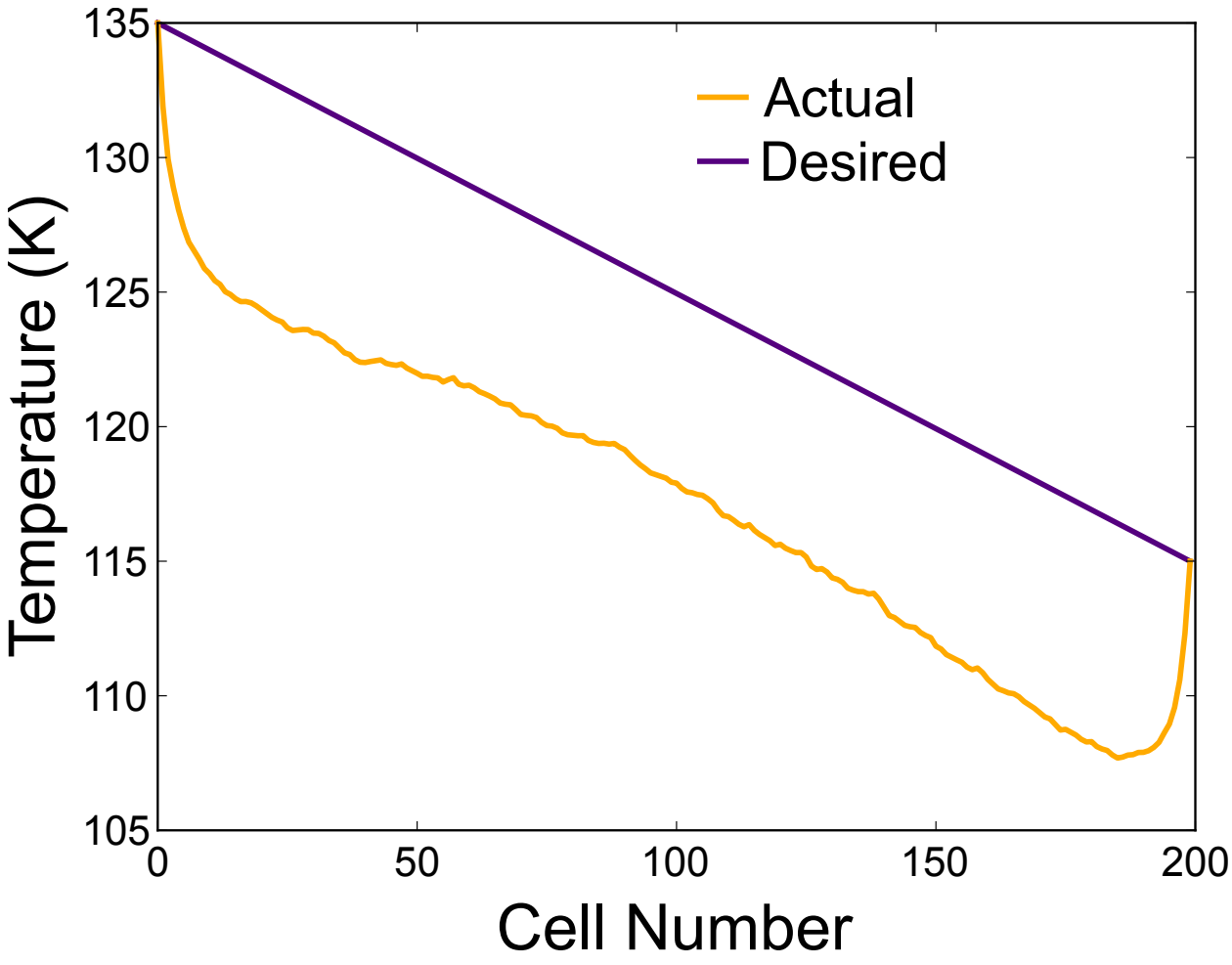

Figure 2.9: The effect of forcing exact energy conservation by adding one phonon to each cell per time step that is not drawn from the equilibrium distribution. The disparity between the expected temperature profile (purple) and actual energy profile (orange) is striking. The attempt to enforce exact energy conservation generates low frequency phonons, which have high group velocities and can carry energy out of the wire. The result is a dramatic loss of energy from the center of the wire.

last phonon to be added and instead add a phonon with energy $\mathcal{E}_{\mathrm{b},i} - \mathcal{E}_i$ so that energy is exactly conserved. This phonon must have less energy than the unbiased phonon that was discarded, so the new phonon will typically be a low energy phonon. Low energy phonons typically have high velocities and low scattering rates, so can sometimes excape the wire without scattering. It may not seem that adding a single fast phonon per cell per time step would be a problem, but the results are catastrophic at low enough temperatures (Fig. 2.9). These fast phonons leave the system quickly and cause the energy in the middle of the wire to drop significantly.

To avoid any bias, the best we can do is add or delete phonons until

$$\mathcal{E}_i \in \left[\mathcal{E}_{\mathrm{d},i} - \hbar\omega_{\max}/2, \mathcal{E}_{\mathrm{d},i} + \hbar\omega_{\max}/2\right], \tag{2.43}$$

where $\mathcal{E}_{\mathrm{d},i}$ is the amount of energy desired in the cell, and stop immediately after $\mathcal{E}_i$ enters that range. That is always possible without putting any restrictions on which phonons are added or deleted. The trick is choosing $\mathcal{E}_{\mathrm{d},i}$ such that energy is conserved on average. To do this, we record the offset $\mathcal{E}_{\mathrm{o},i}$ between the desired energy before internal scattering $\mathcal{E}_{\mathrm{d},i}$ and the energy after adding or deleting phonons $\mathcal{E}_i$. In other words, $\mathcal{E}_{\mathrm{o},i} = \mathcal{E}_i - \mathcal{E}_{\mathrm{d},i}$. In the next time step we then set $\mathcal{E}_{\mathrm{d},i} = \mathcal{E}_{\mathrm{b},i} + \mathcal{E}_{\mathrm{o},i}$ to compensate for the previous offset. In effect, we have created a running total of the offset and adjust $\mathcal{E}_{\mathrm{d},i}$ to minimize the accumulated offset.

For deletion, it is important that the phonons are truly chosen at random. When implementing the simulation, it may be simplest to delete the newest or oldest phonons first. However, the oldest phonons typically have a low scattering rate, and the newest phonons were added to replace scattered phonons, so the newest phonons typically have high scattering rates. In short, deleting phonons because they are new or old is a type of bias.

When adding phonons, it is important to generate the phonons from the equilibrium distribution (Sec. 2.4) and not the modified distribution for scattering (Sec. 2.6). The modified distribution is biased towards producing high energy phonons, which scatter more often, and is inappropriate for enforcing equilibrium. Using phonons from the modified distribution causes the opposite of the problem shown in Fig. 2.9: the temperature profile bows up instead of down (although the effect is less pronounced).

The added phonons should be placed randomly throughout the cell.

2.8 Contacts and Initialization

We need contacts at the ends of the simulation domain to act as fixed-temperature phonon reservoirs and maintain a temperature gradient across the wire. These reservoirs must inject new phonons into the simulation domain and absorb the phonons that leave it. There are two basic methods to implement contacts: either the boundaries of the simulation domain mimic reservoirs outside the simulation domain, or parts of the simulation domain get turned into reservoirs. We will call the former a *boundary contact* and the latter an *internal contact*.

Both approaches can make use of existing code, because all phonon generation follows roughly the same approach. Internal contacts can reuse the code for internal scattering and energy conservation, and boundary contacts can reuse the code for diffuse surface scattering. All PMC simulations will implement internal scattering mechanisms, so it is always straightforward to implement internal contacts. In contrast, not all PMC simulations will implement diffuse surface scattering, so it may take extra work to implement boundary contacts. We will see that boundary contacts require fewer new phonons to be generated each time step, which leads to better performance.

I use boundary contacts in my simulation (Sec. 4.1), but I include a description of internal contacts for completeness and contrast.

2.8.1 Internal Contacts and Initialization

Internal contacts are relatively simple to implement because the approach almost exclusively reuses code from other parts of the simulation. One simply deletes all the phonons in a volume near at the end of the simulation domain (usually the first and last cells) and then fills the volume with new phonons drawn from the equilibrium distribution (Sec. 2.4) and placed randomly throughout the cell. The only requirement on the volume is that it must be large enough that no phonons can traverse the volume from end to end in one time step.

There are two equivalent ways to fill the volume: either with a certain number of phonons ("fill by number"), or by adding phonons until the cell has the correct energy ("fill by energy"). It is

simpler to implement code that fills by number, but the simulation will already need code to fill volumes by energy (to enforce energy conservation), in which case filling by energy can re-use existing code. The procedure to fill by energy is the same as that described in Sec. 2.7, except that we do not need to take any offset into account. So we explain how to fill by number here. (Boundary contacts will also use number rather than energy.)

The average number of phonons in a volume V at a temperature T is[11]

$$\mathcal{N} = V \sum_j \int \frac{d\mathbf{k}}{(2\pi)^3} n_{\text{BE}}\left(\omega_{j,\mathbf{k}}, T\right), \tag{2.44}$$

where the sum is over the branches. The above expression can be simplified for an isotropic dispersion relation

$$\begin{aligned} \mathcal{N} &= V \int_0^{2\pi} \int_0^{\pi} \int_0^{k_{\text{max}}} n_{\text{BE}}\left(\omega_{j,\mathbf{k}}, T\right) \frac{k^2 \sin\theta dk d\theta d\phi}{(2\pi)^3}, \\ &= \frac{V}{2\pi^2} \int_0^{k_{\text{max}}} n_{\text{BE}}\left(\omega_{j,\mathbf{k}}, T\right) k^2 dk, \end{aligned} \tag{2.45}$$

where $k = |\mathbf{k}|$.

$\mathcal{N}$ will not be an integer in general. So, add $\lfloor \mathcal{N} \rfloor$ phonons and then randomly, with a probability of $\mathcal{N} - \lfloor \mathcal{N} \rfloor$, add one more phonon. For example, if $\mathcal{N} = 1192.63$, then always add 1192 phonons and add an additional phonon 63% of the time. In this case, it might be that the additional phonon probability can be done without, but as we saw in Sec. 2.7, one phonon per time step can make a big difference in certain situations. It is better to be safe than sorry.

Initialization is basically equivalent to making every cell an internal contact for one time step. Recall from Sec. 2.2 that for initialization, we choose the cell temperatures to be $T_i = T_h - {}^{i}/_{N_c}\left(T_h - T_c\right)$. So, to initialize the system we fill each cell (either by energy or by number) with phonons just as for an internal contact of the same temperature.

[11] This equation is simply a modified version of Eq. (2.12).

2.8.2 Boundary Contacts

The advantage of boundary contacts is that, instead of having to generate all the phonons inside a volume every time step, you only need to generate the phonons which would have entered the simulation domain from an external reservoir. This effectively makes a boundary contact a blackbody that emits phonons into the simulation domain, so we can use results from the theory of blackbody radiation [75], which in turn has much in common with diffuse scattering (Sec. 2.5.1).

The expected number of phonons of branch j and wave vector $\mathbf{k}$ passing through a surface per unit area and time is

$$n_{\text{bb},j}\left(\mathbf{k},T\right)=\left|\mathbf{v}_j\left(\mathbf{k}\right)\right|n_{\text{BE}}\left(\omega_{j,\mathbf{k}},T\right)\cos\theta\frac{d^3\mathbf{k}}{\left(2\pi\right)^3}, \tag{2.46}$$

where θ is the angle between the group velocity $\mathbf{v}_j\left(\mathbf{k}\right)$ and the surface normal. Because we are only interested in the number of phonons entering the domain, we only consider $\theta\in[0,\pi/2]$.

We now turn to the case of an isotropic dispersion relation with $k_{\max}\geq|\mathbf{k}|$ as an upper bound on the wave-vector magnitude. Then $n_{\text{bb},j}\left(\mathbf{k},T\right)$ can be simplified to [72]

$$\begin{aligned} n_{\text{bb},j}\left(\mathbf{k},T\right)&=\int_0^{\pi/2}\int_0^{2\pi}v_j\left(k\right)n_{\text{BE}}\left(\omega_{j,k},T\right)\cos\theta\frac{k^2\sin\theta dkd\theta d\phi}{\left(2\pi\right)^3},\\ &=v_j\left(k\right)n_{\text{BE}}\left(\omega_{j,k},T\right)\frac{k^2}{8\pi^2}dk. \end{aligned} \tag{2.47}$$

Then the total number of phonons entering the simulation domain due to a blackbody of area A in a period of time Δt is

$$\mathcal{N}_{\text{bc}}\left(T\right)=A\Delta t\sum_j\int_0^{k_{\max}}v_j\left(k\right)n_{\text{BE}}\left(\omega_{j,k},T\right)\frac{k^2}{8\pi^2}dk. \tag{2.48}$$

The $\cos$ in Eq. (2.46) means that phonons entering the simulation will have the angular distribution from Lambert's cosine law, so we can generate random directions for the incoming phonons using Eq. (2.18). In principle, the phonons from the boundary contact will enter the simulation domains at different times, but in practice, all the phonons can be added to the simulation domain at the

same time because Δt is small. In practice, that means placing the phonons randomly on the boundary contact.[12]

Then, the overall procedure is to calculate $\mathcal{N}_{\rm bc}\left(T_h\right)$ and $\mathcal{N}_{\rm bc}\left(T_c\right)$ for the hot and cold contacts, which are at temperatures T_h and T_c respectively. Then at each time step, any phonons that exit the simulation domain are deleted and $\mathcal{N}_{\rm bc}\left(T_h\right)$ and $\mathcal{N}_{\rm bc}\left(T_c\right)$ phonons are created at the two contacts using the procedure from Sec. 2.4 except that Eq. (2.47) is used for the k distribution and the angular distribution is given by Lambert's cosine law, Eq. (2.18).

[12]Having the phonons enter at different times would be equivalent to placing the phonons at different distances from the boundary contact determined by a random start time and $\mathbf{v}_{j,\mathbf{k}}$.

Chapter 3

Elastic Continuum Materials in 2D and Finite-Difference Methods

This chapter details our time-dependent and time-independent finite-difference techniques to solve the elastic and scalar wave equations. While the finite-difference methods are not new, I employed them in several novel ways to study phonon dynamics in (Sec. 4.2). In particular, I have developed a method that uses a finite-difference time-domain solution to the elastic wave equation to calculate the thermal conductivities of nanoribbons (Sec. 3.2.2). This chapter closely follows [24] Maurer *et al.*, "Rayleigh waves, surface disorder, and phonon localization in nanostructures," *Phys. Rev. B*, in press.

Elastic continuum materials provide excellent model systems for studying surfaces[1] and their effects on transport and localization. Elastic materials capture the long-wavelength limit of atomic materials [29, 34], and elastic materials support longitudinal acoustic, transverse acoustic, Rayleigh [86, 34, 87, 88], and structure-dependent modes (such as torsional modes for a wire [37]). The study of elastic continuum materials can provide important insights into phonon–surface scattering in atomic materials [34, 48, 89, 51, 90, 91], especially in nanostructures that are too large to model with atomistic techniques, yet too small to be considered bulk [92, 93, 94, 12].

Elastic medium FDTD arguably provides an even better model system for studying phonon–surface interactions than a true elastic continuum material. Finite differences discretize the continuum materials, which makes a finite-difference system similar to an atomic material. It should not

[1] We use the word "surface" to describe any boundary of a structure, so in a 2D ribbon, we will use "surface" and "edge" interchangeably.

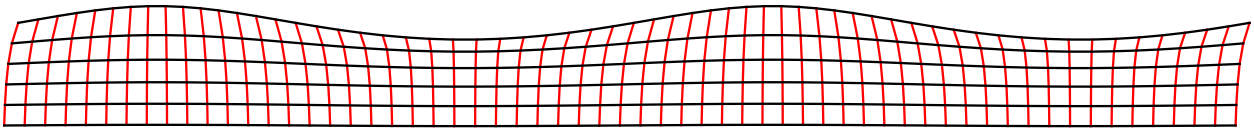

Figure 3.1: Illustration of a Rayleigh wave propagating along the free top surface. The wave amplitude decays exponentially with increasing distance from the surface.

be surprising that finite difference methods can provide a good approximation of atomic materials because of the connection between finite differences and the harmonic approximation of atomic materials (Sec. 1.3). So keep in mind that although we discuss elastic continuum materials, we are really modeling discretized elastic materials with using finite differences. Our system, arguably, has more in common with atomic materials in the harmonic approximation than with continuum elastic materials.

In Sec. 4.2, we will model two-dimensional (2D) graphenelike elastic nanoribbons with random, rough edges (Sec. 1.5). In this system, the only structure-dependent modes are Rayleigh waves (Fig. 3.1), which are a simple type of surface mode that occur only at free surfaces [95, 86, 34, 87, 88] and provide a good starting point for understanding surface modes in general. By switching between fixed and free bounday conditions (BCs) we can selectively "turn off" Rayleigh waves while keeping the surface disorder. We solve the elastic wave equations with the FDTD technique, which is computationally efficient and not limited to weak roughness. We couple the FDTD simulation with the Green-Kubo formula to calculate the thermal conductivity. This combination of FDTD and Green-Kubo has not been used before and has similarities to an equilibrium molecular dynamics (MD) simulation [22, 1] but scales better than MD as the system size increases. This combined technique enables us to simulate large nanostructures with pronounced roughness. We also perform a vibrational eigenmode analysis [96, 97, 98] using time-independent finite-difference (TIFD) methods to further investigate the connection between boundary conditions and localization. Finally, we use TIFD to investigate possible chaotic properties of nanoribbons.

We begin with a review of elastic waves in Sec. 3.1. We include subsections on the elastic wave and scalar wave equations (3.1.1), the utility of the continuum limit in 2D materials (3.1.2),

physically relevant boundary conditions (3.1.4), and an overview of Rayleigh waves (3.1.5). In Sec. 3.2, we introduce the FDTD simulation technique, the structures we simulate (3.2.1), and explain how the method can be used with the Green-Kubo formula to compute thermal conductivity (3.2.2). Sec. 3.2.3 explains the time-independent finite-difference method that we use to solve for normal modes.

The results from our finite-difference simulations are found in Secs. 4.2 and 4.3.

3.1 Review of Elastic Materials

3.1.1 Elastic and Scalar Wave Equations

We consider isotropic, homogeneous, linearly elastic, continuum materials [86, 99]. $\mathbf{u}(\mathbf{r}, t)$ is the displacement of an infinitesimal element of the material. The strain tensor

$$\sigma_{ij} = \frac{1}{2}\left(\partial_j u_i + \partial_i u_j\right) \tag{3.1a}$$

and the stress tensor τ_{ij} are related by the continuum generalization of Hooke's law

$$\tau_{ij} = \lambda \sigma_{ll} \delta_{ij} + 2\mu\sigma_{ij}, \tag{3.1b}$$

where λ and μ are the Lamé parameters, which are material dependent. μ is also known as the shear modulus and $\mu > 0$. Thermodynamic stability requires $\lambda > -\frac{2}{3}\mu$ [86], but $\lambda > 0$ for most materials [35].[2]

Applying Newton's second law to the stress–strain relations yields

$$\begin{aligned} \rho\ddot{\mathbf{u}} &= \nabla \cdot \boldsymbol{\tau} \\ &= (\lambda + 2\mu)\nabla(\nabla \cdot \mathbf{u}) - \mu\nabla \times (\nabla \times \mathbf{u}), \end{aligned} \tag{3.2}$$

where ρ is the density. We will refer to Eq. (3.2) as the *elastic wave equation*, and we will refer to a (vector field) solution of the elastic wave equation as an *elastic wave*.

[2] Hooke's law (and all the equations that follow from it) can be generalized to allow for anisotropy. The generalization requires more material parameters. [29, 34].

The power flux density is [100, 101]

$$\mathbf{J} = -\boldsymbol{\tau}\dot{\mathbf{u}}. \tag{3.3}$$

$\mathbf{J}$ is the elastic wave equivalent of the Poynting vector for electromagnetic waves. For us, $\mathbf{J}$ is the heat current density. We also note that the kinetic energy density is $\rho|\dot{\mathbf{u}}|^2/2$, and the potential energy density is $\sigma_{ij}\tau_{ij}/2$ [86] (using Einstein notation).

We will also consider wave equations of the form $\nabla^2\phi - \frac{1}{c}\ddot{\phi} = 0$, which we will refer to as the *scalar wave equation*, and we will refer to a solution of the scalar wave equation as a *scalar wave*.

By Helmholtz's theorem, $\mathbf{u}$ can be written in terms of a scalar potential ϕ and a vector potential $\boldsymbol{\Psi}$ [86, 99]

$$\mathbf{u} = \nabla\phi + \nabla \times \boldsymbol{\Psi}, \tag{3.4}$$

which allows the elastic wave equation (3.2) to be decomposed into two wave equations, one for longitudinal and one for transverse waves [86, 99]:

$$\nabla^2\phi - \frac{1}{c_l^2}\ddot{\phi} = 0, \tag{3.5a}$$

$$\nabla^2\boldsymbol{\Psi} - \frac{1}{c_t^2}\ddot{\boldsymbol{\Psi}} = 0, \tag{3.5b}$$

where

$$c_l = \sqrt{\frac{\lambda + 2\mu}{\rho}}, \tag{3.6a}$$

$$c_t = \sqrt{\frac{\mu}{\rho}}, \tag{3.6b}$$

are the longitudinal and transverse wave speeds, respectively.

Consider a three-dimensional (3D) slab in the xy plane, effectively a quasi-2D system. For transverse waves in the xy plane, $\boldsymbol{\Psi}$ will always be normal to the plane, i.e., $\boldsymbol{\Psi}_x = \boldsymbol{\Psi}_y = 0$ and $\psi = \boldsymbol{\Psi}_z$ is a scalar field. Thus, the elastic wave equation (3.2) for longitudinal and transverse waves

in a quasi-2D slab can be decomposed into two scalar wave equations, which are independent in an infinite medium and whose solutions are scalar fields ϕ and ψ, respectively.

To study 2D materials rigorously, we take the zero-thickness limit of the quasi-2D, free-standing-slab model. The result is an "elastic plane", which has the same in-plane stress–strain relations as the quasi-2D model, except that λ is modified. To transform the quasi-2D model into a 2D, elastic-plane model, we make the following substitutions in Eq. (3.1b) [86]:

$$\lambda \to \frac{2\lambda'\mu'}{\lambda' + 2\mu'}, \tag{3.7a}$$

$$\mu \to \mu', \tag{3.7b}$$

where the primed quantities are the Lamé parameters for the 3D material that is being formed into a thin plate, and the unprimed quantities can be thought of as 2D Lamé parameters. Materials like single-layer graphene are inherently 2D, so the unprimed 2D Lamé parameters are generally reported in the literature [in which case the substitutions in Eq. (3.7) are unnecessary].

We do not model any out-of-plane modes in this work, but we note that an elastic plane has a single out-of-plane branch. The out-of-plane branch is described by a scalar wave equation of the form $\nabla^4\Phi \propto \ddot{\Phi}$, which results in a quadratic dispersion relation [86]. This quadratic dispersion relation is seen in the long-wavelength limit of graphene ZA modes [102]. The out-of-plane branch is decoupled from the in-plane modes [86], so the out-of-plane branch will not display the mode conversion or surface waves investigated in this work.

As the elastic wave equation in bulk materials can be decomposed into two simpler scalar wave equations, scalar waves are used more often than elastic waves to model phonon–surface scattering [103, 104, 105, 106, 107, 108, 109, 110, 111, 112, 113, 53]. However, the decomposed waves are only independent of each other in an infinite medium. The boundary conditions at surfaces couple the waves together [99]. Without the proper boundary conditions, the wave equations erroneously remain independent, which means they do not capture mode conversion (Sec. 4.2.1), Rayleigh waves (Sec. 3.1.5), or many structure-dependent waves [38].

3.1.2 The Continuum Limit of 2D Materials

The continuum limit is the regime where long-wavelength acoustic phonons in atomic materials behave like elastic waves in continuum materials, i.e., $\omega \approx c|\mathbf{k}|$, where ω is the angular frequency, $\mathbf{k}$ is the wave vector, and c is the wave speed.

The continuum limit is much more important for 2D materials than for 3D materials. The number of phonons per unit angular frequency ω is $N(\omega) = g(\omega) n_{\mathrm{BE}}(\omega)$, where n_{BE} is the Bose-Einstein distribution and g is the density of states. When ω is small, $n_{\mathrm{BE}}(\omega) \approx k_b T/\hbar\omega$. In 3D, the density of states $g_{3D}(\omega) \propto \omega^2$, so $\lim_{\omega\to 0} N_{3D}(\omega) = 0$, i.e., there are relatively few phonons in the continuum limit in 3D [29]. In contrast, the continuum limit of in-plane 2D modes yields the density of states $g_{2D}(\omega) \propto \omega$, so $\lim_{\omega\to 0} N_{2D}(\omega)$ is nonzero [114, 8]. The result is clear in graphene at 300 K [Fig. 3.2(c2)]: a large fraction of the phonons are in the continuum limit. Phonons in the continuum limit also have the highest group velocity of any phonons in the material, along with relatively low scattering rates owing to their long wavelengths [115, 5]. For these reasons – abundance, high group velocity, and low scattering rates – in-plane phonons in the continuum limit are of great significance for the thermal conductivity in 2D materials [116, 117].

The importance of long-wavelength phonons for thermal transport in 2D materials can be grasped by analyzing thermal conductivity in graphene in the relaxation time approximation (Sec. 2.1.1), where[3]

$$\kappa \propto \int k\,dk \int d\theta \sum_j \tau_{j,\mathbf{k}} C_{j,\mathbf{k}} v_{j,\mathbf{k}}^2 \cos^2\theta, \tag{3.8}$$

where the sum is over the branches, $\tau_{j,\mathbf{k}}$ is the relaxation time, $\mathbf{v}_{j,\mathbf{k}}$ is the group velocity, θ is the angle between $\mathbf{v}_{j,\mathbf{k}}$ and the ribbon axis, and $C_{j,\mathbf{k}}$ is the heat capacity per mode. The relaxation times in graphene for umklapp phonon–phonon and isotope scattering are $\tau_{j,\mathbf{k}} \propto \omega^{-2}$ [116, 8]. In the $k \to 0$ limit, $\omega \propto k$, thus $\tau_{j,\mathbf{k}} \propto k^{-2}$. As $v_{j,\mathbf{k}} \to c_j$ and $C_{j,\mathbf{k}} \to k_B$ (k_B is the Boltzmann constant), the divergence in $\tau_{j,\mathbf{k}}$ causes the integrand of Eq. (3.8) to diverge at small k, and κ becomes infinite due to long-wavelength phonons [116].

[3] Eq. (3.8) follows from Eq. (2.11).

In reality, $\tau_{j,\mathbf{k}}$ has a behavior closer to ω^{-1} at low frequencies [118], which will fix the divergence in Eq. (3.8) while retaining a significant contribution from long-wavelength modes. Moreover, no experimental sample has an infinite size, so the lifetime of long-wavelength phonons is limited by scattering from the sample boundaries. The effect of boundaries is often treated via a simple specularity parameter (Sec. 2.5.1). In the case of a nanoribbon, the specularity parameter model for boundary scattering results in a relaxation time [116]: $\tau^{\mathrm{b}}_{j,\mathbf{k}} = \frac{W}{v_{j,\mathbf{k}}}\frac{1+p}{1-p}$, where W is the ribbon width and p is the specularity parameter.

To illustrate the importance of long-wavelength phonons for thermal transport in graphene nanoribbons, we show the contribution to room-temperature thermal conductivity κ [Eq. (3.8)] as a function of wavenumber k [Fig. 3.2(a1)] and frequency f [Fig. 3.2(a2)]; essentially, Figs. 3.2(a1) and (a2) are plots of the integrand from Eq. (3.8) if the integral is over k or over f, respectively. We assume standard umklapp and isotope scattering rates that are quadratic in frequency [119] and isotropic phonon dispersions that fit the full dispersions quite well and contain both linear and quadratic terms [8]. The scattering lifetime of long-wavelength phonons has an upper bound due to scattering from the ribbon edges, and we assume nanoribbon geometry with $W = 25\,\mathrm{nm}$ and a constant specularity parameter of 0.9 [117]; this scattering process will be important only at the center of the Brillouin zone, for very long wavelengths, otherwise it will be overshadowed by phonon–phonon and isotope scattering.

To quantify the range of important wavelengths for thermal transport in graphene, we find the maxima of the curves in Figs. 3.2(a1) and 3.2(a2). The maxima occur at wavenumbers 3.37 and 5.28 1/nm (wavelengths of 1.86 and 1.19 nm) for longitudinal acoustic (LA) and transverse acoustic (TA) phonons, respectively, and are marked with black-orange and black-blue vertical lines throughout Fig. 3.2. These k's correspond to frequencies of 9.33 and 11.0 THz, respectively. The peak wavenumbers in Fig. 3.2(a1) can be considered as roughly the midpoints of the ranges containing the most important wave vectors for thermal conduction; these ranges coincide with the ranges of nearly isotropic dispersions and the continuum limit [see Figs. 3.2(b1) and (b2) for dispersions of TA and LA phonons, respectively, where the constant-wavenumber circles corresponding to the peaks from Fig. 3.2(a1) are denoted in black-blue and black-orange; see also

density of states from full dispersion in Fig. 3.2(c1) and the phonon number per unit frequency in Fig. 3.2(c2)].

Overall, based on the full dispersions and DOS in graphene, we can conclude that the range containing the wave vectors that are the highest contributors to thermal conductivity has considerable overlap with the range in which the approximation of an isotropic elastic solid holds (i.e., the continuum limit).

As an aside, we note that, even though there are relatively few phonons in the continuum limit in 3D materials, elastic waves remain useful for understanding phonon dynamics in 3D. Wave scattering from rough, random surfaces has universal features such as randomizing the direction of the outgoing energy. For that reason, early models of phonon–surface scattering were adapted from electromagnetic-wave scattering [17, 19], and many newer phonon–surface scattering models that are used in 3D are based on scalar and elastic waves [48, 51, 90, 103, 104, 105, 106, 107, 108, 112, 53]. The increased localization due to surface roughness that we see in Sec. 4.2.2 may also exist in 3D.

3.1.3 Our Model System

Because our system is classical, if we truly modeled a continuum material we would suffer from a problem analogous to the "ultraviolet catastrophe": there would be $k_B T$ energy in each of an infinite number of modes, leading to an infinite energy in our system. One way to avoid this problem is to set a cutoff wavelength and only consider modes with longer wavelengths. This happens naturally when we discretize a continuum material using the FDTD method (Sec. 3.2.1.2). To ensure that our model has physical relevance, we choose our cutoff wavelength to be that in graphene. We accomplished this by setting the grid spacing in our system to be the graphene lattice constant (Sec. 3.2.1).

The benefits of our choice of grid spacing can be seen in the bottom right of Fig. 3.2, which shows the density of states [Fig. 3.2(d1)] and phonon number per unit frequency [Fig. 3.2(d2)] in our system. Although our system has fewer continuum phonons than graphene due to Maxwell-Boltzmann statistics [contrast Fig. 3.2(c2) and Fig. 3.2(d2)], most of the phonons in our system

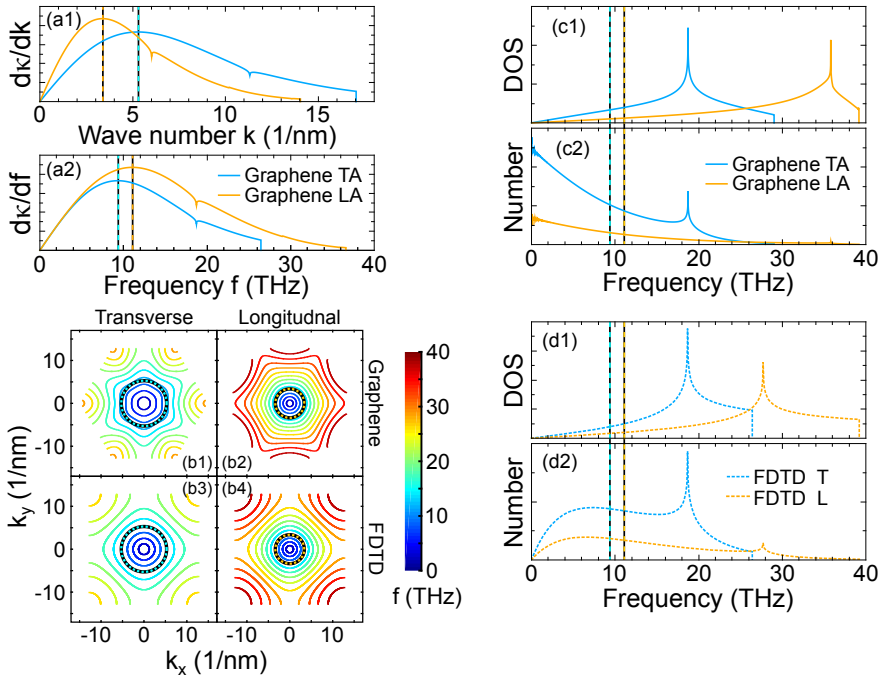

Figure 3.2: Phonon dispersions and thermal transport in graphene and in our graphenelike model system. All temperature-dependent plots are at 300 K. (a1) & (a2) The contribution to thermal conductivity κ from phonons with wavenumbers around k (a1) or frequencies around f (a2). Thermal conductivity is calculated from the RTA and standard umklapp and isotope scattering rates and boundary scattering for a 25-nm-wide ribbon with specularity parameter $p = 0.9$. The maximum contributions for transverse acoustic (TA) and longitudinal acoustic (LA) phonons occur at wavenumbers 3.37 and 5.28 nm^{-1} (a1) (wavelengths of 1.86 and 1.19 nm) and frequencies 9.33 and 11.0 THz (a2), respectively. Dashed black-blue and black-orange lines in all panels indicate the wavenumber or frequency that contribute the most to thermal conductivity from TA and LA modes, respectively. (b1)–(b4) Contour plots of the phonon dispersion relations for graphene TA (b1), graphene LA (b2) [8], FDTD transverse (b3), and FDTD longitudinal (b4) modes [Eq. (3.11)]. Dashed black-blue and black-orange circles mark the peak wavenumbers in (a1). (c1) The density of states (DOS) for TA (blue) and LA (orange) modes in graphene, calculated based on full phonon dispersions [8]. (c2) The number of phonons per unit frequency for graphene, calculated from the DOS (c1) and Bose-Einstein statistics. A large fraction of the graphene phonon population falls in the continuum limit. (d1) The DOS for transverse (blue dashed) and longitudinal (orange dashed) modes in our graphenelike model system. (d2) The number of phonons per unit frequency in our graphenelike model system based on the DOS from (d1). The system is classical, so the phonon number per unit frequency is calculated with Maxwell-Boltzmann statistics and tends to zero at low frequencies. However, a large fraction of the phonon population is still in the continuum limit, and the population is sizeable at the frequencies of maximum contribution to thermal conductivity.

still fall in the continuum limit. Also note the similarities in the cutoff frequencies and Van Hove singularities between graphene [Fig. 3.2(c1)] and our graphenelike system with a grid-cell size equal to the graphene lattice constant [Fig. 3.2(c2)]. Without appropriate discretization our system would not have these similarities to graphene [114].

We emphasize that our graphenelike model system is not intended for a direct and quantitative simulation of real graphene samples; e.g., the model system is harmonic, while graphene has anharmonicity. Still, our model system has many common features with graphene. For instance, Figs. 3.2(b1)–(b4) show the full dispersion relations for graphene [8] in panels (b1) and (b2) versus those obtained for our graphenelike FDTD simulation [Eq. (3.11)]. The graphene and FDTD dispersion relations are in good agreement up to the k's of maximum contribution to thermal conductivity in the diffusive regime (marked with vertical dashed lines); the agreement worsens at higher k, which is particularly pronounced for TA phonons (although the DOS remains in good agreement for TA phonons). Finally, we see in Fig. 3.2(d2) that our FDTD simulation has a sizeable population of phonons at and above the frequency of maximum contribution to thermal conductivity.

In short, while our FDTD simulation neither truly models atomistic graphene nor a perfect continuum 2D material, it is a good hybrid that provides useful insight into both.

3.1.4 Boundary Conditions

At the surface, we consider both fixed (Dirichlet) and free (Neumann) boundary conditions (BCs). Let $\hat{\mathbf{n}}$ be the surface normal vector. For elastic waves, the fixed BC is $\mathbf{u} = 0$ and the free BC is $\boldsymbol{\tau}\hat{\mathbf{n}} = 0$. For scalar waves, the fixed BC is $\phi = 0$ and the free BC is $\nabla\phi \cdot \hat{\mathbf{n}} = 0$.

Free-standing nanostructures (such as suspended graphene nanoribbons) have unrestrained surfaces, which are equivalent to free BCs. We also analyze fixed BCs, because fixing the boundaries enables us to "turn off" Rayleigh waves, which exist only for elastic waves near a free surface. (Studying fixed BCs may also be useful for understanding nanostructures with edges that are not entirely free, such as in supported graphene nanoribbons.)

3.1.5 Rayleigh Waves

There are many types of surface waves in atomic and inhomogeneous elastic materials [87, 35, 88]. Graphene nanoribbons are no exception and support a number of in-plane and out-of-plane edge modes, with properties that depend on the terminating atoms [120]. (Thermal transport in supported graphene will also be affected by Rayleigh waves in the substrate [121]; the substrate Rayleigh waves result in out-of-plane motion of the nanoribbon and are not considered here.)

For the uniform elastic materials we consider here, Rayleigh waves (Fig. 3.1) are the only type of surface wave [35]. Here, we briefly review some important facts about Rayleigh waves [95, 86].

The general form for a Rayleigh wave propagating in the x-direction near the surface of a semi-infinite bulk material ($y \geq 0$) is given by

$$\begin{aligned}\mathbf{u}\left(x,y,t\right) = e^{i(kx-\omega t)} \big[&\left(a\gamma_t e^{-\gamma_t y} + bke^{-\gamma_l y}\right)\hat{\mathbf{x}} \\ &- i\left(ake^{-\gamma_t y} + b\gamma_l e^{-\gamma_l y}\right)\hat{\mathbf{y}}\big] ,\end{aligned} \tag{3.9}$$

where k is the wavenumber, ω is the angular frequency, a and b capture the amplitude of the wave at the surface, and γ_l and γ_t capture the exponential decay of amplitude away from the surface. Rayleigh waves result in a "rolling" motion, where $\mathbf{u}$ rotates 360 degrees each period.

Rayleigh waves have a linear dispersion relation, $\omega = c_r k$, where c_r is the Rayleigh-wave group velocity. c_r has a complicated dependence on the Lamé parameters. For $\lambda > 0$, $0.874c_t < c_r < 0.955c_t$. For the graphenelike Lamé parameters we use here (see Sec. 3.2.1), $c_r = 0.89c_t$, $\gamma_l = 2.19k$, $\gamma_t = 3.85k$, and $a = 1.32b$.

Rayleigh waves are slower than transverse or longitudinal waves, extend into the structure a distance comparable to their wavelength, and can only exist with free BC because they have a nonzero displacement at the surfaces. Since a Rayleigh wave is a type of elastic wave, it can be decomposed into two scalar waves. The two scalar waves that represent a Rayleigh wave are not independent, but are coupled together by the free boundary condition [99]. Applying the free boundary conditions separately to the two scalar waves ($\nabla\phi\cdot\hat{\mathbf{n}} = 0$, $\nabla\psi\cdot\hat{\mathbf{n}} = 0$) is *not* equivalent to the free boundary condition for an elastic wave ($\boldsymbol{\tau}\hat{\mathbf{n}} = 0$). While two interdependent scalar waves

are needed to form a Rayleigh wave, most existing scalar phonon–surface scattering models only use a single scalar wave [103, 104, 105, 106, 107, 108, 112, 53] and thus do not capture Rayleigh waves.

3.2 Finite-Difference Methods

3.2.1 The Finite-Difference Time-Domain Method for the Elastic and Scalar Wave Equations

We solve the elastic (3.2) and scalar (3.5) wave equations in our structures using the finite-difference time-domain method, which is an efficient technique that discretizes the wave equation in both space and time by replacing the partial derivatives with finite differences. While the FDTD method is best known for solving the electromagnetic wave equations [122, 123], the method has been used with many wave equations, such as the Schrödinger [124, 125], Klein-Gordon [124], scalar [126], and elastic wave equations [127, 128]. Elastic-medium FDTD has been used to investigate transmission through superlattices [129] and phononic materials [130, 131, 132], but it had not been used before to calculate thermal conductivity.

Unlike many methods used to investigate elastic materials, elastic-medium FDTD is not limited to weak roughness or to any specific geometry. The technique is computationally simple and fast; the core of the simulation requires only a few lines of element-wise array operations, which can be computed quickly on modern processors.

Our FDTD method faithfully reproduces elastic waves with wavelengths greater than about 10 grid cells [133], but gradually becomes less accurate at shorter wavelengths, which are also outside the continuum limit of atomic solids.

We use graphenelike Lamé parameters from [134]: $\lambda = 32.0\ \mathrm{J/m^2}$ and $\mu = 160.2\ \mathrm{J/m^2}$. (Equivalently, $c_l = 2.14\times10^4\ \mathrm{m/s}$ and $c_t = 1.44\times10^4\ \mathrm{m/s}$.) We choose the grid-cell size, denoted h, to be the graphene lattice constant (h=0.246 nm), which means that the shortest wavelength in our system will be similar to that in graphene. We will use h as a unit of length. Our choice of material parameters and h sets the stability condition for the simulation timestep $\Delta t < h/c_l\sqrt{2}$ [128]. We chose $\Delta t = 0.95$ fs, one tenth of the maximum allowed value. Our timestep is comparable

to the 0.1-0.5 fs often used in graphene MD simulations [135, 136, 137, 94, 138]. We simulate 100h-wide (24.6 nm) nanoribbons with random surface roughness that has a Gaussian autocorrelation function $C_g(x) = \Delta^2 e^{-x^2/\xi^2}$, where Δ and ξ are the rms roughness and correlation length, respectively. The details for generating these random surfaces are given in Sec. 1.5.

While the elastic wave equation (3.2) can be directly solved with the FDTD method to obtain $\mathbf{u}$ [127], we instead use the velocity-stress formulation [128] because it allows for a simple and stable implementation of free BCs and because the velocity and stress are ultimately what we need to find $\mathbf{J}$ [Eq. (3.3)].

Taking the time derivatives of the strain equation (3.1a), Hooke's law (3.1b), and elastic wave equation (3.2) while defining $\mathbf{v} = \dot{\mathbf{u}}$ yields:

$$\dot{\sigma}_{ij} = \frac{1}{2}\left(\partial_j v_i + \partial_i v_j\right), \tag{3.10a}$$

$$\dot{\tau}_{ij} = \lambda \dot{\sigma}_{ll}\delta_{ij} + 2\mu\dot{\sigma}_{ij}, \tag{3.10b}$$

$$\rho\dot{\mathbf{v}} = \nabla \cdot \boldsymbol{\tau}. \tag{3.10c}$$

The elastic wave equation is thus broken into two first-order differential equations. [Although there are three equations above, $\dot{\boldsymbol{\sigma}}$ and $\dot{\boldsymbol{\tau}}$ are linearly related via Hooke's law, Eq. (3.1b).] The velocity-stress formulation [128] solves for the stress–strain and velocity using a leapfrog technique on a staggered, square grid (See Fig. 3.3). We found that the second-order-accurate [128] and fourth-order-accurate [139] spatial finite difference operators were both stable and suitable for our purposes. We used the second-order-accurate operator because it is computationally simpler.

The second-order-accurate method is based around centered finite difference operators to approximate the spatial derivatives in Eq. (3.10) [128]. The details of the finite differences can be worked out from Fig. 3.3. For example, Eq. (3.10c) implies that $\rho\dot{v}_x = \partial_x\tau_{xx} + \partial_y\tau_{xy}$. Using superscripts to denote the grid cell, $v_x^{i,j}$ is in the center of Fig. 3.3 with $\tau_{xx}^{i,j+1}$ to its right, $\tau_{xx}^{i,j}$ to its left, $\tau_{xy}^{i,j}$ above, and $\tau_{xy}^{i+1,j}$ below. So $\partial_x\tau_{xx} \approx \left(\tau_{xx}^{i,j+1} - \tau_{xx}^{i,j}\right)/h$. Similarly, $\partial_y\tau_{xy} \approx \left(\tau_{xy}^{i,j} - \tau_{xx}^{i,j+1}\right)/h$. There are other ways to number the grid cells, and the details of the finite difference operators may be different, but the same approach can be used.

To implement free boundaries, we used the "vacuum formalism," where materials parameters μ, λ, and ρ^{-1} are set to zero outside the structure. For accuracy and stability, a half-grid-cell-thick fictitious layer of material is added around the structure to ease the transition from the material to vacuum [139]. Fixed BCs are simpler to implement: we force $\mathbf{v} = 0$ on the surface.

The 2D scalar wave equation can be recovered by taking the 3D elastic wave equation and setting $\partial_z v_z = 0$. To keep our elastic and scalar FDTD methods consistent, we take the 3D generalization of our elastic wave FDTD technique [140] and set $\partial_z \dot{v}_z = 0$. The result of this matematical convience is a 2D scalar wave equation FDTD method. (The method can also be derived directly [126].) Free and fixed BCs are enforced by setting the stress or velocity, respectively, to zero on the surface.

Because we simulate a linear elastic material, our model does not include phonon–phonon scattering, which would imply a nonlinear restoring force in the wave equation [33]. Our simulation is suitable for investigating structures where surface or boundary roughness is the dominant scattering mechanism.

3.2.1.1 Energy Conservation in Long Simulations

The elastic wave FDTD technique was originally developed to model earthquakes [127, 141]. Many commonly used free-surface implementations are known to have long-term instabilities [142]; however, these instabilities are not an issue for typical seismic simulations, which are often short and have absorbing boundary conditions along some domain edges. In contrast, our simulations require stability and energy conservation even for very long simulations (millions of timesteps). It had not been previously reported that the combination of BCs and FDTD method we report here is energy-stable [143].

Figure 3.4 shows the energy in the system as a function of time. The simulation is initialized with only kinetic energy (Sec. 3.2.2), but half of the kinetic energy becomes potential energy within the first 0.5 ps of the simulation. Although the total energy is stable after an initial transient, the steady-state energy is about 1.8% higher than the initial kinetic energy. The steady-state energy

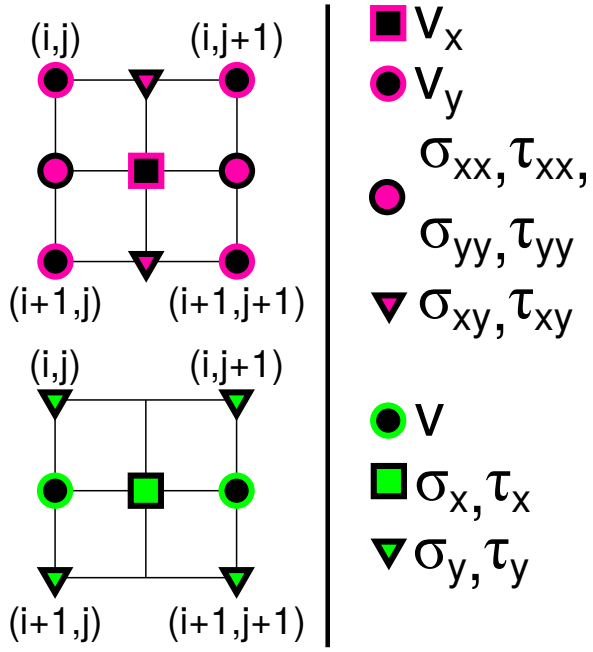

Figure 3.3: The staggered grid used for the FDTD solution to the elastic (top) and scalar (bottom) wave equations. (i, j) enumerate the grid cells along the x and y directions. The symbols (squares, triangles, and circles) show where on the grid the different components of $\mathbf{v}$, $\boldsymbol{\sigma}$, and $\boldsymbol{\tau}$ are defined.

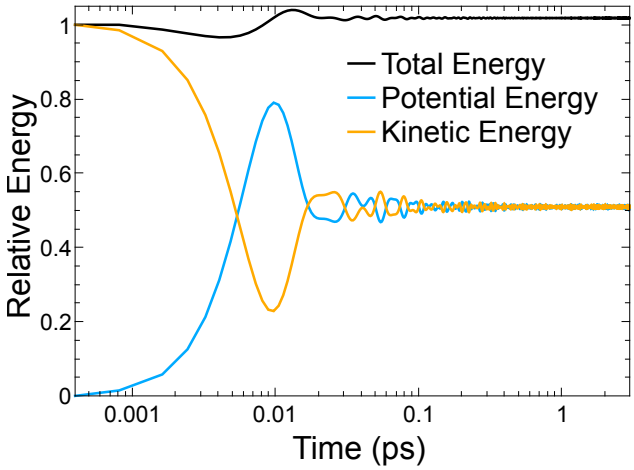

Figure 3.4: Energy in a FDTD simulation relative to the initial energy. Initially, all the energy is kinetic energy (orange), but half the energy is potential energy (blue) by 0.5 ps. The steady-state total energy is about 1.8% higher than the initial energy, but the total energy is very stable after an initial transient.

(not initial energy) should be used to calculate the system temperature T for use in the Green-Kubo formula [Sec. 3.2.2 and Eq. (3.12)].

3.2.1.2 Effects of Discretization

Discretizing wave equations introduces dispersion and anisotropy to the dispersion relations. Dispersion and anisotropy are undesirable for modeling continuum materials. However, as we ultimately care about phonons in atomic materials, which also have dispersion and anisotropy, discretization can actually bring the elastic medium model closer to an atomic model, as we saw in Sec. 3.1.3. The dispersion relation for our FDTD method is [128]:

$$\omega_i = \frac{2}{\Delta t} \arcsin\left(\frac{c_i \Delta t}{h} \sqrt{\sin^2 \frac{hk_x}{2} + \sin^2 \frac{hk_y}{2}} \right), \tag{3.11}$$

where $\mathbf{k}$ is the wave vector, and i can be either l or t for longitudinal or transverse phonons, respectively. Dispersion relations of this form are common to other FDTD methods [123].

The argument of the $\arcsin$ is small because $\frac{c_i \Delta t}{h}$ in our system equals 0.07 and 0.05 for longitudinal and transverse phonons, respectively, so we can approximate $\arcsin(x) \approx x$ and get a dispersion relation very similar to the classic dispersion relation for a periodic one-dimensional lattice with harmonic potentials $\omega \propto |\sin(hk/2)|$ (Sec. 1.3.3). In the limit of small $|\mathbf{k}|$, Eq. (3.11) becomes the dispersion relation for continuum materials: $\omega_i = c_i |\mathbf{k}|$.

We also note that it is possible to explicitly add anisotropy to elastic-material FDTD simulations at the cost of additional complexity [144, 145]. It should also be possible to implicitly change the anisotropy by choosing grids with different geometries. For example, a hexagonal grid [123] should lead to a dispersion relation with hexagonal symmetry.

Discretization also leads to minimum wavelengths for waves in the system. For bulk waves (transverse and longitudinal), the shortest wavelength is two grid cells ($2h$) with displacements that alternate $\rightarrow, \leftarrow$ or $\uparrow, \downarrow$ for longitudinal and transverse waves, respectively, that propagate in the horizontal direction. However, Rayleigh waves correspond to a "rolling" motion (Sec. 3.1.5) which cannot be captured with just two grid cells. Thus, the shortest wavelength for Rayleigh waves in our model is four grid cells ($4h$), with displacements that cycle $\uparrow, \leftarrow, \downarrow, \rightarrow$ for a wave

propagating in the horizontal direction. In the absence of dispersion, this minimal wavelength corresponds to a cutoff frequency of $c_r/4h \approx 13$ THz for Rayleigh waves. (c_r is defined in Sec. 3.1.5.) Other frequencies that will be important later correspond to the shortest wavelength for waves propagating at a 45 degree angle from the ribbon axis. That corresponds to a wavelength of $2^{3/2}h$ and frequencies of $\frac{c_l}{2^{3/2}h} \approx 31$ THz and $\frac{c_t}{2^{3/2}h} \approx 21$ THz for longitudinal and transverse waves, respectively.

3.2.1.3 FDTD vs. Molecular Dynamics

Because of the discretization, our FDTD model has similarities to a molecular dynamics simulation, with springlike nearest-neighbor potentials and with the discretized material elements playing a similar role to atoms in MD. The primary advantages of an FDTD simulation over an MD simulation are simplicity, scalability, and computational speed. We can simulate relatively large structures with significantly less computational cost than an MD simulation. The trade-off is that our FDTD method cannot accurately account for the short-wavelength limit or anharmonic potentials of atomic materials. The harmonic potentials and classical statistics also mean that our thermal conductivity is independent of temperature.

3.2.2 Thermal Conductivity Calculation

We compute the thermal conductivity in a similar way to an equilibrium molecular dynamics simulation [22, 1]. First, we initialize all the discretized elements with random velocities drawn from a Maxwell-Boltzmann distribution. The simulation can become unstable if the net momentum is too far from zero. Because we draw a finite number of samples from the Maxwell-Boltzmann distribution, the net momentum will be small but nonzero. So, before starting the simulation we adjust the velocities so that the structure has zero net momentum. We likewise adjust the velocities so that the kinetic energy is equally divided between the x and y motion, x being along the nanoribbon. All our nanoribbons have periodic boundary conditions in the x direction (along the axis of the ribbon), so energy neither leaves nor enters the simulation.

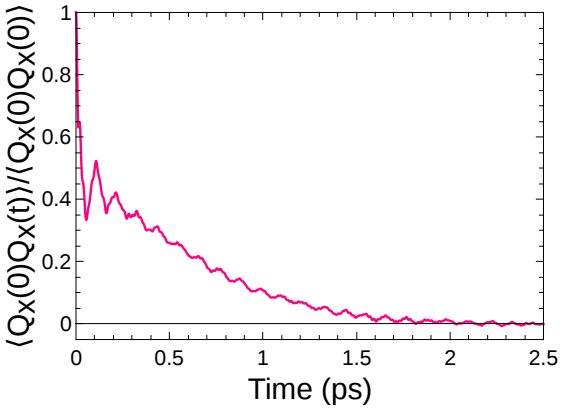

Figure 3.5: Representative heat-current autocorrelation function (HCACF) from our FDTD simulation. The curve is similar to those obtained for equilibrium molecular dynamics simulations [1].

We run the simulation for 100,000 timesteps to let the system equilibrate. Then, the simulation runs an additional 900,000 timesteps in equilibrium. At each timestep, we calculate the heat current $\mathbf{Q}$, which is the spatial integral of the heat-current density $\mathbf{J}$ [Eq. (3.3)].[4] Finally, we calculate the thermal conductivity κ using the Green-Kubo formula (Sec. 1.4):

$$\kappa = \frac{1}{k_B T^2 V} \int_0^\infty \langle Q_x(0)\, Q_x(t) \rangle \, \Delta t \,, \tag{3.12}$$

where T is the system temperature, V is the system volume, and the x-axis is along the ribbon. To calculate the system volume, we use the standard technique of multiplying the surface area by the graphite interplanar distance of 0.335 nm [94]. We directly compute the integral and cut it off after the first dip, when the heat-current autocorrelation function $\langle Q_x(0)\, Q_x(t) \rangle$ first reaches zero [1]. Figure 3.5 shows that the heat-current autocorrelation function obtained via FDTD has a temporal dependence similar to that obtained in MD simulations (Fig. 1.2), underscoring the similarity between the two techniques.

3.2.3 Time-Independent Finite-Difference Method for Finding Normal Modes

Finite-difference methods can also find normal modes of the system, which are time-independent. The FDTD update equations [Eq. (3.10)] are a set of linear equations that can be written in matrix form

$$\mathbf{M}\mathbf{s}_i = \mathbf{s}_{i+1}, \tag{3.13}$$

where $\mathbf{s}_i$ is a vector that holds the stress and velocity components at every grid cell at timestep i, and $\mathbf{M}$ is a matrix that encodes the linear equations that advance the simulation by one timestep [the right side of Eq. (3.10)]. For example $\mathbf{s}_i$ could be written

$$\mathbf{s}_i = \left(v_x^{0,0,i}, v_y^{0,0,i}, \tau_{xx}^{0,0,i}, \tau_{yy}^{0,0,i}, \tau_{xy}^{0,0,i}, v_x^{0,1,i}, v_y^{0,1,i}, \tau_{xx}^{0,1,i}, \tau_{yy}^{0,1,i}, \tau_{xy}^{0,1,i} \ldots \right)^T, \tag{3.14}$$

[4] Calculating $\mathbf{J} = -\boldsymbol{\tau}\mathbf{v}$ [Eq. (3.3)] requires multiplying stress and velocity components. (E.g., $J_x = -\tau_{xx} v_x - \tau_{xy} v_y$.) However, the stress and velocity components are defined at different locations within a grid cell (Fig. 3.3), so for the velocity, we use the average value of the two velocity components neighboring each stress component. (E.g., $J_x^{i,j} = -\tau_{xx}^{i,j} \left(v_x^{i,j} + v_x^{i,j-1}\right)/2 - \tau_{xy}^{i,j} \left(v_y^{i,j} + v_y^{i-1,j}\right)/2$, where the superscripts are the grid indices used in Fig. 3.3.)

where the superscripts indicate the grid cell and timestep. $\mathbf{M}$ is a sparse matrix that is similar to a matrix representing a tight-binding Hamiltonian. E.g., $\sigma_{xx}^{0,0}$ depends on $v_x^{0,1}$, so there will be a nonzero matrix element connecting the two.

We can find the eigenvalues and eigenvectors of $\mathbf{M}$

$$\mathbf{M}\mathbf{s}_n = \lambda_n \mathbf{s}_n, \tag{3.15}$$

where $\mathbf{s}_n$ are eigenvectors and λ_n are eigenvalues. Comparing Eqs. (3.13) and (3.15), we see that $\mathbf{s}_n$ must represent a normal mode of the system because it is unchanged by the update matrix (up to a constant factor). For the system to be stable, it must be that $|\lambda_n| = 1$, so λ_n must represent a phase factor. In fact, $\lambda_n = e^{i\omega_n \Delta t}$, where ω_n is the angular frequency of the mode.[5]

The above method works, but it results in very large matrices. In most situations, $\mathbf{s}_n$ contains more data than we need. Often we only need the velocities, not the stresses. So, if we can avoid storing the stresses, then we can shrink the matrix by a factor of $(3/5)^2$ and greatly speed up the calculations while also reducing memory usage.

So, we developed a method to calculate the velocities alone by making use of the leapfrog scheme in the FDTD simulation. Instead of using the single matrix in Eq. (3.13), we can instead use two matrices ($\mathbf{M}_\tau$ and $\mathbf{M}_v$) to write the equations as

$$\mathbf{M}_\tau \mathbf{s}_{\tau,i} = \mathbf{s}_{v,i+1/2} - \mathbf{s}_{v,i-1/2}, \tag{3.16a}$$

$$\mathbf{M}_v \mathbf{s}_{v,i+1/2} = \mathbf{s}_{\tau,i+1} - \mathbf{s}_{\tau,i}, \tag{3.16b}$$

where $\mathbf{s}_\tau$ and $\mathbf{s}_v$ hold only the stress or velocity components, respectively. (We will later refer to $\mathbf{s}_v$ as the velocity-polarization vector, which we make extensive use of in Sec. 4.2.2.) Because we are using a leapfrog scheme, the two vectors are defined a half timestep apart. The right side of the above equations may seem strange, but it follows from the fact that Eq. (3.10) defines changes in the stress and velocity, and the right side of Eq. (3.16) represents the changes. $\mathbf{M}_\tau$ operates on the

[5] Just like for a stationary state of the Schrödinger equation.

stresses to update the velocities [i.e., Eq. (3.10c)], while $\mathbf{M}_v$ operates on the velocities to update the stresses a half timestep later [i.e., Eqs. (3.10a) and (3.10b)].

For normal modes, it must be that

$$\mathbf{s}_{v,i+1/2} = e^{i\omega\Delta t}\mathbf{s}_{v,i-1/2}, \tag{3.17a}$$

$$\mathbf{s}_{\tau,i+1} = e^{i\omega\Delta t}\mathbf{s}_{\tau,i}, \tag{3.17b}$$

so we can rewrite Eq. (3.16) as

$$\mathbf{M}_\tau\mathbf{s}_{\tau,i} = \mathbf{s}_{v,i+1/2} - \mathbf{s}_{v,i-1/2} = \left(1 - e^{-i\omega\Delta t}\right)\mathbf{s}_{v,i+1/2}, \tag{3.18a}$$

$$\mathbf{M}_v\mathbf{s}_{v,i+1/2} = \mathbf{s}_{\tau,i+1} - \mathbf{s}_{\tau,i} = \left(e^{i\omega\Delta t} - 1\right)\mathbf{s}_{\tau,i}. \tag{3.18b}$$

Combining the two yields

$$\mathbf{M}_\tau\mathbf{M}_v\mathbf{s}_{v,i+1/2} = \left(1 - e^{-i\omega\Delta t}\right)\left(e^{i\omega\Delta t} - 1\right)\mathbf{s}_{v,i+1/2}. \tag{3.19}$$

$\mathbf{s}_{v,i+1/2}$ is then an eigenvector with eigenvalue $\left(1 - e^{-i\omega\Delta t}\right)\left(e^{i\omega\Delta t} - 1\right)$.

So, the procedure to find normal modes is to find the eigenvectors and eigenvalues of the matrix $\mathbf{M}_\tau\mathbf{M}_v$. The eigenvectors are the velocity-polarization vectors of the normal modes and the eigenvalues $\lambda_n = \left(1 - e^{-i\omega_n\Delta t}\right)\left(e^{i\omega_n\Delta t} - 1\right)$, which can be solved for ω_n

$$\begin{aligned}
\lambda_n &= \left(1 - e^{-i\omega_n\Delta t}\right)\left(e^{i\omega_n\Delta t} - 1\right), \\
&= e^{i\omega_n\Delta t} - 1 - 1 + e^{-i\omega_n\Delta t}, \\
&= 2\cos\left(\omega_n\Delta t\right) - 2, \\
\omega_n &= \frac{\arccos\left(1 + \lambda_n/2\right)}{\Delta t}.
\end{aligned} \tag{3.20}$$

λ_n must be real and $\lambda_n \leq 0$ to get real ω_n. All the λ_n that I have seen meet these conditions, although eigensolvers tend to give λ_n an extremely small imaginary part (often order 10^{-18}), possibly due to rounding errors. So, only the real part of λ_n should be used in Eq. (3.20).[6] Eigensolvers will also find zero-frequency modes caused by grid cells that are outside the ribbon. These zero-frequency modes can be discarded.

[6]There are specialized eigensolvers that work only on symmetric matrices and only return real eigenvalues. However $\mathbf{M}_\tau \mathbf{M}_v$ will not be a symmetric matrix in general, so you must use general eigensolvers, which return complex numbers.

Chapter 4

Results

This Chapter contains the major results of my work. Section 4.1 draws on the PMC methods described in Chapter 2 to model silicon nanowires. Our results help explain the unexpectedly low thermal conductivities seen in rough silicon nanowires. These results are contained in [23].

In Sec. 4.2, we apply the tools of elastic medium finite differences (Chapter 3) to investigate phonons in rough nanoribbons. The project was originally meant to be a straightforward investigation of phonon–surface scattering, but the project bloomed into an investigation of surface waves and mode localization in nanoribbons. These results are contained in [24].

We continue our investigations of discretized elastic media in Sec. 4.3 by studding their normal modes in detail to find signs of wave chaos.

4.1 Phonon Monte Carlo Simulation of Silicon Nanowires

As discussed in the introduction (Sec. 1), a prominent open problem in the field of nanoscale phonon transport is the unexpectedly low thermal conductivity of very rough silicon nanowires [20, 9, 146]. Earlier measurements on vapor-liquid-solid (VLS)-grown SiNWs showed κ an order of magnitude lower than the bulk value [32]. These results could largely be explained within the diffusive-transport framework and a specularity-parameter model for surface scattering (Sec. 2.5.1). Indeed, thermal transport in many relatively smooth SiNWs is well described using the relaxation-time approximation (Sec. 2.1.1) and the model of partially or completely diffuse surface scattering [147, 148, 32, 149, 12]. In contrast, the κ's measured on electrolessly etched [20] or intentionally roughened VLS-grown [9] SiNWs are far below the Casimir limit (Sec. 2.5.1) and

have values similar to amorphous materials. Several groups have calculated the κ of SiNWs in the presence of periodic or rough surface features by molecular dynamics [150, 151, 152], elastodynamics or hydrodynamics [48, 53, 51, 153], solving the phonon Boltzmann transport equation (BTE) [149, 154, 155, 148, 156, 157, 158, 26], or within coherent transport formalisms [159, 160, 161, 50, 162]. The unusually low thermal conductivity has been linked to diverse mechanisms, such as the need to include full dispersion [149], different surface-scattering rates for phonons of different energies [161, 49], a surrounding native oxide that might randomize phonon phase [152, 12], internal defects [146, 152], and multiple coherent backscattering events from highly correlated surfaces [50, 162]. Lim *et al.* [9] performed a systematic experimental study of the surface condition of intentionally roughened VLS-grown SiNWs, revealing correlation lengths smaller than previously assumed [50] and underscoring the importance of surface-roughness profile in nanoscale thermal transport.

In the remainder of this section, we show that the ultralow measured thermal conductivities in intentionally roughened SiNWs can be reproduced in phonon Monte Carlo simulation with exponentially correlated real-space rough surfaces similar to experiment [9]. We demonstrate that the normalized geometric mean free path $\bar{\Lambda}$ serves as a universal quantifier of surface roughness; $\bar{\Lambda} = 1/2$ corresponds to the Casimir limit. $\kappa(\bar{\Lambda})$ is exponential at low roughness (high $\bar{\Lambda}$), where internal scattering competes with roughness scattering, and linear at pronounced roughness (low $\bar{\Lambda}$), where multiple successive scattering events from the same surface dominate and result in ultralow, amorphous-limit κ.

4.1.1 System and Methods

We consider long SiNWs with square cross-sections and rough surfaces (as described in Sec. 1.5). Most previous studies that included correlated roughness used either Gaussian [48, 49, 50, 51, 52] or Gaussian-based [53] ACFs. However, measurements of Si/SiO_2 interfaces found exponential [54] or exponential/Gaussian hybrid ACFs [55]. Hybrid ACFs have also been found on SiNWs [162, 9]. Therefore, we consider surfaces with both exponential and Gaussian ACFs (exponential and Gaussian surfaces, for brevity). Fig. 1.3 shows exponential and Gaussian surfaces; the salient

difference between the two is that the exponential surfaces have much more short-scale roughness than the Gaussian surface. In the simulation, each SiNW surface has a random roughness profile generated numerically with the technique from Sec. 1.5.

The SiNWs we consider have widths 20-70 nm and are approximately 2 μm long, much longer than the room-temperature bulk phonon mean free path [163], so transport is scattering-limited (diffusive) and described by the PBTE (Sec. 2.1). We use PMC (Sec. 2.2) to solve the PBTE because PMC can incorporate real-space roughness and simulate the SiNWs of experimentally relevant sizes. Bulk dispersion relations are reasonable for SiNWs thicker than a few tens of nanometers [147, 149, 148], and for simplicity, we use isotropic, quadratic dispersion relation for each acoustic branch [164]:

$$\omega_{j,k} = c_j k + d_j k^2. \tag{4.1}$$

For the two transverse branches $c_t = 5.23 \times 10^3$ ms^{-1} and $d_t = -2.26 \times 10^{-7}$ m^{2}s^{-1}. For the longitudinal branch $c_l = 9.01 \times 10^3$ ms^{-1} and $d_l = -2.00 \times 10^{-7}$ m^{2}s^{-1}. These constants were found by fitting a quadratic curve to the measured silicon phonon dispersion relation in the (100) direction and provide a good approximation for the full dispersion relations [164].

Finally, we use boundary contacts (Sec. 2.8.2), whose temperatures differ by 20 K, and the internal scattering mechanisms described in Sec. 2.6.

4.1.2 Thermal Conductivity Calculations

Figure 4.1 presents the results of PMC simulations for a large ensemble of 70-nm-wide SiNWs, akin to those measured by Lim *et al*. [9]. The rough surfaces were generated according to exponential or Gaussian ACFs, with a broad range of roughness parameters, Δ=0-5.5 nm and ξ=3-16 nm; this range includes experimental values [9]. As expected, κ decreases with increasing Δ and increases with increasing ξ (the surface "looks" smoother with a higher ξ [2]). Exponential surfaces have more small-scale roughness, and consequently have lower κ, because they are more effective at scattering short-wavelength phonons than their Gaussian counterparts with the same roughness parameters. Furthermore, κ calculated with real-space roughness is below the Casimir limit (about

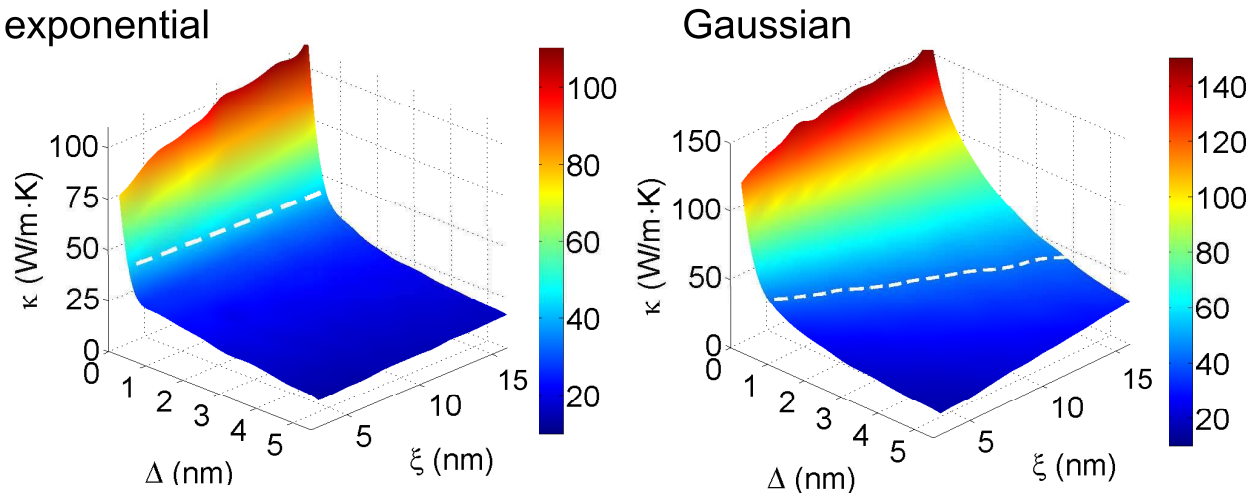

Figure 4.1: Room-temperature thermal conductivity κ versus rms roughness Δ and correlation length ξ for 70-nm-wide SiNWs with exponential (left panel) and Gaussian (right panel) autocorrelation functions. The Casimir limit for SiNWs of this width, approximately 42.7 W/m·K, is shown with a dashed white line.

42.7 W/m·K for 70-nm SiNWs and shown in a white dashed line in Fig. 4.1) over a wide range of Δ and ξ for both exponential and Gaussian surfaces. The Casimir limit was calculated using PMC by using diffuse boundary scattering (Sec. 2.5.1) along with the normal internal scattering mechanisms (Sec. 2.6).

Figure 4.2 shows κ versus Δ for Soffer's specularity-parameter model (Sec. 2.5.1), which assumes $\xi = 0$, and for exponential and Gaussian surfaces with different values of ξ (5, 9, and 13 nm). The exponential curves and the specularity model agree up to about $\Delta \approx 0.5\,\mathrm{nm}$, which is on the order of the average phonon wavelength, after which the specular curve saturates at the Casimir limit. Moreover, our results for exponential surfaces are very close to experiments on intentionally roughened SiNWs of similar diameters and surface-roughness parameters [9]. The slight discrepancy might stem from isotropic rather than full dispersions [161, 8], the fact that the measured SiNWs appear to have a hybrid rather than purely exponential ACF [9], and not accounting for the native oxide [152].

4.1.3 Thermal Conductivity and the Geometric Mean Free Path

Thermal conductivity includes the effects of both internal and roughness scattering; their relative importance depends in a complicated manner on the temperature, wire width W, the ACF, and the surface-roughness parameters Δ and ξ. Focusing on surface scattering alone, we note that a SiNW can be considered a cavity, so we can calculate the geometric mean free path $\Lambda = \frac{4V}{S}$, where V is the cavity volume and S is its surface area (Sec. 1.6.1). Our wires have only small openings at the ends, so they resemble closed cavities, and numerical computations of Λ in our SiNWs shows them to be almost identical to the closed-cavity values. A long square SiNW of length L has $V = LW^2$ (since the average height of rough surfaces is zero) and $S \geq 4WL$ (the rougher the SiNW, the larger its surface area), thus $\Lambda \leq W$. Therefore, we define the normalized geometric mean free path, $\bar{\Lambda} = \Lambda/W$ ($0 \leq \bar{\Lambda} \leq 1$), which enables us to compare across different wire diameters. Smaller $\bar{\Lambda}$ means greater roughness.

Figure 4.3 shows $\bar{\Lambda}$ as a function of Δ and ξ for exponential and Gaussian correlation on 70-nm-wide SiNWs. Note that the $\bar{\Lambda}(\Delta, \xi)$ surfaces look qualitatively similar to $\kappa(\Delta, \xi)$ (Fig. 4.1);

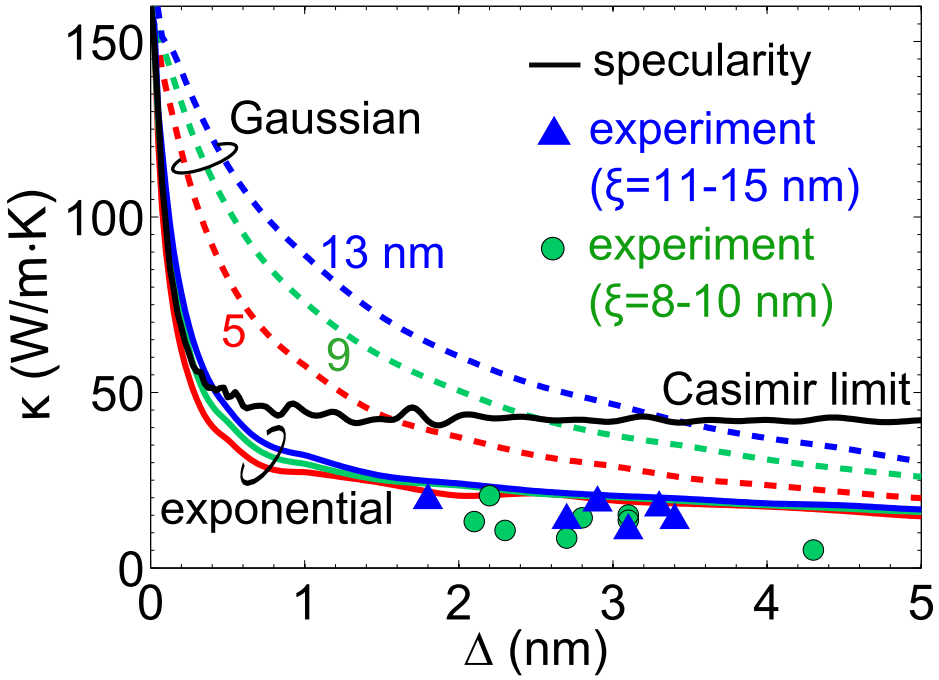

Figure 4.2: Thermal conductivity κ versus rms roughness Δ for 70-nm-wide SiNWs with different correlation lengths ξ and autocorrelation functions of the surface roughness. Values from the PMC calculation with real-space exponential (solid curves) and Gaussian (dashed curves) surfaces are presented for the correlation lengths of 5 nm (red), 9 nm (green), and 13 nm (blue). Thermal conductivity calculated by PMC with a momentum-dependent specularity-parameter model for phonon surface-roughness scattering (black solid curve) tends to the Casimir limit. The symbols represent experimental values from the supplement to Lim *et al.* [9], obtained on intentionally roughened SiNWs of diameters 67-84 nm, and with correlation lengths 8-10 nm (green circles) and 11-15 nm (blue triangles) extracted from exponential fits to experimentally obtained ACFs.

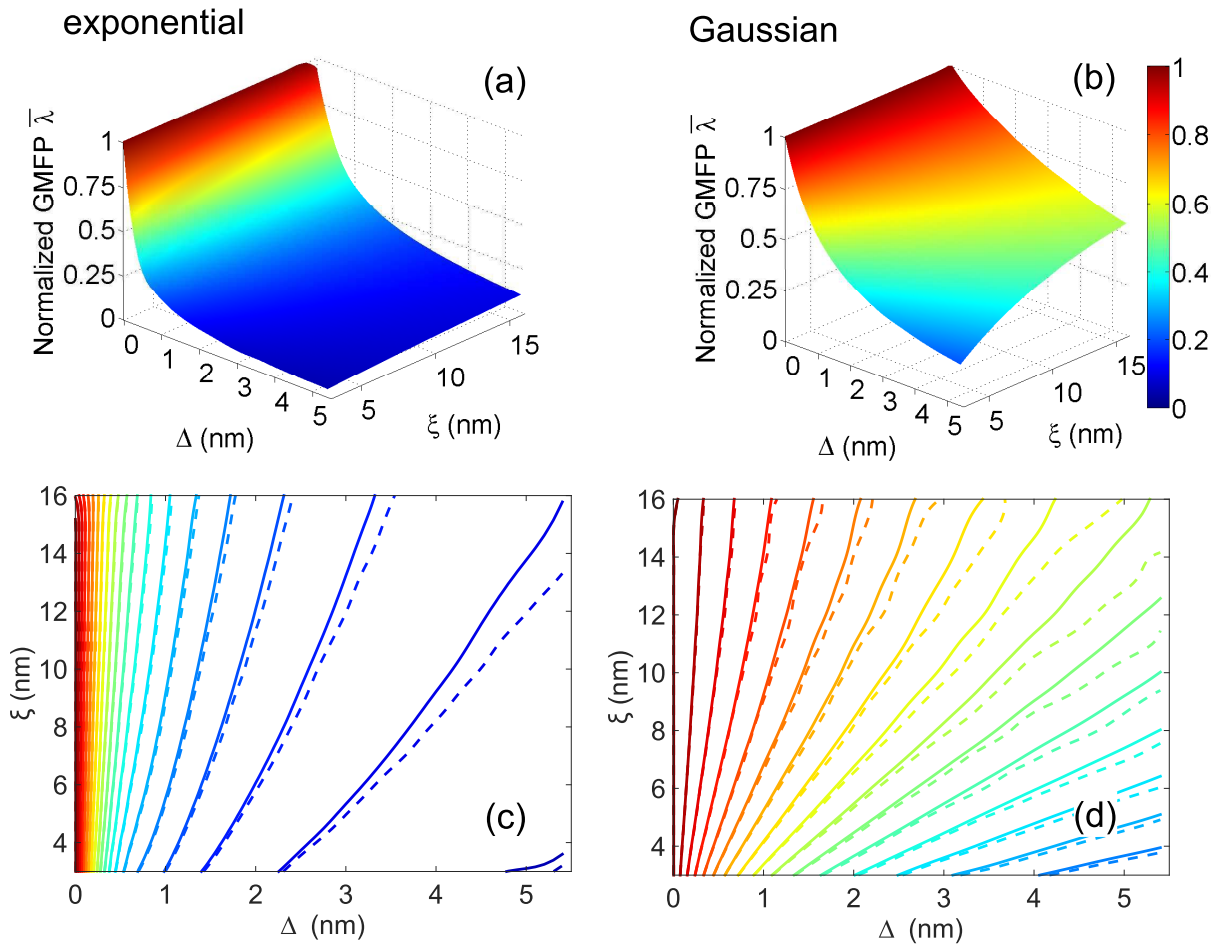

Figure 4.3: (Top row) $\bar{\Lambda}$, the geometric mean free path normalized to the SiNW width, as a function of rms roughness Δ and correlation length ξ for a 70-nm-wide SiNW whose rough boundary surfaces are characterized by (a) exponential and (b) Gaussian autocorrelation functions. (Bottom row) Contour plots of the normalized geometric mean free path $\bar{\Lambda}$ versus Δ and ξ for exponential (c) and Gaussian (d) boundary surfaces. Here, solid lines correspond to SiNWs of width 70 nm, while dashed lines represent 35-nm-wide SiNWs. Consecutively colored contours correspond to 0.05 increments in $\bar{\Lambda}$. The color scale is the same as in the top row.

both κ and $\overline{\Lambda}$ decrease as Δ increases and increase as ξ increases. The bottom two panels in Fig. 4.3 reveal an important universality: the contour plots of $\bar{\Lambda}(\Delta, \xi)$ for 35 and 70-nm-wide SiNWs are nearly identical for a given ACF. Therefore, once we specify the type of correlation, the normalized geometric mean free path $\bar{\Lambda}$ can be considered as a near-universal quantifier of surface roughness scattering, encompassing W, Δ, and ξ. From this point on, we will concentrate on exponential surfaces, as they resemble experiment more closely [9].

Figure 4.4(a) shows κ as a function of $\overline{\Lambda}$ for SiNWs of width 20, 35, and 70 nm and with exponential surfaces. Each plot presents thermal conductivity data for several hundred different SiNWs with real-space roughness. There are a number of interesting features in this graph. First, as $\bar{\Lambda} \to 1$ (the smooth-surface limit), all three curves converge to the bulk thermal conductivity [7], as expected. This smooth-wire limit is well captured by treating each surface with an appropriate specularity parameter, as seen in Fig. 4.2. Second, the Casimir limit values (17.3, 26.1, and 42.7 $\mathrm{W/m \cdot K}$ for the 20, 35, and 70-nm SiNWs, respectively) occur at $\bar{\Lambda} \approx 1/2$, i.e., $\Lambda = W/2$. Therefore, thermal conductivity below the Casimir limit corresponds to $\bar{\Lambda} < 1/2$.

In the inset to Fig. 4.4(a) we present thermal conductivity normalized to width, κ/W, versus $\bar{\Lambda}$ when internal scattering mechanisms have be turned off and only surface-roughness scattering remains. For $\bar{\Lambda} > 1/2$, i.e., above the Casimir limit, the curves for the three different SiNW widths coincide: roughness-limited thermal conductivity per unit width is universal as a function of $\bar{\Lambda}$ in this regime. With increasing roughening, however, once the Casimir limit has been surpassed ($\bar{\Lambda} < 1/2$), the curves start to diverge from one another. Therefore, there is a fundamental difference in surface-limited transport above and below the Casimir limit, an important issue that we explore further below.

The most prominent feature of Fig. 4.4(a) is that, for each SiNW thickness, there is a crossover in $\kappa(\bar{\Lambda})$. In the low-to-moderate roughness regime, $\kappa(\bar{\Lambda})$ is exponential ($\ln \kappa \sim \bar{\Lambda}$, with a width-dependent slope), notably so for the thicker two SiNWs (35 and 70 nm). Since our phonons are semiclassical point particles, localization [165] stemming from coherent superposition of waves is out of the question. We believe the explanation is related to the phenomenon of variable-range hopping [166, 167], where there is an exponential dependence of conductivity of the characteristic

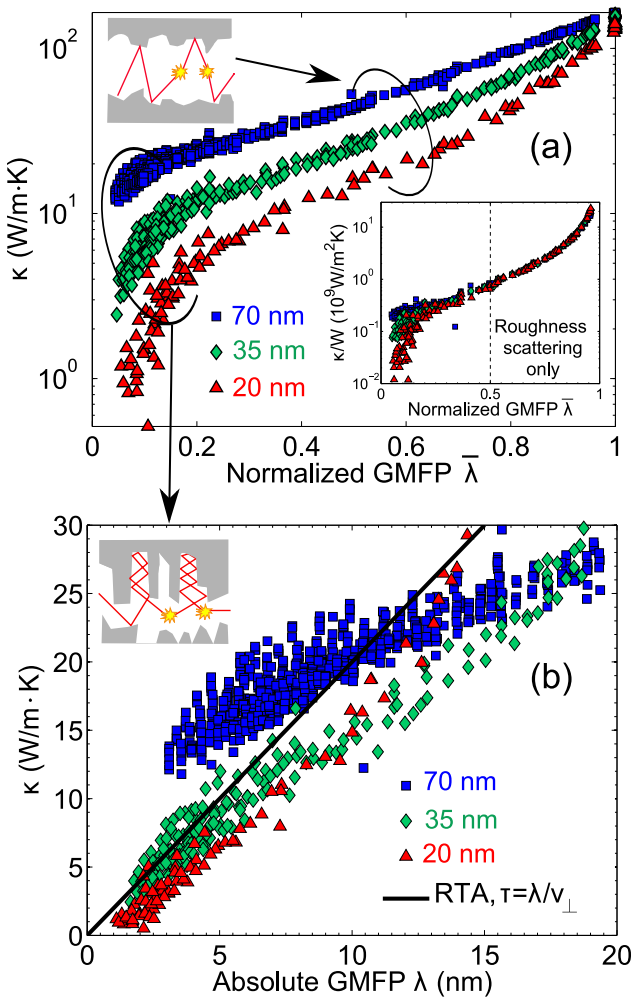

Figure 4.4: (a) Room-temperature thermal conductivity κ as a function the normalized geometric mean free path $\bar{\Lambda}$ for SiNWs of width 70 nm (blue squares), 35 nm (green diamonds), and 20 nm (red triangles), obtained from PMC simulation on a large ensemble of SiNWs with real-space exponentially correlated rough surfaces. (Inset) κ normalized to width W versus $\bar{\Lambda}$ without internal scattering for the same SiNWs as in the main panel. Vertical dashed line denotes $\bar{\Lambda} = 1/2$. (b) Thermal conductivity κ as a function of the absolute geometric mean free path Λ for very rough SiNWs [low-$\bar{\Lambda}$ region from (a)]. The solid black line corresponds to a simple RTA solution with $\tau = \Lambda/v_{\perp}$ that yields a thermal conductivity of $\kappa = A\Lambda$, $A \approx 2 \times 10^9\,\mathrm{W/m^2K}$. The schematics depict phonon trajectories, interrupted by internal scattering events, in SiNWs with (a) low-to-moderate and (b) pronounced roughness.

hopping range. What happens here, for low-to-moderate roughness, can be referred to as *variable-range bouncing*: phonon bounces between opposite sides of the SiNW, while the range variability stems from the path being interrupted by internal scattering events, as depicted in the top-left-corner schematic in Fig. 4.4(a).

Another interesting aspect of Fig. 4.4(a) is the $\kappa(\bar{\Lambda})$ behavior of very rough SiNWs (small $\bar{\Lambda}$). First off, the cross-over happens at smaller $\bar{\Lambda}$ for thicker SiNWs, because in thicker SiNWs the relative importance of internal scattering at a given $\bar{\Lambda}$ is higher. The small-$\bar{\Lambda}$ region is also harder to reach in thicker SiNWs, like the 70-nm one, because very high Δ would be required, outside of the range we focused on here. The $\kappa(\bar{\Lambda})$ behavior in the small-$\bar{\Lambda}$ region can be explained by *multiple scattering events at the same boundary*. In Fig. 4.4(b), we zoom in on the low-$\bar{\Lambda}$ region from Fig. 4.4(a) and present κ as a function of the absolute GMFP, Λ. We note that the thermal conductivities reach very low values, of only a few W/m·K, such as those measured by Hochbaum *et al*. [20]. We also see that the data for 20-nm and 35-nm SiNWs fall on top of each other, which is in keeping with the intuitive picture that multiple scattering events from the same boundary govern transport, so crossing the wire, and thus the wire width, becomes irrelevant. Indeed, the low-Λ region agrees very well with the relaxation-time approximation (Sec. 2.1.1) expression for the thermal conductivity [Eq. (2.11)] with a relaxation time of

$$\tau_{j,k} = \frac{\Lambda}{v_{\perp,j,k}}, \tag{4.2}$$

where $v_{\perp,j,k}$ is the velocity component perpendicular to the wire axis. After plugging this relaxation time into the expression for κ in the RTA [Eq. (2.11)] and integrating, we obtain $\kappa = A\Lambda$, where $A \approx 2 \times 10^9\,\mathrm{W/m^2K}$ at 300 K [Fig. 4.4(b)]. This Λ is single-surface dominated [see top-left-corner schematic in Fig. 4.4(b)] and bears essentially no dependence on the SiNW width.[1] We note that Sadhu and Sinha [50] argued that coherent transport and multiple correlated scattering

[1] It is interesting to compare the relaxation time in Eq. (4.2) to the relaxation time from Casimir's model [Eq.(2.32)]. The two have a similar form except with Λ replacing W.

events at a surface are key to low thermal conductivities. Here, we obtain ultralow thermal conductivities within a semiclassical (incoherent) transport model. While coherent transport is clearly not required, multiple scattering processes from a surface are.

4.1.4 Summary

Thermal conductivities far below the Casimir limit can be readily obtained for SiNWs within the Boltzmann transport formalism, provided that real-space rough surfaces with realistic ACFs are employed. We introduced the concept of the normalized geometric mean free path $\bar{\Lambda}$, which encompasses SiNW width, roughness rms height, and correlation length. Thermal conductivities below the Casimir limit correspond to $\bar{\Lambda} < 1/2$. $\kappa(\bar{\Lambda})$ reveals universal signatures of the interplay between boundary-roughness and internal scattering: a) in the low-roughness, high-$\bar{\Lambda}$ region, $\kappa(\bar{\Lambda})$ is exponential, owing to phonons bouncing across the SiNW and having trajectories randomly interrupted by internal scattering events; b) in the high-roughness, low-$\bar{\Lambda}$ region, multiple scattering events at a single interface govern transport, $\kappa \sim \bar{\Lambda}$, and extremely low values of κ, close to the amorphous limit, are obtained. This work shows that pronounced roughness results in a fundamental, qualitative change to thermal transport in nanostructures.

The utility of Λ hints at a possible connection with chaotic systems. While the SiNWs with our numerically generated surfaces are technically not truly chaotic cavities [58, 60, 168, 64], real SiNWs may be [9]. Our PMC simulations can only consider particle (ray) dynamics and ray chaos, but the results in this section suggest that long-wavelength phonons in SiNWs may also have wave-chaotic dynamics. We explore possible connections with wave chaos in Sec. 4.3.

4.2 Elastic Medium FDTD Simulation of Graphenelike Nanoribbons

The previous PMC work made me curious about wave aspects of phonon–surface scattering, and I eventually decided on elastic medium FDTD as a simple system to investigate. My original question had to do with specular scattering. When using real-space roughness in PMC, we assumed that phonons would scatter specularly from a smooth surface and be in the same branch before and

after scattering (Sec. 2.5). However, I learned that this assumption was wrong [169], and I wanted to know if the false assumption mattered.

That initial question led to a variety of investigations that I report on below. I start with the original question of surface scattering (Sec. 4.2.1), which led to an investigations of Rayleigh surface waves and their impact on thermal conductivity (Sec. 4.2.3). In turn, surface modes led to an investigation of all modes in the system (Sec. 4.2.2) and energy localization (Sec. 4.2.4). Our results gave us insight into Casimir's model (Sec. 4.2.3.2) and other phonon–surface scattering models (Sec. 4.2.5). Finally, we came across an interesting result about the absence of length effects in our system (Sec. 4.2.3.3).

Much of the background for this section was covered in Chapter 3, so we will frequently refer to material in Chapter 3.

4.2.1 Surface Scattering and Mode Conversion

The longitudinal and transverse phonon modes are independent of each other in an infinite medium. However, the two types of modes, and their corresponding scalar wave equations [Eq. (3.5)], are not independent at a surface. For example, the fixed BC for the elastic wave equation ($\mathbf{u} = 0$) combined with Eq. (3.4) requires $\nabla\phi = -\nabla \times \mathbf{\Psi}$. So, the fixed BC for the elastic wave equation is not equivalent to independently applying fixed boundary conditions ($\phi = 0$ and $\psi = 0$) to the two scalar wave equations. In short, the elastic wave equation allows for mode conversion at the surface, while the scalar wave equations do not allow for mode conversion if their boundary conditions are applied independently. Existing scalar wave models of phonon–surface scattering typically employ only a single scalar wave [103, 104, 105, 106, 107, 108, 112, 53], which precludes mode conversion.

Figure 4.5 illustrates mode conversion at the surface via a colorized energy-density profile for a simple example: a longitudinal wave packet incident upon a smooth, free surface at the top. The longitudinal wave is reflected into longitudinal and transverse waves; there is no conversion from bulk into Rayleigh waves at a smooth surface [86, 100, 170, 171, 91]. Wei *et al.* [138] obtained similar results based on a molecular-dynamics simulation of mode conversion between bulk modes

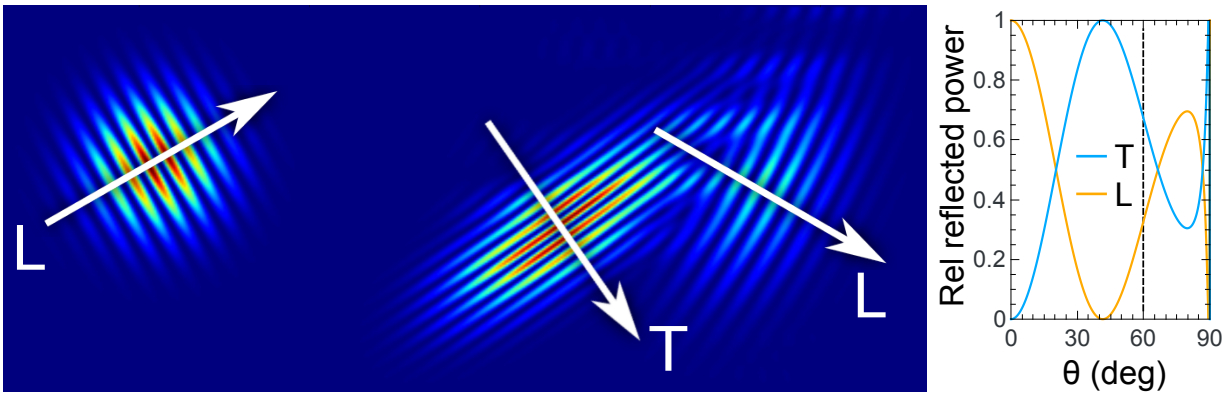

Figure 4.5: (Left panel) Visualization of elastic wave mode conversion at a smooth surface. Color represents the spatial profile of the energy density (arbitrary units; red–high, blue–low). A longitudinal wave packet is incident on a free, smooth top surface at 60° from the surface normal. One longitudinal and one transverse wave packet are reflected. The transverse wave can be identified by its shorter wavelength and slower group velocity. The plot to the right shows the relative energy in the scattered longitudinal (L) and transverse (T) wave packets as a function of the angle of incidence. The material parameters have a strong effect on the angular dependence seen in the plot.

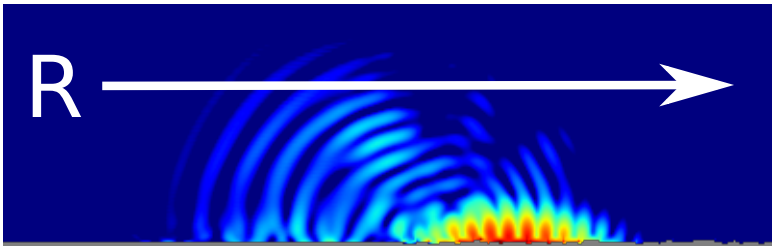

Figure 4.6: Snapshot of a Rayleigh wave that scattered from a rough surface. Color represents the energy-density profile (log scale, arbitrary units; red–high, blue–low). A Rayleigh wave packet was launched from left to right, moving first along a smooth bottom surface (left) and then along a rough bottom surface (right). Once the packet reaches the roughness (snapshot was taken shortly thereafter), it starts radiating energy into bulk modes. However, the conversion from Rayleigh into bulk modes is relatively weak. The energy leaves the packet slowly, and the packet continues to the right with little distortion.

at smooth graphene surfaces. There are many fine points of conversion between bulk modes, such as the angles where the incoming longitudinal wave is converted entirely into a reflected transverse wave (right panel in Fig. 4.5). However, in Sec. 4.2.3.1 we will show that mode conversion between bulk modes has little impact on phonon thermal transport in our nanoribbonlike systems and we therefore focus on conversion between bulk modes and Rayleigh waves at rough surfaces. (We note that conversion between bulk modes and Rayleigh waves has also been simulated with finite-element methods [172, 173, 174].)

Figure 4.6 shows a snapshot of the spatial energy density, represented by color, of a Rayleigh wave packet that moves from left to right along the bottom surface. The packet arrived from a region near a smooth surface (bottom left) and impinged upon a rougher region (bottom right); the snapshot was taken shortly thereafter. The packet remained largely intact, albeit slightly distorted, as it continued to travel along the rough surface. Some energy is radiated into bulk modes, but the amount is small compared to the amount of energy still in the packet (note that the energy density is plotted on a log scale). This finding is in line with previous studies of Rayleigh-wave

scattering from disordered surfaces, which showed that Rayleigh waves were tolerant of material density disorder on scales smaller than the wavelength [170, 171].

Figure 4.7 shows examples of mode conversion for an incident longitudinal wave packet scattering from surfaces with different roughness (nearly smooth: left column, very rough: right column) and boundary conditions (free BC: top row; fixed BC: bottom row). Each panel shows the spatial energy density, represented by color on a log scale. The incoming wave profile is the same as in Fig. 4.5, and is omitted here for clarity; the color represents only the energy density for the outgoing wave packets. First, the specularly scattered bulk modes are visible, albeit distorted, for the nearly smooth surfaces of both BCs. In contrast, scattering from the very rough surfaces of both BC is very diffuse. Second, no energy remains localized at the fixed surfaces, because fixed surfaces do not support surface modes. In contrast, a significant amount of energy is captured near the free surfaces. The longitudinal wave incident on the nearly smooth free surface is partially converted into Rayleigh waves. One Rayleigh-wave energy-density profile has been enlarged in the inset to the top left panel.

For the very rough free surface (Fig. 4.7, top right panel), the energy remaining near the surface is concentrated in a few places and has not propagated nearly as far along the surface as it did in case of its nearly smooth counterpart. The concentrated energy is similar to the spatially localized modes (SLMs) seen in molecular dynamics simulations [175, 39, 40]. In particular, the surface modes we see are similar to the "wag modes" predicted for atoms terminating bonds on nanowires [39, 40] and the motion of molecular chains ("side phonon leads") attached to the edges of nanoribbons [175]. Instead of a terminating atom, a protuberance of the nanoribbon wags back and forth. (See Fig. 4.9 and Sec. 4.2.2 for more detail.) SLMs were found to release their energy over relatively long time scales, and neighboring SLMs are often weakly coupled, so energy travels very slowly along the surface. Although the energy at the very rough free surface has effectively become localized and the wave is no longer a propagating one, for consistency, we will still refer to the localized surface modes as Rayleigh waves.

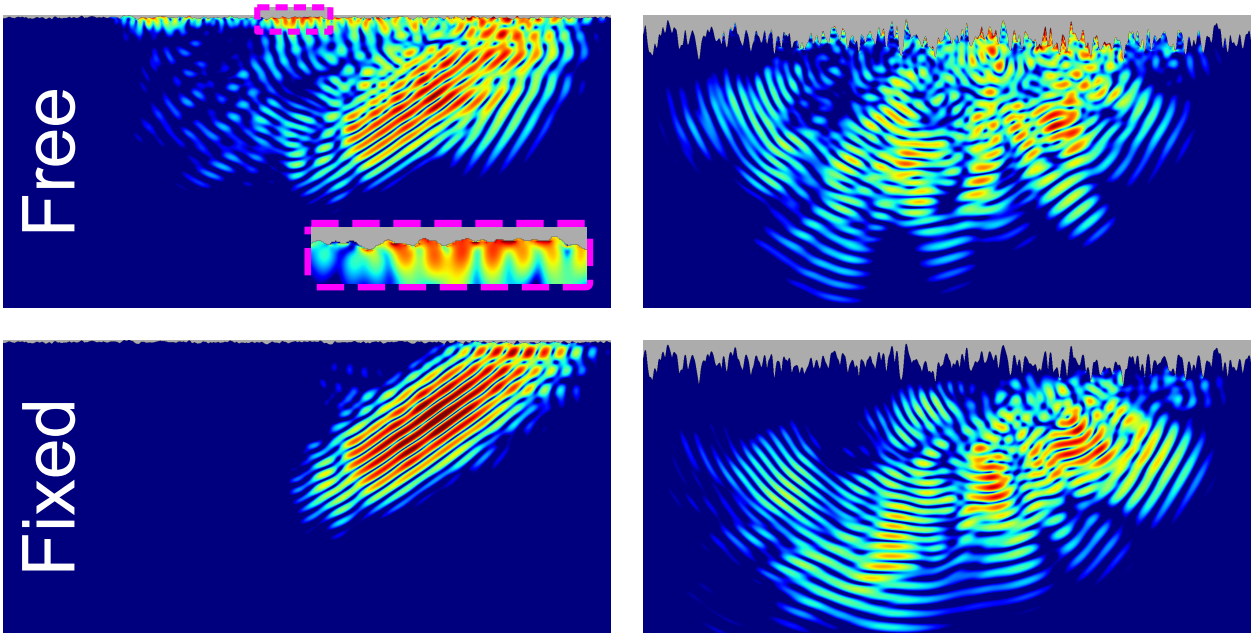

Figure 4.7: Snapshots of bulk elastic waves scattered from rough surfaces (top of each panel). Color represents the energy-density profile (log scale, arbitrary units; red–high, blue–low). A longitudinal wave packet was incident on a surface that is nearly smooth and free (top left panel), very rough and free (top right), nearly smooth and fixed (bottom left), and very rough and fixed (bottom right). Surface Rayleigh modes are visible only for the free surfaces (i.e., energy is localized near the free surfaces), because fixed surfaces do not support surface modes. (Inset to top left panel) Zoom-in on the energy-density profile for a free, nearly smooth surface (region inside the dashed box on the main panel) reveals a wave packet localized near the surface: a Rayleigh mode. (Compare with the Rayleigh wave packet in Figure 4.6. The relative size of the rms roughness Δ and packet wavelength λ are $\Delta/\lambda = 0.025$ for the left two figures, $\Delta/\lambda = 0.25$ for the right two figures. $\xi/\lambda = 0.5$ for all figures (ξ is the correlation length).

4.2.2 Localization and Vibrational Eigenmode Analysis

To directly investigate localization, we preform a vibrational eigenmode analysis (VEA) [96, 97, 98] of our system. VEA involves writing the equations of motion for the system [Eq. (3.10)] in matrix form and finding all the modes of the system (Sec. 3.2.3). VEA allows us to find the frequencies, spatial energy distribution, and motion of each mode. Because finding the eigenvectors and eigenvalues of a large matrix is computationally expensive, we only show results for ribbons 70 grid cells or less in width.

The localization of a mode is commonly quantified by its *participation ratio*, PR, [96, 97]:

$$PR = \left(N \sum_i E_i^2 \right)^{-1} \tag{4.3}$$

where N is the number of grid cells inside the ribbon, and E_i is the is the time averaged kinetic energy of the ith grid cell. E_i is calculated from the velocity-polarization vector $\mathbf{s}_v$ (Sec. 3.2.3) and is normalized so that $\sum_i E_i = 1$. The participation ratio is usually defined in terms of the displacement of the grid cells [96] rather than the velocity (and thus average kinetic energy). However, for a harmonic oscillator, the amplitudes of the displacement and velocity are proportional to each other, and any differences in constants are removed by the normalization. Our definition of the participation ratio is equivalent to the standard definition. We use our definition because our FDTD method yields the velocity but not the displacement.

PR measures how evenly the energy is spatially distributed in the system. If the energy is evenly distributed among the grid cells ($E_i = N^{-1}$), then $PR = 1$ (total delocalization, such as a plane wave). If all the energy is in one grid cell, then $PR = N^{-1}$ (total localization). Values between the two limits indicate varying degrees of localization.

Note that $PR = 1$ is impossible even inside a smooth ribbon because there must be standing waves in at least one direction. Standing waves have nodes where the displacement (and thus kinetic energy) is zero, so the kinetic energy cannot be evenly distributed. Consider scalar waves in a smooth ribbon of length L and width W, and take n, m to be natural numbers. A wave that is traveling along x and standing in y will be of the form $z\left(x, y, t\right) \sim \sin\left(\pi n y / W\right) e^{i(kx - \omega t)}$,

which results in $PR = 2/3$. A wave that is standing in both x and y directions will be of the form $z(x, y, t) \sim \sin(\pi n x/L) \sin(\pi n y/W) e^{i\omega t}$, which results in $PR = (2/3)^2 = 4/9$ [98]. Our structure has finite length but periodic boundary conditions, which means the modes are propagating but have longitudinal constraints stemming from periodicity as well as a finite grid cell size. Therefore, it is not surprising that the numerically obtained participation ratios for a smooth ribbon fall between $4/9$ and $2/3$.

The impact of boundary conditions on localization can be seen in Fig. 4.8. Free BCs results in significant localization at low frequencies, where we expect to find Rayleigh waves. As we noted in Sec. 3.1.2, low-frequency phonons are very common and important in actual 2D materials, so the localization of these phonons is particularly important. At higher frequencies, the participation ratios differ little between free and fixed BCs. While it is hard to definitively prove a connection between localization and conductivity, it is widely believed that localized modes contribute less to the conductivity than delocalized modes [176, 97, 177, 178].

We would like to stress that Fig. 4.8 shows that almost all low-frequency modes (including bulk modes) localize when free BCs are introduced. Consider the frequency range below 15 THz. This is where we expect all Rayleigh waves to lie for structures with free BCs (Sec. 3.2.1.2), although there are some small wag modes (described below) at higher frequencies. For fixed BCs (bottom panel) there are many modes below 15 THz, *and they are all bulk modes* since there are no Rayleigh waves with fixed BCs. These low-frequency bulk modes should not disappear when we introduce free boundary conditions, so it must be that there are many bulk modes below 15 THz for ribbons with free BCs. However, it is clear that, when free BCs are introduced, almost all the modes below 15 THz have become more localized – both the newly introduced Rayleigh waves and the preexisting bulk modes! The effect is striking. With fixed BCs, nearly all of these modes have participation ratios *above* $4/9$. With free BCs, the vast majority of the modes now have participation ratios *below* $4/9$. Recall participation ratios below $4/9$ are impossible for bulk modes in a smooth ribbon, so all participation ratios below the value $4/9$ are clear signs of localization due to disorder.

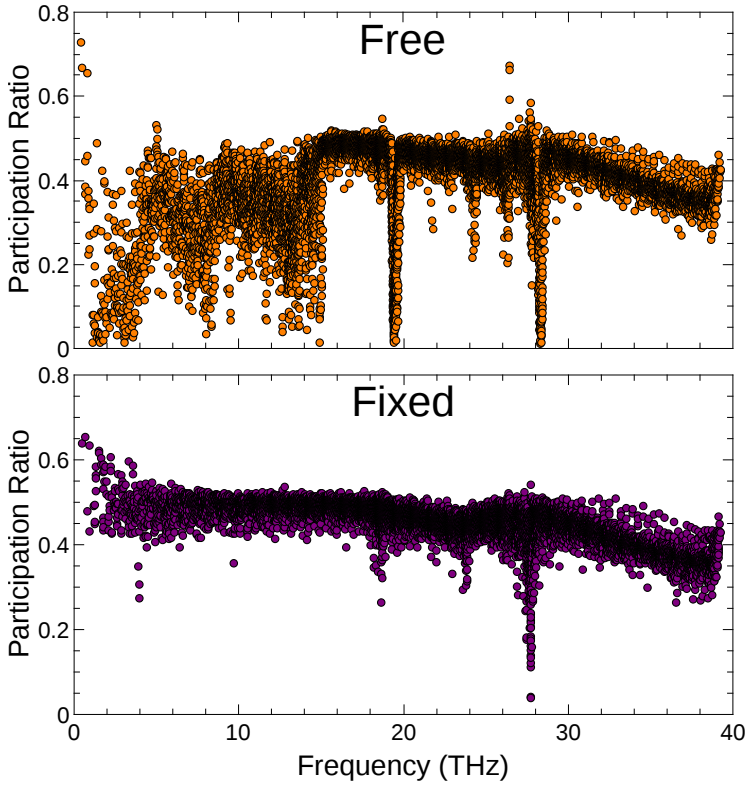

Figure 4.8: The participation ratio versus frequency for all modes of a $70h$-wide graphenelike nanoribbon with $\Delta = 2h, \xi = 5h$, and free (top) and fixed (bottom) BCs. Free BC results in significant localization at low frequencies, where we expect to find Rayleigh waves. Traveling waves in a smooth ribbon will have a participation ratio of $2/3$. Indeed, all the calculated participation ratios are below $2/3$ except for one spurious point. $4/9$ is the smallest participation ratio possible in a smooth ribbon. Almost all the low frequency modes in the fixed ribbon have participation ratios above $4/9$, while almost all the low-frequency modes in the free ribbon have participation ratios below $4/9$. This clearly shows how free surfaces can increase the localization of all low-frequency modes; nearly all surface Rayleigh modes are in this range.

Table 4.1: Average participation ratio, $\bar{p}$, for modes with frequencies below 15 THz (which includes all Rayleigh waves) in graphenelike nanoribbons of width and length 70h and correlation length $\xi = 5h$ at different rms roughness Δ. Grid-cell size is $h = 0.246$ nm.

$\Delta \rightarrow$	0	$3h$	$6h$	$9h$	$12h$
$\bar{p}_{\text{free}}$	0.515	0.352	0.323	0.286	0.267
$\bar{p}_{\text{fixed}}$	0.543	0.493	0.483	0.474	0.465
$\frac{\bar{p}_{\text{free}}}{\bar{p}_{\text{fixed}}}$	0.948	0.714	0.668	0.602	0.573

The large drop in participation ratio for free surfaces is due to surface roughness and is not an intrinsic effect of free BCs. Table 4.1 shows the average participation ratios for modes with frequencies below 15 THz as roughness is increased. For smooth ribbons, the average participation ratio is nearly the same for free and fixed BCs, so free BCs do not intrinsically lower the participation ratio. However, as the roughness is increased, the differences in the participation ratios become clear. The participation ratio for fixed ribbons drops slowly as roughness is increased, but the participation ratio for free ribbons drops precipitously. It is possible that this effect is related to mode conversion between Rayleigh and bulk waves (Sec. 4.2.1). Rayleigh-to-bulk mode conversion also requires free surfaces and is also nonexistent at smooth surfaces but becomes more prominent with increased roughness. Rayleigh-to-bulk mode conversion might lead to hybridized bulk-Rayleigh waves and lead to increased localization of the formerly bulk modes. Note that the increased localization seen in Fig. 4.8 disappears immediately after the cutoff frequency for Rayleigh waves ≈ 13 THz (Sec. 3.2.1.2), which further suggests that Rayleigh waves play a directly role in increasing localization.

VEA also allows us to visualize individual modes. Figure 4.9 shows one of the wag modes described in Sec. 4.2.1, as well as a surface mode that is less localized. The less-localized surface mode looks like a series of wag modes interspersed with several gaps. These gaps suggest that the mode cannot propagate energy all the way through the structure. This could indicate that the structure is sufficiently rough to prevent Rayleigh waves from propagating. We have observed that

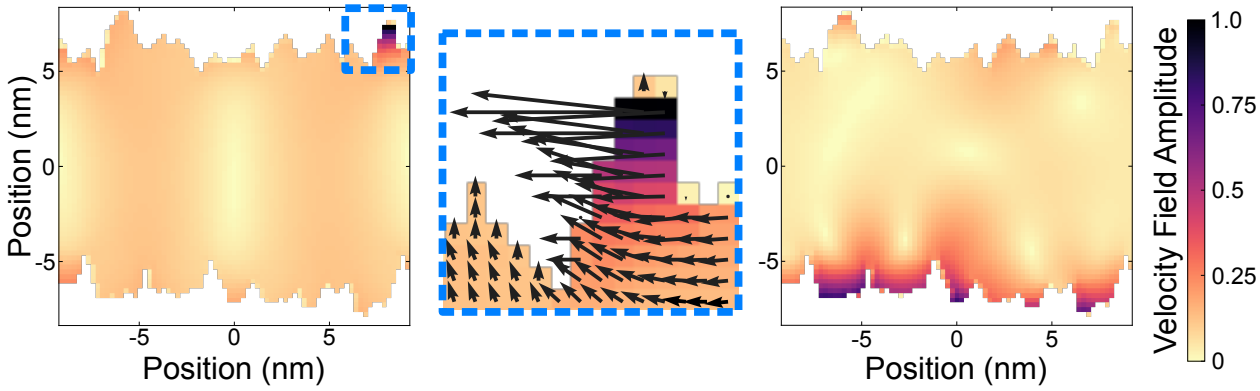

Figure 4.9: Illustration of surface modes calculated with VEA for a $50h$-wide ribbon with $\Delta = 3h$ and $\xi = 5h$. Color is the relative amplitude of the velocity field (proportional to the square root of kinetic energy) throughout the ribbon (colorbar to the right). (Left) A wag mode (participation ratio $p = 0.089$): the energy is concentrated in a protrubance that "wags" side to side, as illustrated by (center) a close-up of the wag mode with a superimposed snapshot of the velocity field. (Right) A mode that is less localized than the wag mode but still concentrates energy at the surface.

the most localized modes are generally surface modes. That observation is consistent with the energy-density distribution in the ribbon, which is discussed in Sec. 4.2.3.1 and Fig. 4.12. Fixed boundary conditions do not have a direct analog to wag modes because, unlike free boundary conditions, fixed boundaries generally allow bulk modes to extend into surface irregularities so that the protuberances do not have their own modes [98].

The dips in Fig. 4.8 that occur at approximately 20 and 30 THz represent "bouncing ball" modes that traverse the ribbon at 45 degree angles to the ribbon axis. Bouncing-ball modes are very short-wavelength modes that correspond the trajectory of point particles "bouncing" though the structure [59]. The frequencies of the dips correspond to the shortest possible wavelength for longitudinal and transverse waves traveling at 45 degree angles to the ribbon axis (Sec. 3.2.1.2). It is unclear why these bouncing ball modes are more localized than bouncing ball modes at other angles.

This means that the location of the dips (and some other interesting features in Fig. 4.8) are somewhat dependent on our choice of h. However, these features could also occur in atomic materials, where the lattice spacing is set by nature, not by theorists.

4.2.3 Thermal Conductivity and Rayleigh Waves

4.2.3.1 Results

We now turn to the thermal conductivity of nanoribbons. We model ribons that are 300 grid cells (73.8 nm) long and have an average width of 100 grid cells (24.6 nm). The length is sufficient to supress length effects (Sec. 4.2.3.3). The results, summarized in Table 4.2, are the averages from 100,000 simulations. For each ribbon, we solve the elastic wave equation and the two decoupled scalar equations. The thermal conductivities given for the scalar waves are the sum of the thermal conductivities of the two decoupled scalar waves. The results follow the general pattern seen elsewhere [9, 23] of κ decreasing with increasing rms roughness Δ and decreasing correlation length ξ, with ξ having a weaker effect than Δ.

Because κ depends weakly on ξ, we simplify the analysis by focusing on Δ. Figure 4.10 shows κ as a function of Δ for $\xi = 9h$. Scalar waves (with both BCs) and elastic waves with fixed

Table 4.2: Calculated thermal conductivity (in $\mathrm{W/m \cdot K}$) of a 24.6-nm-wide graphenelike nanoribbon calculated based on the FDTD solution to the elastic and scalar wave equations with free and fixed boundary conditions. Roughness rms value Δ and correlation length ξ are measured in units of grid-cell size h (h =0.246 nm).

$\Delta \rightarrow$	1	2	3	4	5	1	2	3	4	5
$\xi \downarrow$	Elastic waves, free BCs					Scalar waves, free BCs				
3	1254	752	540	426	343	2916	1351	782	516	371
6	1409	757	563	426	340	3093	1361	794	560	393
9	1479	814	588	431	353	3210	1455	820	567	414
12	1620	834	580	455	362	3544	1499	882	582	427
15	1695	898	591	458	365	3727	1581	874	610	431
	Elastic waves, fixed BCs					Scalar waves, fixed BCs				
3	2309	1172	754	529	396	3457	1411	842	564	417
6	2697	1267	750	573	399	3530	1520	853	541	433
9	2934	1255	812	556	423	4289	1673	917	579	434
12	3272	1382	810	581	424	4063	1746	955	600	434
15	3287	1531	867	585	450	4535	1812	1020	645	460

surfaces have very similar results, which converge at large Δ. Elastic waves with free BCs have significantly lower thermal conductivities. By switching from fixed to free BCs, we turn on all the effects of Rayleigh waves: the slow Rayleigh waves themselves (Sec. 3.1.5), bulk-to-Rayleigh-wave conversion (Sec. 4.2.1), and their susceptibility to localization (Sec. 4.2.2). So, our thermal conductivity results show the combined effect of the existence of Rayleigh waves.

Although our method has significant limitations in modeling real materials, in order to test our simulation on larger structures, we also simulated 45-nm-wide nanoribbons with 0.6-nm rms roughness, similar to those measured by Bae *et al.* [179]. Our calculation, which only accounts for edge roughness, yielded $\kappa \approx 500\ \mathrm{W/m \cdot K}$; Bae *et al.* measured $\kappa \approx 80\ \mathrm{W/m \cdot K}$ at 300 K, considerably lower in part because of three-phonon scattering. Other simulation techniques have also predicted high thermal conductivities for rough graphene nanoribbons that are smaller than the approximately 25-nm-wide nanoribbons we consider here [94, 93, 92]. For example, Evans *et al.* [94] predicted a thermal conductivity of $\approx 3000 - 4000\ \mathrm{W/m \cdot K}$ for a 11-nm-wide graphene nanoribbon with one lattice constant of rms edge roughness.

4.2.3.2 Interpretation and Casimir's Model

It may seem surprising that the scalar and fixed elastic results are nearly identical, but the results are in line with one of Casimir's insights [17]: for bulk modes scattering from reflective surfaces (i.e., surfaces that do not "trap" energy), sufficient roughness scatters everything diffusely; the surface behaves like a blackbody that absorbs all incident phonons and immediately radiates them away at random angles. The details of the diffuse scattering (fixed or free surface, mode conversion or not) are irrelevant. All that matters is that the surface reflects everything diffusely. In this way, Casimir avoided the issue of mode conversion, even though he considered elastic waves. In Fig. 4.10, we see similar results. When the roughness is low, there are some differences between the scalar and fixed elastic results, but the results all converge as the roughness increases and the scattering becomes totally diffuse. (When there is no roughness, all the results also converge since there is no meaningful surface scattering.)

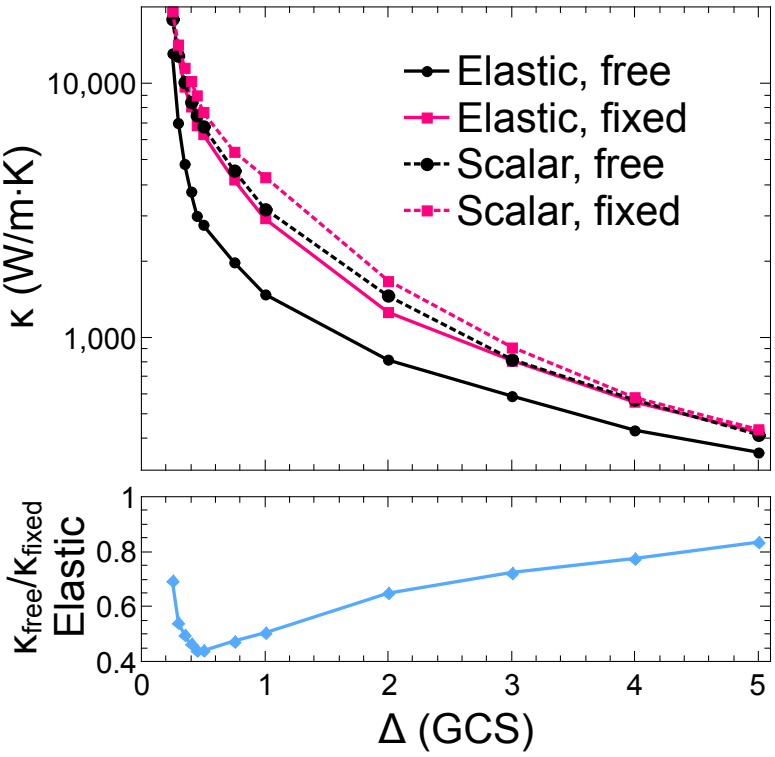

Figure 4.10: Top: Thermal conductivity κ of a nanoribbon as a function of rms roughness Δ (given in the units of h, the grid-cell size), as obtained based on the FDTD solution to elastic (solid lines) and scalar (dashed lines) wave equations with free (black circles) and fixed (red squares) boundary conditions. The correlation length ξ is fixed at $9h$ and the nanoribbon width is $100h$ (grid-cell size is h =0.246 nm). Bottom: Ratio of thermal conductivities resulting from free and fixed boundary conditions with the elastic wave equation. The thermal conductivities appear to converge in the limits of no surface disorder and very high surface disorder.

However, Casimir's insight only holds for reflective surfaces. In contrast, free surfaces support Rayleigh waves, which can effectively trap incident energy at the surface instead of reflecting it (Secs. 4.2.1,4.2.4). This limitation in Casimir's assumptions helps to explain why the free elastic results are different from the others, but not why they are are necessarily lower. At first glance, it might seem that Rayleigh waves should increase thermal conductivity; after all, Rayleigh waves are another mode to transport energy, and they also have the benefit of always traveling down the axis of the ribbon. However, Rayleigh waves have the disadvantage of being slower than either transverse or longitudinal waves, even when there is no disorder. More importantly, Rayleigh waves concentrate the energy where there is the most disorder, at the surface (Secs. 4.2.1,4.2.4), so the energy concentrated at the surface likely contributes little to thermal transport. Finally, free surfaces with rough boundaries increase the localization of all modes, including bulk modes, possibly through mode conversion with Rayleigh waves (Sec. 4.2.2).

Additionally, Casimir only considered planar surfaces, which puts a lower limit on the thermal conductivity in 3D systems. In 2D, Casimir's model predicts an infinite thermal conductivity in the absence of other scattering mechanisms [180]. The failure of Casimir's model in 2D raises the question of why our model predicts a finite thermal conductivity. Indeed, our model does not inherently have a finite thermal conductivity: the calculated thermal conductivity diverges if the boundaries are flat, so the rough boundaries (rather than finite length or discretization) are the cause of the finite thermal conductivities in our system. (Other systems where nonplanar boundaries produce finite thermal conductivity include some 2D billiard channels, Sec. 1.6.1.)

We believe that several factors are at play to explain the effects of free surfaces on elastic waves. If there is no roughness, there is no meaningful surface scattering, and all the results converge (left side of Fig. 4.10). Adding even a little roughness causes the results to diverge from one another, as the effects of localization and bulk-to-Rayleigh-wave mode conversion take hold. These effects remain important for medium roughness (middle of Fig. 4.10). At high roughness, other effects of roughness, such as constricting the ribbon width in places, are evidently more important than the BCs, and a large amount of roughness will cause the thermal conductivities of free and fixed ribbons to once again converge (right side of Fig. 4.10).

4.2.3.3 Absence of Length Effects

As noted earlier, we chose the length of the simulation domain to be large enough to suppress length effects(fig. 4.11). It may be surprising that length effects apparently disappear because it is commonly believed that, without anharmonicity, the thermal conductivity must be ill defined or diverge as the length of the structure is increased. For example, in 1D harmonic lattices (and may 1D lattices with anharmonicity), the thermal conductivity increases with system length L as a power law: $\kappa \propto L^{\alpha}$, where $\alpha > 0$ is system dependent [181, 182]. In this case, it is said that the thermal conductivity is not "finite" since it diverges with the system length. We do not see this power-law divergence. It could be that length effects would be visible in our system for larger L, but a nonfinite thermal conductivity is associated with a heat-current autocorrelation function that has a power-law decay [183]. We do not see a power-law decay in the thermal conductivity either (Fig. 3.5).

First, we note that although nonfinite thermal conductivities in 1D lattices have been thoroughly studied, much less is known about 2D lattices [182]. There have been reports of finite thermal conductivities in disordered, harmonic 2D lattices [184], although those results have been called into question [185, 186, 182]. More importantly, our system is not simply a lattice of harmonic oscillators that are solved with high-precession integration. Our system is an approximation of the elastic wave equation in a system that is infinite in one dimension solved using the FDTD method on a finite system with periodic boundary conditions in the infinite-size direction. (FDTD studies on systems that are similar to ours have shown localization [187] that results in an "absence of transport" [188].) The elastic wave equation also allows for wave chaos. We see signatures of wave chaos in our structures by looking at the nearest-neighbor level spacings and inverse participation ratio distributions [62]; this chaotic behavior may be related to the thermal conductivity and we will discuss in a future publication [189].

4.2.4 Energy Localization

The effect of Rayleigh-wave localization due to disorder is visible in Fig. 4.12, which depicts the difference between the energy-density profiles across the ribbon for free BCs (Rayleigh

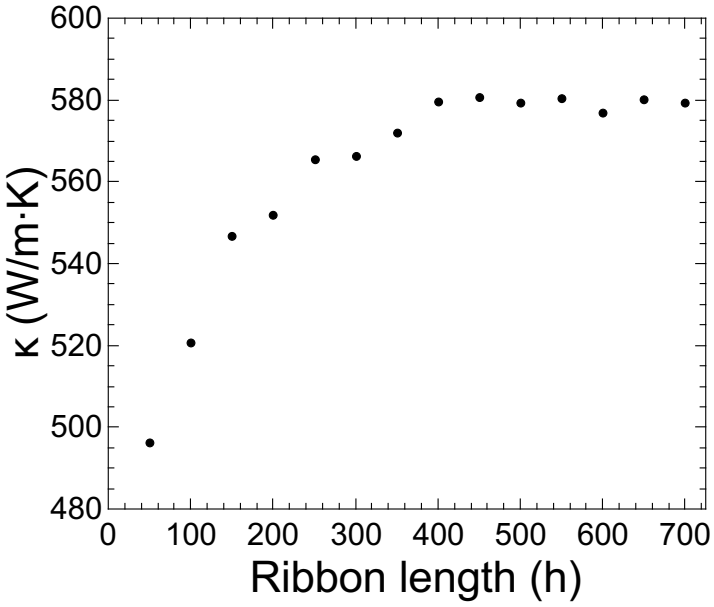

Figure 4.11: Thermal conductivity κ of a $100h$-wide ribbon (grid-cell size h =0.246 nm) versus ribbon length. The correlation length is $9h$, and the rms roughness is $3h$. There are length effects at small lengths, but the length effects are mostly gone by a length of $300h$. Most imporantly, κ does not appear to diverge like $\kappa \propto L^{\alpha}$, where L is the system length and α is a nonzero, system-dependent constant.

waves present) and fixed BCs (Rayleigh waves absent), normalized with the average energy density. Because we are performing an equilibrium simulation, the uneven energy distribution in the free ribbon shown in Fig. 4.12 implies energy localization for the same reason that uneven energy distribution in a single mode implies localization. Each curve is obtained by averaging over the length; the noise in the energy density near the edges is simply because there are fewer points to average over near the edges. Distance from the axis is in the units of nanoribbon width, so the average width goes from -1/2 to 1/2. Stars denote the minimal and squares the maximal distance between an edge and ribbon axis; in other words, the star-to-star distance denotes the minimum width (we can consider this the bulk region), while the square-to-square distance is the maximal ribbon width.

As the edge roughness increases on free ribbons, the energy density in the center of the ribbon decreases, and the energy density near the edges increases. However, increasing roughness on fixed ribbons has little impact on the energy-density profile. This is surely caused by localized modes that are associated with free BCs (Sec. 4.2.2). The increased roughness combined with free BCs must be creating more edge modes (or hybridize bulk and edge modes) with the effect that energy from the center of the ribbon is shifted to the edges. The edges are the most disordered part of the system, so energy stored at the edges likely contributes little to transport. This could be one way that increasing the roughness causes lower thermal conductivity.

4.2.5 Implications for Single-Scalar-Wave Models and Phonon Monte Carlo

Our results have implications for methods and models used to simplify phonon–surface scattering. Simplified phonon–surface scattering models are particularly important for many modern nanostructures, which are often too large to simulate with first-principles methods [12].

Many phonon–surface scattering models use the phenomenological concept of a specularity-parameter [18, 19, 33, 2, 190, 91] (Sec. 2.5.1), the probability a wave will scatter specularity from a rough surface. Existing specularity parameter models are tied to the scalar wave model, which does not support mode conversion. Indeed, Ziman adapted the concept of a specularity parameter from electromagnetic waves, which do not undergo meaningful mode conversion [19]. Our results

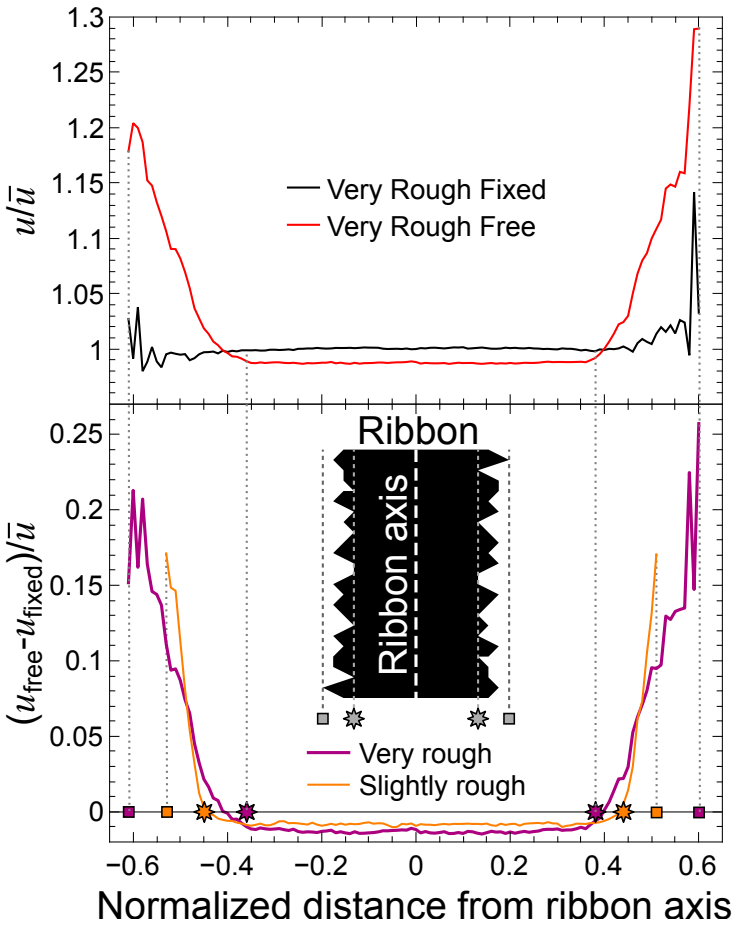

Figure 4.12: Spatial distributions of the energy density across the ribbon, normalized with respect to the average energy density $\bar{u}$. The position is given in the units of W, the ribbon width. Because of roughness, the distance of the edge from the nanoribbon axis varies; stars denote the minimal while squares denote the maximal distance of the edge from the axis; the star-to-star region can be considered the nanoribbon bulk. (Top) The energy densities for identical very rough ribbons ($\Delta/W = 0.05$, with $\xi/W = 0.09$) with free BCs (supporting Rayleigh waves) and fixed BCs (Rayleigh waves absent) versus position with respect to the ribbon axis. The free surface siphons energy while the fixed surface has little effect on the energy profile. (Bottom) Difference in the energy densities between free and fixed BCs for very rough (purple; $\Delta/W = 0.05$) and slightly rough (orange; $\Delta/W = 0.02$) ribbons; $\xi/W = 0.09$ for both. The free-minus-fixed energy-density profile (i.e., the difference between the curves from the top panel) represents the energy redistribution that stems from the presence of Rayleigh surface waves. It is notable that the energy gets moved away from the bulk and into the Rayleigh surface waves, an effect that becomes more pronounced with increasing roughness.

underscore the importance of the ongoing work to extend the specularity parameter model to account for mode conversion [191] and Rayleigh waves [91]. However, even with improvements, the specularity parameter concept only makes sense in the limit of weak roughness; all specularity parameter models have a "Casimir limit" when the specularity parameter is zero and all scattering is diffuse [23], yet in many three-dimensional nanostructures thermal conductivities far below that limit have been measured [20, 9, 156]. It is also not clear that an improved specularity parameter can result in finite thermal conductivity in two dimensional systems in the absence of other scattering mechanisms.

Another tool used to study phonon transport in relatively large nanostructures is phonon Monte Carlo (PMC), where a large ensemble of phonons are treated as point particles that drift and scatter [70, 4, 72, 73, 26, 23]. Current PMC simulations do not allow for mode conversion or Rayleigh waves. Instead, PMC simulations either have phonons scatter specularly at the surface [72, 26, 156, 23] or have a specularity parameter with the reflected phonon of the same mode as the incident phonon [73, 23]. Monte Carlo simulations for chaotic ray-splitting billiards are similar to PMC simulations, and the chaotic ray-splitting billiard simulations have been extended to allow for mode conversion between bulk modes [80]. The technique could be extended to PMC and, in principle, could support Rayleigh waves if the scattering amplitudes between bulk and Rayleigh waves were known.

Finally, let us consider what our results mean for the many phonon–surface scattering models based on scalar waves [103, 104, 105, 106, 107, 108, 109, 110, 111, 112, 113, 53]. While the scalar wave equation significantly overestimates κ, it does produce qualitatively similar results to the elastic wave equation: κ decreases with increasing Δ and with decreasing ξ. Problems arise when accurate predictions are needed for known surface roughness. This issue was seen in the work of Santamore and Cross, who studied a system first using scalar [104] and then elastic wave equations [48]. While both models could fit experimental data, they required significantly different surface-roughness parameters. (The actual surface roughness features were unknown.) For a surface with a known roughness profile, an elastic-wave model would be more accurate than a scalar-wave model.

4.2.6 FDTD Conclusion

In this section (which covers our work from [24]), we demonstrated the utility of the novel technique of calculating thermal conductivity by coupling a finite-difference-time-domain solution of the elastic wave equation with the Green-Kubo formula (Sec. 3.2). This technique can handle the large structures needed to investigate highly disordered surfaces. We apply this technique to 2D, but the method can easily be extended to 3D.

By including free surfaces, we see that not only do we introduce localized surface modes (such as propagating Rayleigh waves and nonpropagating wag modes), but low-frequency bulk modes also become significantly more localized (Sec. 4.2.2). This effect is not seen with fixed surfaces, which indicates that surface disorder alone does not cause the significant increase in localization. Instead, the increased localization is caused by a combination of surface disorder and boundary conditions, likely related to mode conversion between bulk and Rayleigh waves.

This increased localization is coincident with a buildup of energy at free surfaces but not at fixed surfaces (Sec. 4.2.4). This buildup reduces the energy density in the center of the ribbon. Since the edges are the most disordered part of the system, it stands to reason that the buildup of energy at the edges plays a role in reducing the thermal conductivity.

Indeed, we see that increased disorder does reduce the thermal conductivity, and this effect is more pronounced in ribbons with free boundary conditions than with fixed boundary conditions (Sec. 4.2.3.1), which underscores the importance of Rayleigh waves in reducing the thermal conductivity. The results for fixed and free ribbons appear to converge in the limit of large disorder. With enough disorder, it could be that other effects, such as significant constrictions of the ribbon, become more important than the effects of boundary conditions.

We qualitatively investigate mode conversion (Sec. 4.2.1) and find that mode conversion between bulk modes due to surfaces has little effect on thermal conductivity (Sec. 4.2.3.1), which can be explained with insights from Casimir's model (Sec. 4.2.3.2). In contrast, mode conversion between surface and bulk modes cannot be accounted for in Casimir's model.

Finally, we consider the limitations of common phonon–surface scattering models that do not include Rayleigh waves (Sec. 4.2.5), such as models that treat phonons as a single scalar wave.

While such models can qualitatively produce similar results to models based on elastic waves, a significant gap exists between the scalar wave and elastic wave predictions. Unlike single scalar waves, elastic waves are the long-wavelength limit of real phonons and should result in more accurate predictions.

We have shown that free surfaces (and the associated Rayleigh waves) play an important role in phonon–surface scattering and phonon localization, yet they are not included in most phonon–surface scattering models. However, both surface and internal scattering mechanisms (phonon–phonon, mass-difference, etc.) play important roles in nanoscale thermal transport. Additional work is needed to develop models that include internal scattering mechanisms, incorporate the effects of free surfaces, and are able to simulate large nanostructures.

4.3 Wave Chaos

Our success using the GMFP to understand transport in particle-based simulations lead us to wonder if similar methods could be applied to our discretized continuum structures. This possibility was particularly intriguing since, while elastic structures have long been studied as chaotic cavities, the transport properties of elastic structures have received much less attention [62]. Moreover, it is also interesting to look at the chaotic properties of our system because our system is discretized and thus may deviate from the predictions of wave chaos.

The first task was to determine if our nanoribbons were in fact chaotic cavities. This proved more difficult than expected, since there is an important, but subtle, distinction between "chaotic" and "disordered." Even after finding chaos in our system, we need to understand what is causing the chaos. Wave chaos is due to the chaotic ray dynamics of the cavity, but chaos can arise from other source and have different effects.

Part of the difficulty is that low-frequency modes in our model system do act like waves in a continuum (Sec. 3.2.1.2), so it should not be surprising that low-frequency modes can display wave chaos. Yet, the effects of discretization are clear in high-frequency modes, which do not behave like waves in a continuum. Discretization may also cause high-frequency modes not behave like

particles either because our system has a minimum wavelength.[2] So, it is not clear that high-frequency modes will display wave or ray chaos. In short, it could be that our structures appear chaotic for some frequency ranges, but not others.

4.3.1 Eigenvalue and Eigenvector Statistics

The most direct way to check for wave chaos in a system is to examine the statistics of the normal modes and their frequencies.[3] These are known as the eigenvector and eigenvalue statistics, respectively. In this section, we describe two measures that are useful to determine if a system is chaotic. To do this, we calculate the normal modes and their frequencies using the time-independent finite-difference method described in Sec. 3.2.3.

4.3.1.1 Nearest-Neighbor Level Spacing

The basic properties of nearest-neighbor level spacings are reviewed in Sec. 1.6.2, but the highlights are that a smooth ribbon will have a level-spacing distribution matching a Poisson distribution

$$p_{\mathrm{p}}(s) = e^{-s}, \tag{4.4}$$

while a chaotic ribbon will have a level-spacing distribution matching a GOE distribution

$$p_{\mathrm{GOE}}(s) = \frac{\pi}{2} s e^{-\pi s^2/4}, \tag{4.5}$$

where s is the frequency spacing between neighboring levels (normalized so that the average spacing is 1).

There are also systems that fall on a spectrum between chaotic and nonchaotic; their level-spacing distributions often look like a hybrid between Eqs. (4.4) and (4.5). Figure 4.13 shows the level-spacing distribution for ribbons with increasing roughness. As the roughness is increased,

[2]The FDTD dispersion relation [Eq. (3.11)] reaches its highest frequencies for $\mathbf{k}$ in the corners of the effective Brillouin zone [seen in Fig. 3.2(b3),(b4)]. So, the waves with the shortest wavelengths can only propagate diagonally and are not analogous to particles.

[3]There are other methods to check for chaos, such as computing the Lyapunov exponent from autocorrelation functions [192]. The Lyapunov exponent measures the exponential divergence described in Sec. 1.6.1.

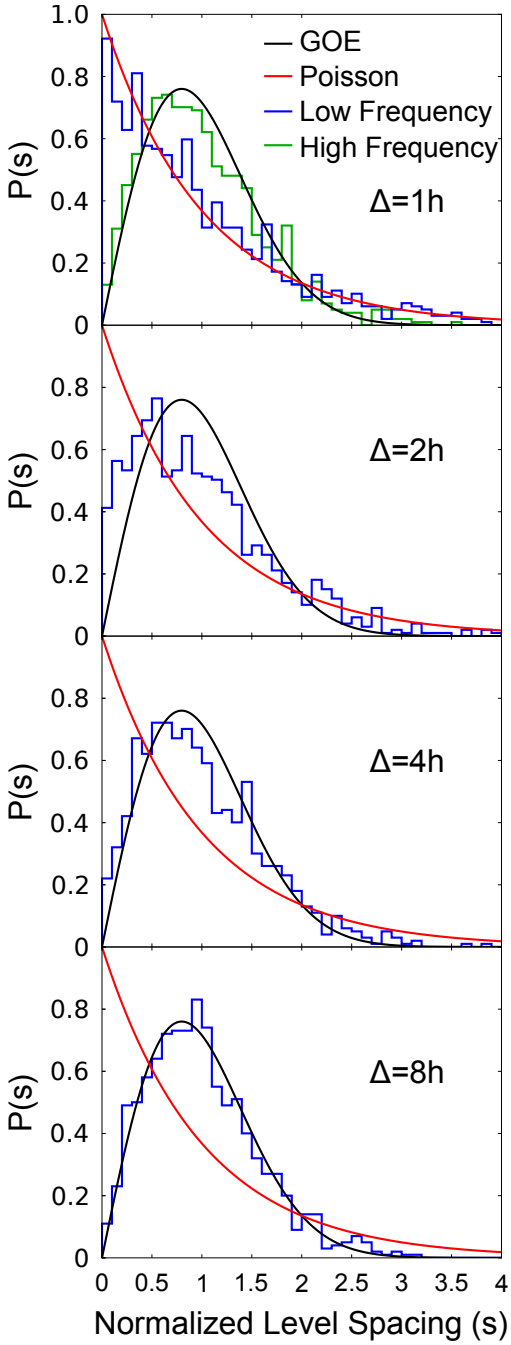

Figure 4.13: The nearest-neighbor level-spacing distribution for $100h$-wide-ribbons with a Gaussian edge and correlation length $15h$. The four plots are for RMS roughnesses Δ of $1h$, $2h$, $4h$, and $8h$ (from top to bottom). The blue curves are histograms calculated from 1000 modes with frequencies of around 6 THz. The crossover from a Poisson distribution (red) to a GOE distribution (black) is clear as the RMS roughness is increased. The green curve (top plot only) is for the 1000 highest-frequency modes in the system (about 38 THz). These modes follow a GOE distribution even at $\Delta = 1h$.

the distribution for 1000 modes around 6 THz transitions from a Poisson to a GOE distribution. In contrast, the 1000 highest frequency modes in the system (top panel only) follow a GOE distribution even for a relatively smooth ribbon. This is an example of how modes in different frequency ranges can be affected by roughness differently.

4.3.1.2 Inverse Participation Ratios

Results that show a GOE distribution are an important first step, but it is also possible to have a GOE distribution without having chaos. A GOE distribution can also arise from general disorder [10, 11] because many perturbations can lead to the level repulsion that is captured in the GOE distribution.

Another signature of wave chaos is seen in the distribution of inverse participation ratios. However, this requires a slightly different definition of (inverse) participation ratio than the one given in Sec. 4.2.2. For the purpose of studying the chaotic properties of a system, the inverse participation ratio (IPR) of a mode is

$$I = N\frac{\sum_i v_{i,x}^4}{\sum_i v_{i,x}^2}, \tag{4.6}$$

where N is the number of grid cells inside the ribbon, the sums run over all the grid cells, and $v_{i,x}$ is the x component of the velocity-polarization vector at the ith grid cell. (The velocity-polarization vector is denoted as $\mathbf{s}_v$ in Sec. 3.2.3.) The formula works just as well with the y component of the velocity-polarization vector. It is important not to use the magnitude of the velocity-polarization vector $|\mathbf{v}_i| = \sqrt{v_{i,x}^2 + v_{i,y}^2}$, because $|\mathbf{v}_i|$ will not have the same statistical properties as $v_{i,x}$ or $v_{i,y}$ alone. If $|\mathbf{v}_i|$ were used in place of $v_{i,x}$, then Eq. (4.6) would simply be the reciprocal of Eq. (4.3). With the proper definition in hand, we can now turn to studying the IPRs of our structures.

RMT predicts that all modes in a 2D chaotic system have $I = 3$ [10, 11]. In other words, the probability distribution function of the IPRs $p(I) = \delta(3)$. However, $p(I)$ will not be a delta function in a finite system but instead will be a relatively narrow distribution peaked around $I = 3$. In contrast, disordered systems have smeared-out distributions peaked at a value greater than 3 [10, 11].

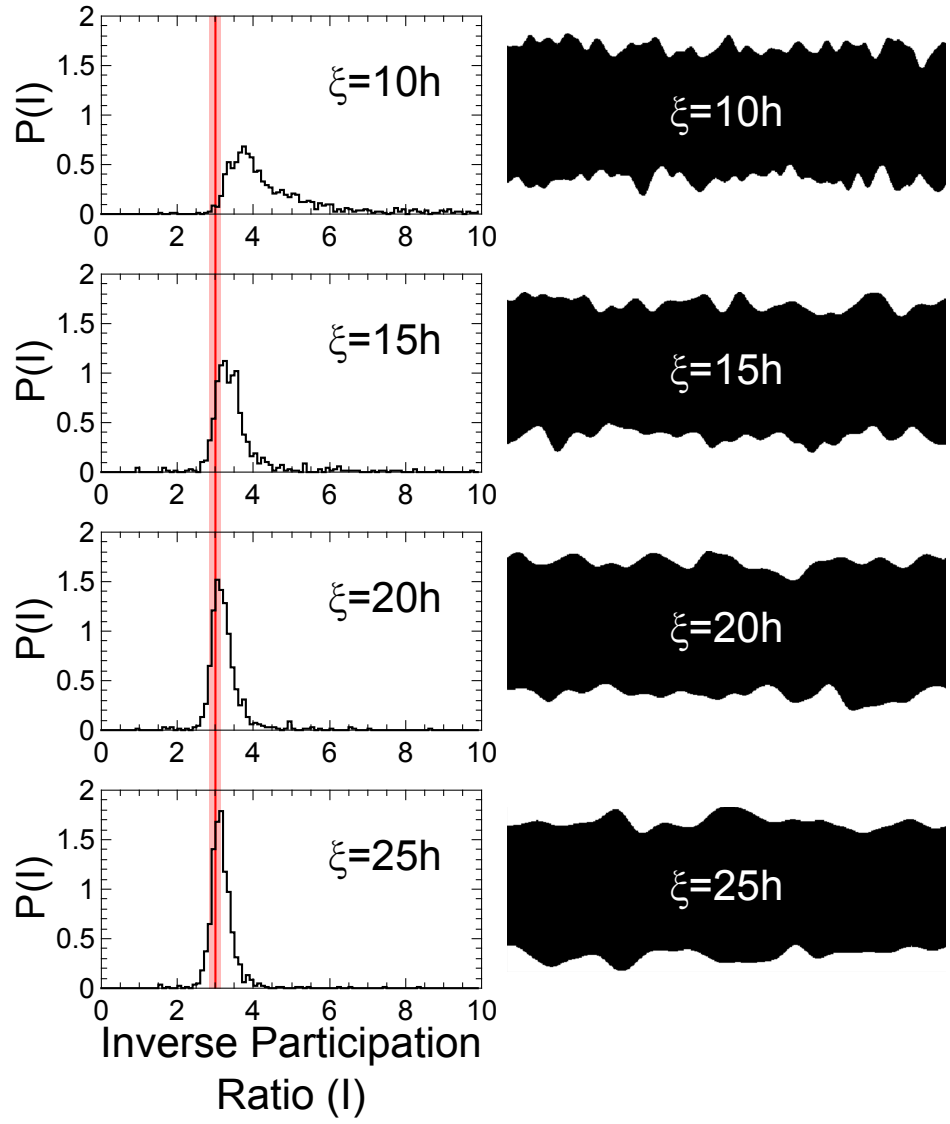

Figure 4.14: The inverse participation ratio distributions $p\left(I\right)$ (left) for $150h$-wide-ribbons with a Gaussian edge and RMS roughness $7.5h$ (right side, drawn in black). The four plots are for correlation length ξ of $10h$, $15h$, $20h$, and $25h$ (from top to bottom). Random matrix theory predicts that $p\left(I\right) = \delta\left(3\right)$, and chaotic systems should have $p\left(I\right)$ strongly peaked around 3 [10, 11]. The red line marks $I = 3$, and the red-shaded region covers $I = 3 \pm 0.15$. Increasing ξ reduces the short-scale roughness and causes a transition from a distribution expected for a disordered system (top) to a distribution expected for a chaotic system (bottom). The plotted $p\left(I\right)$ are calculated from histograms from 1000 modes with frequencies of about 2 THz.

Just as we can see a crossover in the level-spacing distribution as we vary the roughness (Fig. 4.13), we can likewise see a crossover in the IPR distribution. Figure 4.14 shows this transition as the correlation length ξ is varied. $\xi = 10$ results in a distribution associated with disordered systems while $\xi = 25$ results in a distribution associated with chaotic systems. Small ξ result in narrow "crevices" in the ribbons (right side of figure), and these crevices may suppress chaotic behavior since long wavelength modes may not be able to "fit" in narrower crevices. The modes used in Fig. 4.14 have frequencies of about 2 THz, which results in wavelengths of $29h$ and $43h$ for transverse and longitudinal waves, respectively. Long-wavelength modes are usually not affected by roughness on size scales much smaller than the wavelength [44]. Likewise, it may be that a structure does not appear chaotic if ξ is significantly smaller than the wavelength.

4.3.1.3 Automated Measures

While it is possible to estimate by eye whether a level-spacing distribution fits a GOE distribution, quantitative measures are needed to analyze larger data sets.

For the level-spacing distribution, I use a least-squares fit of the distribution to

$$p(s) = a\frac{\pi}{2}se^{-\pi s^2/4} + (1-a)\,e^{-x}, \tag{4.7}$$

where $a \in [0,1]$ is the fitting parameter. $a = 1$ corresponds to a perfect fit to the GOE distribution, and $a = 0$ corresponds to a perfect fit to the Poisson distribution. I chose $a > 0.85$ to be a good fit to the GOE distribution. It turns out that Eq. (4.7) is often a poor fit to distributions that fall between the GOE and Poisson distribution. However, Eq. (4.7) is not really meant to fit the data. Its fit parameter is simply meant to quantify how close a distribution is to a GOE distribution.

For the IPR distribution, I simply find the IPR value corresponding to the peak value of the distribution (i.e., the statistical mode). If this value falls in the range 3 ± 0.15, then I consider it to have an IPR distribution that is compatible with the system being chaotic.

The cutoffs in these two metrics are somewhat arbitrary, but both are reasonable.

Table 4.3: Level spacing and IPR distribution metrics for a variety of ribbon widths and correlation lengths ξ. The RMS roughness is set to 5% of the width. The level spacing and IPR distributions were calculated for modes with frequencies around 2 THz. Top: The fitting parameter a from Eq. (4.7). Values greater than 0.85 (shaded red) indicate a good fit to the GOE distribution. Bottom: The most common (mode) IPR value. Values within 3 ± 0.15 (shaded blue) are considered compatible with a system being chaotic. Each grid cell contains the average value from over 20 simulations, which is enough for the the results to converge. Width and correlation length ξ are measured in units of the grid-cell size h.

Width $\rightarrow$	100	150	200	250	300
$\xi \downarrow$	Fit parameter from Eq. (4.7)				
5	0.743	0.740	0.869	0.909	0.915
10	0.685	0.683	0.809	0.885	0.898
15	0.673	0.665	0.798	0.877	0.896
20	0.661	0.659	0.787	0.865	0.899
25	0.652	0.652	0.776	0.858	0.890
30	0.630	0.650	0.779	0.863	0.878
	Most common IPR value				
5	7.77	6.76	6.37	6.40	5.94
10	3.73	3.67	3.71	3.82	3.81
15	3.14	3.23	3.26	3.29	3.30
20	2.99	3.12	3.14	3.14	3.15
25	3.05	3.08	3.09	3.08	3.09
30	3.01	3.05	3.06	3.05	3.05

Table 4.3 shows the IPR and level-spacing distribution metrics for a variety of ribbon widths and correlation lengths. For a system to be chaotic, it is necessary to have a level-spacing distribution that is close to a GOE distribution (shaded red in the top table) and to have an IPR distribution peaked around $I = 3$ (shaded blue in the bottom table). Many ribbons fail one or both of these metrics, and only 6 of the width/correlation length combinations shown are compatible with wave chaos. The ribbon widths and surface-roughness parameters investigated in Sec. 4.2 were clearly not compatible with wave chaos.

4.3.2 Thermal Conductivity and Geometric Mean Free Path

One of the disappointments in our initial investigation of discretized elastic materials (Sec. 4.2) was that we could not establish a link between the geometric mean free path Λ [Eq. (1.34)] and the thermal conductivity; we had hoped for a link between the two since we saw a link between the two in PMC simulations (Sec. 4.1.3). However, the search for chaotic features made us investigate a larger range of ribbon widths and surface-roughness parameters — including a range of ribbons that are chaotic.

We calculated κ and Λ for each of the grid cells in Table 4.3 and plotted κ vs Λ in Fig. 4.15(a). The plot breaks the data points intro four categories for level spacings fitting the GOE distribution (or not) and IPR distributions peaked around 3 (or not). While there is no clear connection between κ and Λ, it seems that some function of Λ sets a lower bound on κ.

Of the four categories, only the least chaotic (no GOE, IPR not peaked at 3) appears to fall on a curve, and the curve follows the lower bound on κ. This is a surprising result because one might expected that chaotic systems (GOE, IPR peaked at 3) would be most closely connected to the GMFP, which is a concept from ray chaos.

Figure 4.15(b) is the same as (a) except that the horizontal axis shows the normalized geometric mean free path $\bar{\Lambda} = \Lambda/W$. There is no clear relationship between $\bar{\Lambda}$ and κ, although the results are clustered by category. More work is needed. (Note that, for 2D ribbons, the maximum value of $\bar{\Lambda}$ is $\pi/2$ [Eq. (1.34)].)

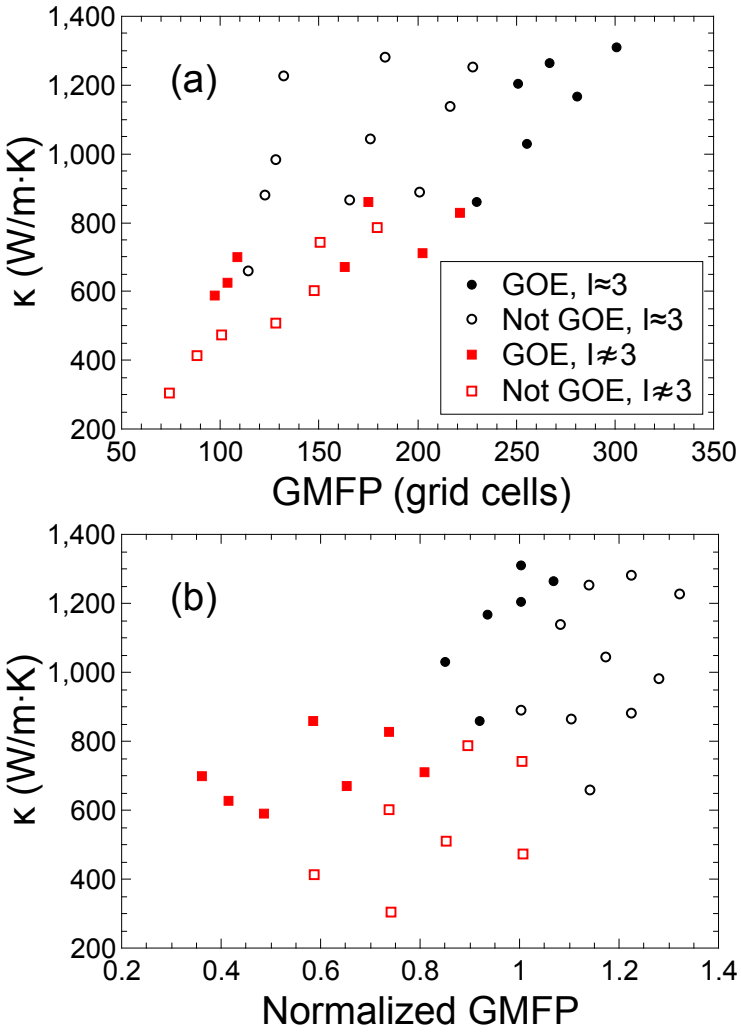

Figure 4.15: (a) Plot of thermal conductivity vs geometic mean free path for the ribbons in Table 4.3. The ribbons are broken down into the categories seen in the table: GOE level spacing/IPR peaked near 3 (filled black circles), no GOE level spacing/IPR peaked near 3 (open black circles), GOE level spacing/IPR not peaked at 3 (filled red squares), and no GOE level spacing/IPR not peaked at 3 (open red squares). Λ does seem to set a lower bound on κ. (b) same as above but with the normalized geometric mean free path $\bar{\Lambda}$ on the horizontal axis. There is no clear relation between κ and $\bar{\Lambda}$, but the results are clustered by category. Note that in a 2D nanoribbon, the maximum value of $\bar{\Lambda}$ is $\pi/2$ [Eq. (1.34)].

4.3.3 Frequency Dependence and Future Work

Another complication is that different frequency modes see the cavity differently. We already saw an example of frequency dependence in the top panel of Fig. 4.13, where the level spacing for high frequency modes followed a GOE distribution while lower frequency modes followed a Poisson distribution.

Figure 4.16 shows a similar frequency dependence in more detail. The inverse participation ratio and level-spacing distributions are calculated for several different frequencies in the same ribbon. It is clear that the 1, 5, and 10 THz modes do not see the cavity as chaotic, while higher-frequency modes might.[4] Frequency-dependent chaos may make it difficult to find a link between thermal conductivity and chaos because our method for calculating the thermal conductivity (Sec. 3.2.2) uses all the modes in the system — both modes that see the cavity as chaotic and those that do not.

A possible solution is to find the frequency-dependent transmission through the cavity as in [129, 130, 131, 132]. Instead of periodic boundary conditions, there would be absorbing boundary conditions [193, 123] at each end of the ribbon, a wave packet would be fired into the ribbon, and the frequency-dependent transmission (and reflection) could be calculated by taking the Fourier transform of the velocities in grid cells immediately in front of the absorbing boundaries. The frequency-dependent transmission could be used with the Landauer formula (Sec. 1.4 and [47]) to calculate the conductance of the structure. Moreover, we could calculate the conductance only for modes in a given frequency range, which would allow us to better see the effects of chaos on the thermal conductivity. Many models of transport through chaotic cavities are based on calculating the frequency-dependent transmission [59], and these methods allow other test for chaos, such as ribbon-to-ribbon conductance fluctuations [194].[5]

[4] I also preformed the same calculations for modes at 30 and 35 THz; the results are very similar to the 25 THz results.

[5] The FDTD-Green-Kubo method that we introduced in Sec. 3.2.2 has simulation-to-simulation variation because each simulation is initialized with random velocities. So, it is difficult to differentiate real ribbon-to-ribbon conductance fluctuations from random variation caused by the initial conditions.

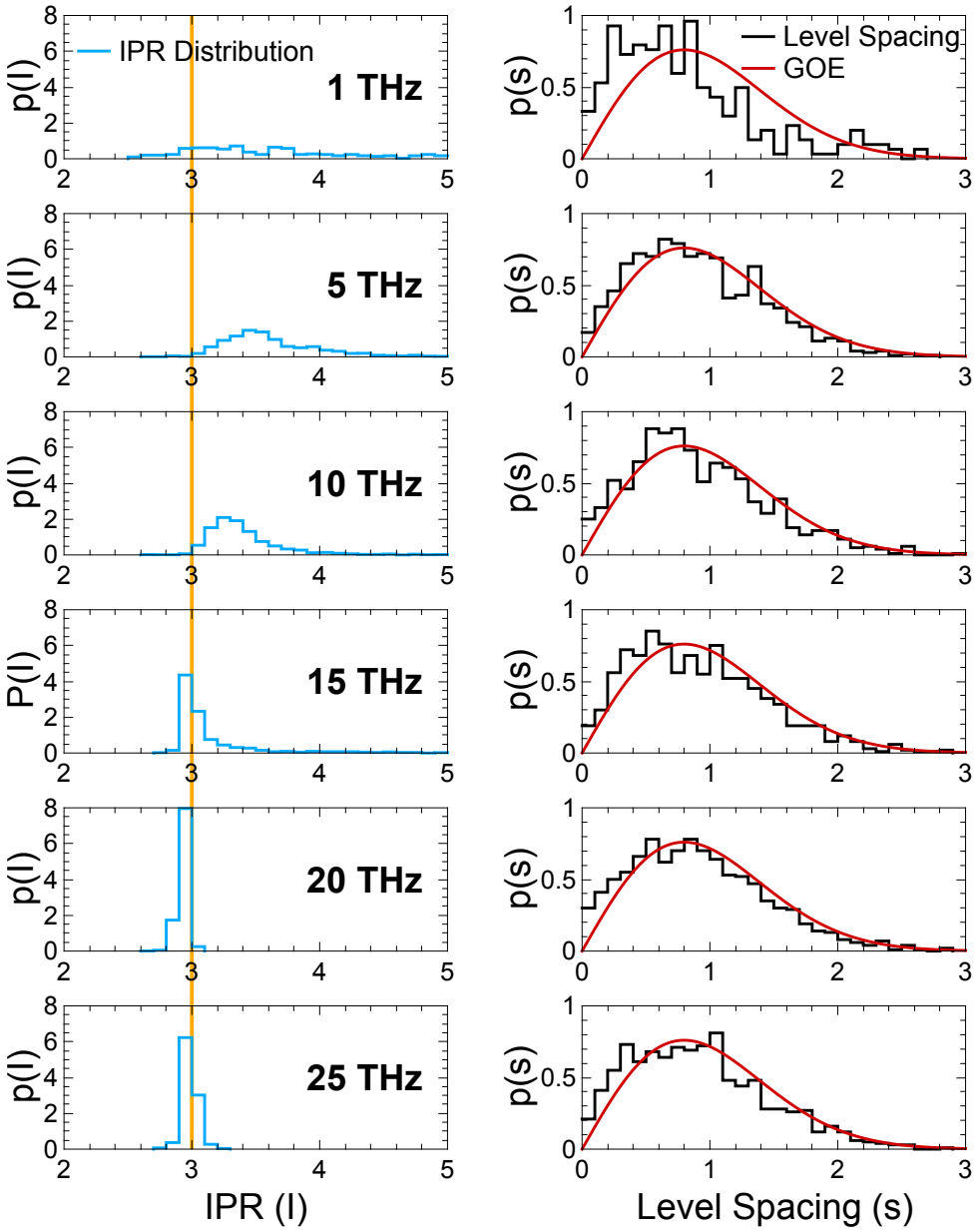

Figure 4.16: Inverse participation ratio distribution (left) and level-spacing distribution (right) of the same ribbon for different mode frequencies (from top to bottom: 1, 5, 10, 15, 20, and 25 THz). It is clear that any chaotic properties of the ribbon must be frequency-dependent; the ribbon cannot be chaotic for the 1, 5, and 10 THz modes, although the ribbon is still disordered at these frequencies. Each distribution was calculated from the 1000 modes with frequencies closest to the desired frequency. Calculated from a single 200h-wide ribbon with $\Delta = 10$, $\xi = 15$.

Chapter 5

Conclusion

In this dissertation, we examined the effects of surfaces on phonon dynamics through two very different approaches: a phonon Monte Carlo simulation based on semiclassical particles (Chapter 2) and elastic-medium finite-difference methods based on classical waves (Chapter 3). The two approaches nicely complement each other, and both illustrate the importance of rough surfaces on phonon transport.

Chapter 2 detailed many fine points of PMC simulations — such as random phonon generation (Sec. 2.4), energy conservation (Sec. 2.7), and contacts (Sec. 2.8) — including material that is important but rarely documented. The work in Chapter 2 is to be published in [25].

Chapter 3 demonstrated the utility of elastic-medium finite-difference methods; they are appropriate to model diverse systems from earthquakes to 2D nanostructures. The combination of FDTD with the Green-Kubo to calculate transport coefficients (Sec. 3.2.2) may prove particularly versatile. The method can be applied to a wide range of wave-transport problems. Finite difference methods also allow for the inclusion of nonbulk modes (such as Rayleigh waves) which can be important for phonon transport but are poorly understood. The work in Chapter 3 is published in [24].

The results from our PMC simulation (Sec. 4.1 and published in [23]) emphasize the importance of multiple scattering from surfaces and the interplay between surface and internal scattering mechanisms (Sec. 4.1 and [23]). The utility of the geometric mean free path is the highlight of our PMC results because the GMFP cleanly quantifies the effects of multiple scattering and the interplay between surface and internal scattering mechanisms (Sec. 4.1.3). For very short GMFPs,

the thermal conductivity is directly proportional to the GMFP. As the GMFP is reduced, the thermal conductivity shows a crossover from internal-scattering-dominated behavior (and fits within Casimir's model) to qualitatively different behavior that is dominated by phonon–surface scattering in a way that Casimir's model cannot account for. Our simulations can largely reproduce the very low thermal conductivities that are measured in experiment, which is a feat that few other models can match (Sec. 4.2).

Our elastic-medium finite-difference methods highlight how rough surfaces introduce surface modes (Sec. 4.2.1), increase the localization of all modes (Sec. 4.2.2), and trap energy (Sec. 4.2.4). The combination of these effects, together with straightforward phonon–surface scattering, reduces thermal conductivity (Sec. 4.2.3.1). We also see hints of chaotic behavior in our elastic structures (Sec. 4.2) that may prove useful for understanding transport in our systems. The work is to be published in [24].

Both of our simulation methods are well suited to model other large, experimentally relevant structures and thus have many potential applications. Moreover, both simulation methods can be adapted to other situations and extended to allow for new effects. The PMC code base has already been successfully adapted for use in graphene ribbons and extended to allow for full dispersion relations [8]; there is no shortage of other systems that the PMC code base could model. We have already experimented with introducing isotope scattering to our elastic-medium finite-difference simulations (by assigning different densities to different grid cells). Other possibilities include introducing phonon-phonon scattering (by making the material parameters strain-dependent [33]) or calculating the transmission through our system (as in [129, 130, 131, 132]) for use with the Landauer formula (Sec. 1.4 and [47]), which could be used to introduce Bose-Einstein statistics to our model.

However, an exciting opportunity for future work is further study of nanostructures as chaotic cavities for phonons. It is clear that the results in Sec. 4.3 barely scratch the surface of the chaotic properties of our system. Extending our elastic medium FDTD method to calculate transmission amplitudes would provide a direct connection with the many models of transport in chaotic systems

that are built on a scattering matrix formalism [59, 62]. This could allow the detection of other signatures of chaos, such as ribbon-to-ribbon conductance fluctuations [194].

Nanoscale thermal transport is still a developing field with many possible projects, from straightforward modeling of experimental devices to studying wave chaos, and I hope that the simulations and results described in this thesis prove useful for future projects.

Acronyms

ACF autocorrelation function. vii, 17, 18, 103

BC boundary conditions. 103

FDTD finite-difference time-domain. iv, 2, 67, 103

GCS Grid Cell Spacing. 103

GMFP geometric mean free path. 2, 20, 99, 103

HCACF heat-current autocorrelation function. x, 16, 73, 103

IPR inverse participation ratio. 100, 103

MD molecular dynamics. 103

MFP mean free path. 6, 103

PBTE phonon Boltzmann transport equation. 23, 27, 103

PMC phonon Monte Carlo. xiv, 2, 23, 27, 103

RMT random matrix theory. 21, 103

SiNW silicon nanowire. 1, 103

LIST OF REFERENCES

[1] J. Li, L. Porter, and S. Yip, "Atomistic modeling of finite-temperature properties of crystalline β-SiC: II. Thermal conductivity and effects of point defects," *J. Nucl. Mater.*, vol. 255, no. 2-3, pp. 139–152, 1998.

[2] S. B. Soffer, "Statistical Model for the Size Effect in Electrical Conduction," *J. Appl. Phys.*, vol. 38, no. 4, pp. 1710–1715, 1967.

[3] M. G. Holland, "Analysis of lattice thermal conductivity," *Phys. Rev.*, vol. 132, pp. 2461–2471, Dec 1963.

[4] D. Lacroix, K. Joulain, and D. Lemonnier, "Monte Carlo transient phonon transport in silicon and germanium at nanoscales," *Phys. Rev. B*, vol. 72, p. 064305, Aug 2005.

[5] A. Ward and D. A. Broido, "Intrinsic phonon relaxation times from first-principles studies of the thermal conductivities of Si and Ge," *Phys. Rev. B*, vol. 81, p. 085205, Feb 2010.

[6] D. T. Morelli, J. P. Heremans, and G. A. Slack, "Estimation of the isotope effect on the lattice thermal conductivity of group iv and group iii-v semiconductors," *Phys. Rev. B*, vol. 66, p. 195304, Nov 2002.

[7] C. J. Glassbrenner and G. A. Slack, "Thermal conductivity of silicon and germanium from 3k to the melting point," *Phys. Rev.*, vol. 134, pp. A1058–A1069, May 1964.

[8] S. Mei, L. N. Maurer, Z. Aksamija, and I. Knezevic, "Full-dispersion Monte Carlo simulation of phonon transport in micron-sized graphene nanoribbons," *J. Appl. Phys.*, vol. 116, no. 16, p. 164307, 2014.

[9] J. Lim, K. Hippalgaonkar, S. C. Andrews, A. Majumdar, and P. Yang, "Quantifying Surface Roughness Effects on Phonon Transport in Silicon Nanowires," *Nano Lett.*, vol. 12, no. 5, pp. 2475–2482, 2012.

[10] P. Pradhan and S. Sridhar, "Correlations due to localization in quantum eigenfunctions of disordered microwave cavities," *Phys. Rev. Lett.*, vol. 85, pp. 2360–2363, Sep 2000.

[11] P. Pradhan and S. Sridhar, "From chaos to disorder: Statistics of the eigenfunctions of microwave cavities," *Pramana*, vol. 58, no. 2, pp. 333–341, 2002.

[12] D. G. Cahill, P. V. Braun, G. Chen, D. R. Clarke, S. Fan, K. E. Goodson, P. Keblinski, W. P. King, G. D. Mahan, A. Majumdar, H. J. Maris, S. R. Phillpot, E. Pop, and L. Shi, "Nanoscale thermal transport. II. 2003–2012," *Applied Physics Reviews*, vol. 1, no. 1, p. 011305, 2014.

[13] R. Peierls, "Zur kinetischen Theorie der Wärmeleitung in Kristallen," *Annalen der Physik*, vol. 395, no. 8, pp. 1055–1101, 1929.

[14] R. Peierls, *On the Kinetic Theory of Thermal Conduction in Crystals*, ch. 4, pp. 15–48. Co-published by Imperial College Press and World Scientifc Publishing Co., 1997.

[15] I. Tamm, "Über die Quantentheorie der molekularen Lichtzerstreuung in festen Körpern," *Zeitschrift für Physik*, vol. 60, no. 5, pp. 345–363, 1930.

[16] A. B. Kojevnikov, "Paul Dirac and Igor Tamm correspondence; 1, 1928-1933," Tech. Rep. MPI-Ph-93-80, Max-Planck Inst., München, Oct 1993.

[17] H. Casimir, "Note on the conduction of heat in crystals," *Physica*, vol. 5, no. 6, pp. 495–500, 1938.

[18] R. Berman, F. E. Simon, and J. M. Ziman, "The Thermal Conductivity of Diamond at Low Temperatures," *Proc. R. Soc. A*, vol. 220, no. 1141, pp. 171–183, 1953.

[19] R. Berman, E. L. Foster, and J. M. Ziman, "Thermal Conduction in Artificial Sapphire Crystals at Low Temperatures. I. Nearly Perfect Crystals," *Proc. R. Soc. A*, vol. 231, no. 1184, pp. 130–144, 1955.

[20] A. I. Hochbaum, R. Chen, R. D. Delgado, W. Liang, E. C. Garnett, M. Najarian, A. Majumdar, and P. Yang, "Enhanced thermoelectric performance of rough silicon nanowires," *Nature*, vol. 451, pp. 163–167, 2008.

[21] W. Zhang, T. S. Fisher, and N. Mingo, "The atomistic Green's function method: An efficient simulation approach for nanoscale phonon transport," *Numerical Heat Transfer, Part B: Fundamentals*, vol. 51, no. 4, pp. 333–349, 2007.

[22] A. J. C. Ladd, B. Moran, and W. G. Hoover, "Lattice thermal conductivity: A comparison of molecular dynamics and anharmonic lattice dynamics," *Phys. Rev. B*, vol. 34, pp. 5058–5064, Oct 1986.

[23] L. N. Maurer, Z. Aksamija, E. B. Ramayya, A. H. Davoody, and I. Knezevic, "Universal features of phonon transport in nanowires with correlated surface roughness," *Appl. Phys. Lett.*, vol. 106, no. 13, p. 133108, 2015.

[24] L. N. Maurer, S. Mei, and I. Knezevic, "Rayleigh waves, surface disorder, and phonon localization in nanostructures," *Phys. Rev. B*, in press 2016.

[25] L. N. Maurer, S. Mei, and I. Knezevic, "Phonon Monte Carlo: Generating Random Variates for Thermal Transport Simulation," in *Nanophononics* (Z. Aksamija, ed.), Pan Stanford Publishing, 2016.

[26] E. B. Ramayya, L. N. Maurer, A. H. Davoody, and I. Knezevic, "Thermoelectric properties of ultrathin silicon nanowires," *Phys. Rev. B*, vol. 86, p. 115328, Sep 2012.

[27] A. H. Davoody, E. B. Ramayya, L. N. Maurer, and I. Knezevic, "Ultrathin GaN nanowires: Electronic, thermal, and thermoelectric properties," *Phys. Rev. B*, vol. 89, p. 115313, Mar 2014.

[28] K. Behnia, *Fundamentals of Thermoelectricity*. Cambridge University Press, 2015.

[29] N. W. Ashcroft and D. N. Mermin, *Solid State Physics*. Thomson Learning, 1976.

[30] Heremans Joseph P., Dresselhaus Mildred S., Bell Lon E., and Morelli Donald T., "When thermoelectrics reached the nanoscale," *Nat. Nano*, vol. 8, pp. 471–473, jul 2013.

[31] J. Lee, W. Lee, J. Lim, Y. Yu, Q. Kong, J. J. Urban, and P. Yang, "Thermal Transport in Silicon Nanowires at High Temperature up to 700 K," *Nano Lett.*, vol. 16, no. 7, pp. 4133–4140, 2016. PMID: 27243378.

[32] D. Li, Y. Wu, P. Kim, L. Shi, P. Yang, and A. Majumdar, "Thermal conductivity of individual silicon nanowires," *Appl. Phys. Lett.*, vol. 83, no. 14, pp. 2934–2936, 2003.

[33] J. M. Ziman, *Electrons and Phonons: the Theory of Transport Phenomena in Solids*. Clarendon Press, 1960.

[34] G. P. Srivastava, *The Physics of Phonons*. CRC Press, 1990.

[35] A. A. Maradudin, "Surface Acoustic Waves," in *Nonequilibrium Phonon Dynamics* (W. E. Bron, ed.), vol. 124 of *NATO ASI Series*, pp. 395–599, Springer US, 1985.

[36] A. K. Sood, J. Menéndez, M. Cardona, and K. Ploog, "Interface vibrational modes in gaas-alas superlattices," *Phys. Rev. Lett.*, vol. 54, pp. 2115–2118, May 1985.

[37] Y. Tanaka, F. Yoshida, and S. Tamura, "Imperfect phonon transmission and quantized thermal conductance in dielectric nanowires," *Phys. Status Solidi C*, vol. 1, no. 11, pp. 2625–2628, 2004.

[38] Y. Tanaka, F. Yoshida, and S. Tamura, "Lattice thermal conductance in nanowires at low temperatures: Breakdown and recovery of quantization," *Phys. Rev. B*, vol. 71, p. 205308, May 2005.

[39] B. Kang and S. K. Estreicher, "Thermal conductivity of Si nanowires: A first-principles analysis of the role of defects," *Phys. Rev. B*, vol. 89, p. 155409, Apr 2014.

[40] S. K. Estreicher, T. M. Gibbons, and M. B. Bebek, "Thermal phonons and defects in semiconductors: The physical reason why defects reduce heat flow, and how to control it," *J. Appl. Phys.*, vol. 117, no. 11, p. 112801, 2015.

[41] G. Chen, *Nanoscale Energy Transport and Conversion*. Oxford University Press, 2005.

[42] P. Carruthers, "Theory of thermal conductivity of solids at low temperatures," *Rev. Mod. Phys.*, vol. 33, pp. 92–138, Jan 1961.

[43] P. K. Schelling, S. R. Phillpot, and P. Keblinski, "Comparison of atomic-level simulation methods for computing thermal conductivity," *Phys. Rev. B*, vol. 65, p. 144306, Apr 2002.

[44] J. A. Ogilvy, *Theory of Wave Scattering from Random Rough Surfaces*. IOP Publishing, 1991.

[45] D. J. Griffiths, *Introduction to Electrodynamics*. Prentice Hall, 1981.

[46] D. K. Ferry and S. M. Goodnick, *Transport in Nanostructures*. Cambridge University Press, 1997.

[47] M. P. Blencowe, "Quantum energy flow in mesoscopic dielectric structures," *Phys. Rev. B*, vol. 59, pp. 4992–4998, Feb 1999.

[48] D. H. Santamore and M. C. Cross, "Effect of Phonon Scattering by Surface Roughness on the Universal Thermal Conductance," *Phys. Rev. Lett.*, vol. 87, p. 115502, Aug 2001.

[49] P. Martin, Z. Aksamija, E. Pop, and U. Ravaioli, "Impact of phonon-surface roughness scattering on thermal conductivity of thin Si nanowires," *Phys. Rev. Lett.*, vol. 102, p. 125503, Mar 2009.

[50] J. Sadhu and S. Sinha, "Room-temperature phonon boundary scattering below the Casimir limit," *Phys. Rev. B*, vol. 84, p. 115450, Sep 2011.

[51] J. Hyun Oh, M. Shin, and M.-G. Jang, "Phonon thermal conductivity in silicon nanowires: The effects of surface roughness at low temperatures," *J. Appl. Phys.*, vol. 111, no. 4, p. 044304, 2012.

[52] H. Jin Lee, J. Sik Jin, and B. Jae Lee, "Assessment of phonon boundary scattering from light scattering standpoint," *J. Appl. Phys.*, vol. 112, no. 6, p. 063513, 2012.

[53] G. B. Akguc and J. Gong, "Wave-scattering formalism for thermal conductance in thin wires with surface disorder," *Phys. Rev. B*, vol. 80, p. 195408, Nov 2009.

[54] S. M. Goodnick, D. K. Ferry, C. W. Wilmsen, Z. Liliental, D. Fathy, and O. L. Krivanek, "Surface roughness at the Si(100)-SiO2 interface," *Phys. Rev. B*, vol. 32, pp. 8171–8186, Dec 1985.

[55] Y. Zhao, H. Matsumoto, T. Sato, S. Koyama, M. Takenaka, and S. Takagi, "A novel characterization scheme of si/sio2 interface roughness for surface roughness scattering-limited mobilities of electrons and holes in unstrained- and strained-Si mosfets," *Electron Devices, IEEE Transactions on*, vol. 57, no. 9, pp. 2057–2066, 2010.

[56] M. G. Ghossoub, K. V. Valavala, M. Seong, B. Azeredo, K. Hsu, J. S. Sadhu, P. K. Singh, and S. Sinha, "Spectral Phonon Scattering from Sub-10 nm Surface Roughness Wavelengths in Metal-Assisted Chemically Etched Si Nanowires," *Nano Lett.*, vol. 13, no. 4, pp. 1564–1571, 2013.

[57] J. F. James, *A Student's Guide to Fourier Transforms*. Cambridge University Press, 2011.

[58] N. Chernov and R. Markarian, *Chaotic Billiards*. American Mathematical Society, 2006.

[59] H.-J. Stöckmann, *Quantum Chaos: an introduction*. Cambridge University Press, 2007.

[60] J. L. Vega, T. Uzer, and J. Ford, "Chaotic billiards with neutral boundaries," *Phys. Rev. E*, vol. 48, pp. 3414–3420, Nov 1993.

[61] N. Chernov, "Entropy, Lyapunov exponents, and mean free path for billiards," *J. Stat. Phys.*, vol. 88, no. 1, pp. 1–29, 1997.

[62] G. Tanner and N. Søndergaard, "Wave chaos in acoustics and elasticity," *J. Phys. A*, vol. 40, no. 50, pp. R443–R509, 2007.

[63] D. Alonso, R. Artuso, G. Casati, and I. Guarneri, "Heat Conductivity and Dynamical Instability," *Phys. Rev. Lett.*, vol. 82, pp. 1859–1862, Mar 1999.

[64] D. Alonso, A. Ruiz, and I. de Vega, "Polygonal billiards and transport: Diffusion and heat conduction," *Phys. Rev. E*, vol. 66, p. 066131, Dec 2002.

[65] B. Li, L. Wang, and B. Hu, "Finite Thermal Conductivity in 1D Models Having Zero Lyapunov Exponents," *Phys. Rev. Lett.*, vol. 88, p. 223901, May 2002.

[66] B. Li, G. Casati, and J. Wang, "Heat conductivity in linear mixing systems," *Phys. Rev. E*, vol. 67, p. 021204, Feb 2003.

[67] D. Alonso, A. Ruiz, and I. de Vega, "Transport in polygonal billiards," *Physica D*, vol. 187, no. 1-4, pp. 184–199, 2004. Microscopic Chaos and Transport in Many-Particle Systems.

[68] C. M. Marcus, A. J. Rimberg, R. M. Westervelt, P. F. Hopkins, and A. C. Gossard, "Conductance fluctuations and chaotic scattering in ballistic microstructures," *Phys. Rev. Lett.*, vol. 69, pp. 506–509, Jul 1992.

[69] O. Bohigas, M. J. Giannoni, and C. Schmit, "Characterization of chaotic quantum spectra and universality of level fluctuation laws," *Phys. Rev. Lett.*, vol. 52, pp. 1–4, Jan 1984.

[70] R. B. Peterson, "Direct Simulation of Phonon-Mediated Heat Transfer in a Debye Crystal," *J. Heat Transfer*, vol. 116, no. 4, pp. 815–822, 1994.

[71] S. Mazumder and A. Majumdar, "Monte Carlo study of phonon transport in solid thin films including dispersion and polarization," *J. Heat Transfer*, vol. 123, no. 4, pp. 749–759, 2001.

[72] J. Randrianalisoa and D. Baillis, "Monte Carlo Simulation of Steady-State Microscale Phonon Heat Transport," *J. Heat Transfer*, vol. 130, p. 072404, May 2008.

[73] A. Mittal and S. Mazumder, "Monte Carlo Study of Phonon Heat Conduction in Silicon Thin Films Including Contributions of Optical Phonons," *J. Heat Transfer*, vol. 132, no. 5, p. 052402, 2010.

[74] J.-P. M. Peraud, C. D. Landon, and N. G. Hadjiconstantinou, "Monte Carlo Methods for Solving the Boltzmann Transport Equation," *Annual Review of Heat Transfer*, vol. 16, pp. 205–265, 2004.

[75] M. F. Modest, *Radiative Heat Transfer*. Academic Press, 2003.

[76] L. Lindsay, D. A. Broido, and T. L. Reinecke, "*Ab initio* thermal transport in compound semiconductors," *Phys. Rev. B*, vol. 87, p. 165201, Apr 2013.

[77] D. Lacroix, K. Joulain, D. Terris, and D. Lemonnier, "Monte Carlo simulation of phonon confinement in silicon nanostructures: Application to the determination of the thermal conductivity of silicon nanowires," *Appl. Phys. Lett.*, vol. 89, no. 10, p. 103104, 2006.

[78] R. Piessens, E. de Doncker-Kapenga, C. Uberhuber, and D. Kahaner, *Quadpack: A Subroutine Package for Automatic Integration*. Springer, 1983.

[79] L. Devroye, *Non-Uniform Random Variate Generation*. Springer-Verlag, 1986.

[80] L. Couchman, E. Ott, and T. M. Antonsen, "Quantum chaos in systems with ray splitting," *Phys. Rev. A*, vol. 46, pp. 6193–6210, Nov 1992.

[81] M. Asheghi, K. Kurabayashi, R. Kasnavi, and K. E. Goodson, "Thermal conduction in doped single-crystal silicon films," *J. Appl. Phys.*, vol. 91, no. 8, pp. 5079–5088, 2002.

[82] J. Callaway, "Model for lattice thermal conductivity at low temperatures," *Phys. Rev.*, vol. 113, pp. 1046–1051, Feb 1959.

[83] P. G. Klemens, "Thermal Conductivity and Lattice Vibrational Modes," vol. 7, pp. 1–98, 1958.

[84] A. Cepellotti, G. Fugallo, L. Paulatto, M. Lazzeri, F. Mauri, and N. Marzari, "Phonon hydrodynamics in two-dimensional materials," *Nature Communications*, vol. 6, p. 6400, 2015.

[85] S. Lee, D. Broido, K. Esfarjani, and G. Chen, "Hydrodynamic phonon transport in suspended graphene," *Nature Communications*, vol. 6, p. 6290, 2015.

[86] L. Landau and E. Lifshitz, *Theory of Elasticity*. Pergamon Press, 1986.

[87] R. Wallis, "Lattice dynamics of crystal surfaces," *Prog. Surf. Sci.*, vol. 4, pp. 233–367, 1974.

[88] R. Wallis, "Surface phonons: theoretical developments," *Surf. Sci.*, vol. 299-300, pp. 612–627, 1994.

[89] W.-X. Li, K.-Q. Chen, W. Duan, J. Wu, and B.-L. Gu, "Acoustic phonon transport through a T-shaped quantum waveguide," *J. Phys. Condens. Matter*, vol. 17, no. 28, p. 5049, 2014.

[90] J. Hyun Oh, M.-G. Jang, M. Shin, and S.-H. Lee, "Phonon transport in Si nanowires with elastically dissimilar barriers," *Appl. Phys. Lett.*, vol. 100, no. 11, p. 113110, 2012.

[91] A. A. Maznev, "Boundary scattering of phonons: Specularity of a randomly rough surface in the small-perturbation limit," *Phys. Rev. B*, vol. 91, p. 134306, Apr 2015.

[92] W. Li, H. Sevinçli, G. Cuniberti, and S. Roche, "Phonon transport in large scale carbon-based disordered materials: Implementation of an efficient order-N and real-space Kubo methodology," *Phys. Rev. B*, vol. 82, p. 041410, Jul 2010.

[93] H. Sevinçli and G. Cuniberti, "Enhanced thermoelectric figure of merit in edge-disordered zigzag graphene nanoribbons," *Phys. Rev. B*, vol. 81, p. 113401, Mar 2010.

[94] W. J. Evans, L. Hu, and P. Keblinski, "Thermal conductivity of graphene ribbons from equilibrium molecular dynamics: Effect of ribbon width, edge roughness, and hydrogen termination," *Appl. Phys. Lett.*, vol. 96, no. 20, p. 203112, 2010.

[95] L. Rayleigh, "On Waves Propagated along the Plane Surface of an Elastic Solid," *P. Lond. Math Soc.*, vol. s1-17, no. 1, pp. 4–11, 1885.

[96] J. L. Feldman, M. D. Kluge, P. B. Allen, and F. Wooten, "Thermal conductivity and localization in glasses: Numerical study of a model of amorphous silicon," *Phys. Rev. B*, vol. 48, pp. 12589–12602, Nov 1993.

[97] J. Chen, G. Zhang, and B. Li, "Remarkable Reduction of Thermal Conductivity in Silicon Nanotubes," *Nano Letters*, vol. 10, no. 10, pp. 3978–3983, 2010.

[98] S. Russ and Y. Hlushchuk, "Localized low-frequency Neumann modes in 2d systems with rough boundaries," *Europhys. Lett.*, vol. 67, no. 1, p. 70, 2004.

[99] L. M. Brekhovskikh, *Waves in Layered Media*. Academic Press, 1980.

[100] J. P. Wolfe, *Imaging Phonons*. Cambridge University Press, 1998.

[101] R. Snieder, "General Theory of Elastic Wave Scattering," in *Scattering* (P. Sabatier and R. Pike, eds.), pp. 528–542, London: Academic Press, 2002.

[102] O. Dubay and G. Kresse, "Accurate density functional calculations for the phonon dispersion relations of graphite layer and carbon nanotubes," *Phys. Rev. B*, vol. 67, p. 035401, Jan 2003.

[103] A. Kambili, G. Fagas, V. I. Fal'ko, and C. J. Lambert, "Phonon-mediated thermal conductance of mesoscopic wires with rough edges," *Phys. Rev. B*, vol. 60, pp. 15593–15596, Dec 1999.

[104] D. H. Santamore and M. C. Cross, "Effect of surface roughness on the universal thermal conductance," *Phys. Rev. B*, vol. 63, p. 184306, Apr 2001.

[105] M. C. Cross and R. Lifshitz, "Elastic wave transmission at an abrupt junction in a thin plate with application to heat transport and vibrations in mesoscopic systems," *Phys. Rev. B*, vol. 64, p. 085324, Aug 2001.

[106] A. N. Cleland, D. R. Schmidt, and C. S. Yung, "Thermal conductance of nanostructured phononic crystals," *Phys. Rev. B*, vol. 64, p. 172301, Oct 2001.

[107] X. F. Wang, M. S. Kushwaha, and P. Vasilopoulos, "Tunability of acoustic spectral gaps and transmission in periodically stubbed waveguides," *Phys. Rev. B*, vol. 65, p. 035107, Dec 2001.

[108] S.-X. Qu and M. R. Geller, "Mesoscopic electron and phonon transport through a curved wire," *Phys. Rev. B*, vol. 70, p. 085414, Aug 2004.

[109] L. Wen-Xia, L. Tian-Yu, and L. Chang-Long, "Acoustic Phonon Thermal Transport through a Nanostructure," *Chinese Phys. Lett.*, vol. 23, no. 9, p. 2522, 2006.

[110] W. Li and K. Chen, "Phonon heat transport through periodically stubbed waveguides," *Phys. Lett. A*, vol. 357, no. 4-5, pp. 378–383, 2006.

[111] L.-M. Tang, L. Wang, W.-Q. Huang, B. S. Zou, and K.-Q. Chen, "Acoustic phonon transport and thermal conductance in a periodically modulated quantum wire," *J. Phys. D: Appl. Phys.*, vol. 40, no. 5, p. 1497, 2007.

[112] H.-Y. Zhang, H.-J. Li, W.-Q. Huang, and S.-X. Xie, "Acoustic phonon transport through a quantum waveguide with two stubs," *J. Phys. D: Appl. Phys.*, vol. 40, no. 19, p. 6105, 2007.

[113] Y. Wang, L.-L. Wang, L.-M. Tang, B. Zou, and L.-H. Zhao, "The influence of flaws on phonon thermal conductance in a dielectric quantum wire," *J. Phys. D: Appl. Phys.*, vol. 40, no. 22, p. 7159, 2007.

[114] L. Lindsay, D. A. Broido, and N. Mingo, "Flexural phonons and thermal transport in graphene," *Phys. Rev. B*, vol. 82, p. 115427, Sep 2010.

[115] D. A. Broido, A. Ward, and N. Mingo, "Lattice thermal conductivity of silicon from empirical interatomic potentials," *Phys. Rev. B*, vol. 72, p. 014308, Jul 2005.

[116] D. L. Nika, S. Ghosh, E. P. Pokatilov, and A. A. Balandin, "Lattice thermal conductivity of graphene flakes: Comparison with bulk graphite," *Appl. Phys. Lett.*, vol. 94, no. 20, p. 203103, 2009.

[117] D. L. Nika, E. P. Pokatilov, A. S. Askerov, and A. A. Balandin, "Phonon thermal conduction in graphene: Role of umklapp and edge roughness scattering," *Phys. Rev. B*, vol. 79, p. 155413, Apr 2009.

[118] N. Bonini, J. Garg, and N. Marzari, "Acoustic Phonon Lifetimes and Thermal Transport in Free-Standing and Strained Graphene," *Nano Lett.*, vol. 12, no. 6, pp. 2673–2678, 2012.

[119] Z. Aksamija and I. Knezevic, "Lattice thermal conductivity of graphene nanoribbons: Anisotropy and edge roughness scattering," *Appl. Phys. Lett.*, vol. 98, no. 14, p. 141919, 2011.

[120] A. V. Savin and Y. S. Kivshar, "Vibrational tamm states at the edges of graphene nanoribbons," *Phys. Rev. B*, vol. 81, p. 165418, Apr 2010.

[121] Y. Ni, Y. A. Kosevich, S. Xiong, Y. Chalopin, and S. Volz, "Substrate-induced cross-plane thermal propagative modes in few-layer graphene," *Phys. Rev. B*, vol. 89, p. 205413, May 2014.

[122] K. Yee, "Numerical solution of initial boundary value problems involving maxwell's equations in isotropic media," *IEEE T. Antenn. Propag.*, vol. 14, pp. 302–307, May 1966.

[123] A. Taflove and S. C. Hagness, *Computational Electrodynamics: The Finite-Difference Time-Domain Method*. Artech House, 2005.

[124] H. F. Harmuth, "On the solution of the Schrödinger and the Klein Gordon equations by digital computers," *Journal of Mathematics and Physics*, vol. 36, pp. 269–278, 1957.

[125] D. M. Sullivan and P. M. Wilson, "Time-domain determination of transmission in quantum nanostructures," *J. Appl. Phys.*, vol. 112, no. 6, p. 064325, 2012.

[126] J. Virieux, "SH-wave propagation in heterogeneous media: Velocity-stress finite-difference method," *Geophysics*, vol. 49, no. 11, pp. 1933–1942, 1984.

[127] Z. Alterman and F. C. Karal, "Propagation of elastic waves in layered media by finite difference methods," *Bull. Seismol. Soc. Am.*, vol. 58, no. 1, pp. 367–398, 1968.

[128] J. Virieux, "P-SV wave propagation in heterogeneous media: Velocity-stress finite-difference method," *Geophysics*, vol. 51, no. 4, pp. 889–901, 1986.

[129] H. Kato and S.-i. Tamura, "Anomalous transmission of phonons in superlattices at oblique propagation: an analysis based on finite difference equations," *J. Phys. Condens. Matter*, vol. 9, no. 32, p. 6791, 1997.

[130] M. M. Sigalas and N. García, "Theoretical study of three dimensional elastic band gaps with the finite-difference time-domain method," *J. Appl. Phys.*, vol. 87, no. 6, pp. 3122–3125, 2000.

[131] D. Garcia-Pablos, M. Sigalas, F. R. Montero de Espinosa, M. Torres, M. Kafesaki, and N. García, "Theory and Experiments on Elastic Band Gaps," *Phys. Rev. Lett.*, vol. 84, pp. 4349–4352, May 2000.

[132] J. O. Vasseur, P. A. Deymier, B. Chenni, B. Djafari-Rouhani, L. Dobrzynski, and D. Prevost, "Experimental and Theoretical Evidence for the Existence of Absolute Acoustic Band Gaps in Two-Dimensional Solid Phononic Crystals," *Phys. Rev. Lett.*, vol. 86, pp. 3012–3015, Apr 2001.

[133] A. R. Levander, "Fourth-order finite-difference P-SV seismograms," *Geophysics*, vol. 53, no. 11, pp. 1425–1436, 1988.

[134] K. V. Zakharchenko, M. I. Katsnelson, and A. Fasolino, "Finite Temperature Lattice Properties of Graphene beyond the Quasiharmonic Approximation," *Phys. Rev. Lett.*, vol. 102, p. 046808, Jan 2009.

[135] J.-W. Jiang, J.-S. Wang, and B. Li, "Young's modulus of graphene: A molecular dynamics study," *Phys. Rev. B*, vol. 80, p. 113405, Sep 2009.

[136] Z. Guo, D. Zhang, and X.-G. Gong, "Thermal conductivity of graphene nanoribbons," *Appl. Phys. Lett.*, vol. 95, no. 16, p. 163103, 2009.

[137] J. Hu, X. Ruan, and Y. P. Chen, "Thermal Conductivity and Thermal Rectification in Graphene Nanoribbons: A Molecular Dynamics Study," *Nano Lett.*, vol. 9, no. 7, pp. 2730–2735, 2009. PMID: 19499898.

[138] Z. Wei, Y. Chen, and C. Dames, "Wave packet simulations of phonon boundary scattering at graphene edges," *J. Appl. Phys.*, vol. 112, no. 2, p. 024328, 2012.

[139] C. Zeng, J. Xia, R. D. Miller, and G. P. Tsoflias, "An improved vacuum formulation for 2D finite-difference modeling of Rayleigh waves including surface topography and internal discontinuities," *Geophysics*, vol. 77, no. 1, pp. T1–T9, 2012.

[140] R. W. Graves, "Simulating seismic wave propagation in 3D elastic media using staggered-grid finite differences," *Bull. Seismol. Soc. Am.*, vol. 86, no. 4, pp. 1091–1106, 1996.

[141] K. R. Kelly, R. W. Ward, S. Treitel, and R. M. Alford, "Synthetic Seismograms: A Finite-Difference Approach," *Geophysics*, vol. 41, no. 1, pp. 2–27, 1976.

[142] R. Stacey, "New finite-difference methods for free surfaces with a stability analysis," *Bull. Seismol. Soc. Am.*, vol. 84, no. 1, pp. 171–184, 1994.

[143] G. P. Tsoflias and C. Zeng. (private communication).

[144] H. Igel, P. Mora, and B. Riollet, "Anisotropic wave propagation through finitedifference grids," *Geophysics*, vol. 60, no. 4, pp. 1203–1216, 1995.

[145] M. Sato, "Diagonally Staggered Grid for the Analysis of Elastic Wave Fields in Isotropic and Anisotropic Solids Using the Finite-Difference Time-Domain Method," *Jpn. J. Appl. Phys.*, vol. 47, no. 5S, p. 3931, 2008.

[146] J. P. Feser, J. S. Sadhu, B. P. Azeredo, K. H. Hsu, J. Ma, J. Kim, M. Seong, N. X. Fang, X. Li, P. M. Ferreira, S. Sinha, and D. G. Cahill, "Thermal conductivity of silicon nanowire arrays with controlled roughness," *J. Appl. Phys.*, vol. 112, no. 11, p. 114306, 2012.

[147] N. Mingo, "Calculation of Si nanowire thermal conductivity using complete phonon dispersion relations," *Phys. Rev. B*, vol. 68, p. 113308, Sep 2003.

[148] C. Bera, "Monte Carlo simulation of thermal conductivity of Si nanowire: An investigation on the phonon confinement effect on the thermal transport," *J. Appl. Phys.*, vol. 112, no. 7, 2012.

[149] Y. Chen, D. Li, J. R. Lukes, and A. Majumdar, "Monte Carlo simulation of silicon nanowire thermal conductivity," *J. Heat Transfer*, vol. 127, no. 10, pp. 1129–1137, 2005.

[150] Y.-R. Chen, M. S. Jeng, Y. W. Chou, and C. C. Yang, "Molecular dynamics simulation of the thermal conductivities of Si nanowires with various roughnesses," *Computational Materials Science*, vol. 50, no. 6, pp. 1932 – 1936, 2011.

[151] F. Sansoz, "Surface faceting dependence of thermal transport in silicon nanowires," *Nano Letters*, vol. 11, no. 12, pp. 5378–5382, 2011.

[152] D. Donadio and G. Galli, "Atomistic simulations of heat transport in silicon nanowires," *Phys. Rev. Lett.*, vol. 102, p. 195901, May 2009.

[153] F. X. Alvarez, D. Jou, and A. Sellitto, "Phonon boundary effects and thermal conductivity of rough concentric nanowires," *J. Heat Transfer*, vol. 133, no. 2, p. 022402, 2011.

[154] A. L. Moore, S. K. Saha, R. S. Prasher, and L. Shi, "Phonon backscattering and thermal conductivity suppression in sawtooth nanowires," *Appl. Phys. Lett.*, vol. 93, no. 8, p. 083112, 2008.

[155] Z. Wang, Z. Ni, R. Zhao, M. Chen, K. Bi, and Y. Chen, "The effect of surface roughness on lattice thermal conductivity of silicon nanowires," *Physica B*, vol. 406, no. 13, pp. 2515 – 2520, 2011.

[156] C. Blanc, A. Rajabpour, S. Volz, T. Fournier, and O. Bourgeois, "Phonon heat conduction in corrugated silicon nanowires below the Casimir limit," *Appl. Phys. Lett.*, vol. 103, no. 4, p. 043109, 2013.

[157] J. S. Heron, T. Fournier, N. Mingo, and O. Bourgeois, "Mesoscopic size effects on the thermal conductance of silicon nanowire," *Nano Letters*, vol. 9, no. 5, pp. 1861–1865, 2009.

[158] D. L. Nika, A. I. Cocemasov, C. I. Isacova, A. A. Balandin, V. M. Fomin, and O. G. Schmidt, "Suppression of phonon heat conduction in cross-section-modulated nanowires," *Phys. Rev. B*, vol. 85, p. 205439, May 2012.

[159] J. Carrete, L. J. Gallego, L. M. Varela, and N. Mingo, "Surface roughness and thermal conductivity of semiconductor nanowires: Going below the casimir limit," *Phys. Rev. B*, vol. 84, p. 075403, Aug 2011.

[160] P. G. Murphy and J. E. Moore, "Coherent phonon scattering effects on thermal transport in thin semiconductor nanowires," *Phys. Rev. B*, vol. 76, p. 155313, Oct 2007.

[161] R. Chen, A. I. Hochbaum, P. Murphy, J. Moore, P. Yang, and A. Majumdar, "Thermal conductance of thin silicon nanowires," *Phys. Rev. Lett.*, vol. 101, p. 105501, Sep 2008.

[162] M. G. Ghossoub, K. V. Valavala, M. Seong, B. Azeredo, K. Hsu, J. S. Sadhu, P. K. Singh, and S. Sinha, "Spectral phonon scattering from sub-10 nm surface roughness wavelengths in metal-assisted chemically etched Si nanowires," *Nano Letters*, vol. 13, no. 4, pp. 1564–1571, 2013.

[163] Y. S. Ju and K. E. Goodson, "Phonon scattering in silicon films with thickness of order 100 nm," *Appl. Phys. Lett.*, vol. 74, no. 20, pp. 3005–3007, 1999.

[164] E. Pop, R. W. Dutton, and K. E. Goodson, "Analytic band Monte Carlo model for electron transport in Si including acoustic and optical phonon dispersion," *J. Appl. Phys.*, vol. 96, no. 9, pp. 4998–5005, 2004.

[165] P. W. Anderson, "Absence of diffusion in certain random lattices," *Phys. Rev.*, vol. 109, pp. 1492–1505, Mar 1958.

[166] N. F. Mott, "Conduction in non-crystalline materials," *Philos. Mag.*, vol. 19, pp. 835–852, 1969.

[167] N. Apsley and H. P. Hughes, "Temperature-and field-dependence of hopping conduction in disordered systems," *Philos. Mag.*, vol. 30, pp. 963–972, 1974.

[168] S. Troubetzkoy, "Complexity lower bounds for polygonal billiards," *Chaos*, vol. 8, no. 1, pp. 242–244, 1998.

[169] G. D. Mahan, *Condensed Matter in a Nutshell*. Princeton University Press, 2011.

[170] R. G. Steg and P. G. Klemens, "Scattering of Rayleigh Waves by Surface Irregularities," *Phys. Rev. Lett.*, vol. 24, pp. 381–383, Feb 1970.

[171] T. Sakuma, "Elastic-Surface-Wave Scattering from Point-Mass Defects in a Solid Surface," *Phys. Rev. B*, vol. 8, pp. 1433–1440, Aug 1973.

[172] A. N. Darinskii, M. Weihnacht, and H. Schmidt, "Rayleigh wave reflection from single surface imperfections on isotropic substrates," *J. Appl. Phys.*, vol. 106, no. 3, p. 034914, 2009.

[173] A. Darinskii, M. Weihnacht, and H. Schmidt, "Mutual conversion of bulk and surface acoustic waves in gratings of finite length on half-infinite substrates. I. {FE} analysis of surface wave generation," *Ultrasonics*, vol. 53, no. 5, pp. 998–1003, 2013.

[174] A. Darinskii, M. Weihnacht, and H. Schmidt, "Mutual conversion of bulk and surface acoustic waves in gratings of finite length on half-infinite substrates. II. {FE} analysis of bulk wave generation," *Ultrasonics*, vol. 53, no. 5, pp. 1004–1011, 2013.

[175] Y. A. Kosevich and A. V. Savin, "Reduction of phonon thermal conductivity in nanowires and nanoribbons with dynamically rough surfaces and edges," *Europhys. Lett.*, vol. 88, no. 1, p. 14002, 2009.

[176] D. Donadio and G. Galli, "Temperature Dependence of the Thermal Conductivity of Thin Silicon Nanowires," *Nano Letters*, vol. 10, no. 3, pp. 847–851, 2010. PMID: 20163124.

[177] M. Hu, K. P. Giapis, J. V. Goicochea, X. Zhang, and D. Poulikakos, "Significant Reduction of Thermal Conductivity in Si/Ge CoreShell Nanowires," *Nano Letters*, vol. 11, no. 2, pp. 618–623, 2011.

[178] W. Lv and A. Henry, "Direct calculation of modal contributions to thermal conductivity via Green–Kubo modal analysis," *New J. Phys.*, vol. 18, no. 1, p. 013028, 2016.

[179] M.-H. Bae, Z. Li, Z. Aksamija, P. N. Martin, F. Xiong, Z.-Y. Ong, I. Knezevic, and E. Pop, "Ballistic to diffusive crossover of heat flow in graphene ribbons," *Nat. Commun.*, vol. 4, p. 1734, 2012.

[180] Z. Wang and N. Mingo, "Absence of casimir regime in two-dimensional nanoribbon phonon conduction," *Appl. Phys. Lett.*, vol. 99, no. 10, p. 101903, 2011.

[181] B. Li, H. Zhao, and B. Hu, "Can disorder induce a finite thermal conductivity in 1d lattices?," *Phys. Rev. Lett.*, vol. 86, pp. 63–66, Jan 2001.

[182] A. Dhar, "Heat transport in low-dimensional systems," *Adv. Phys.*, vol. 57, no. 5, pp. 457–537, 2008.

[183] S. Lepri, R. Livi, and A. Politi, "On the anomalous thermal conductivity of one-dimensional lattices," *Europhys. Lett.*, vol. 43, no. 3, p. 271, 1998.

[184] L. Yang, "Finite heat conduction in a 2d disorder lattice," *Phys. Rev. Lett.*, vol. 88, p. 094301, Feb 2002.

[185] B. Hu, B.-Q. Jin, L. Wang, and H. Yang, "Comment on "finite heat conduction in a 2d disorder lattice"," *Phys. Rev. Lett.*, vol. 90, p. 119401, Mar 2003.

[186] L. W. Lee and A. Dhar, "Heat conduction in a two-dimensional harmonic crystal with disorder," *Phys. Rev. Lett.*, vol. 95, p. 094302, Aug 2005.

[187] R. Weaver and O. Lobkis, "Anderson localization in coupled reverberation rooms," *J. Sound Vibration*, vol. 231, no. 4, pp. 1111–1134, 2000.

[188] R. Weaver, "Mesoscopics in acoustics," in *New Directions in Linear Acoustics and Vibration* (M. Wright and R. Weaver, eds.), pp. 123–130, Cambridge: Cambridge University Press, 2010.

[189] L. N. Maurer and I. Knezevic, "Chaos vs disorder in phonon dynamics at the nanoscale," in prep. (2016).

[190] J. E. Graebner, M. E. Reiss, L. Seibles, T. M. Hartnett, R. P. Miller, and C. J. Robinson, "Phonon scattering in chemical-vapor-deposited diamond," *Phys. Rev. B*, vol. 50, pp. 3702–3713, Aug 1994.

[191] J. A. Ogilvy, "Theoretical comparison of ultrasonic signal amplitudes from smooth and rough defects," *NDT International*, vol. 19, no. 6, pp. 371–385, 1986.

[192] S.-Z. Zhang, E. Louis, E. Cuevas, and J. A. Vergés, "Chaotic dynamics in an elastic medium with surface disorder," *Phys. Rev. E*, vol. 56, pp. 4125–4129, Oct 1997.

[193] F. D. Hastings, J. B. Schneider, and S. L. Broschat, "Application of the perfectly matched layer (PML) absorbing boundary condition to elastic wave propagation," *J. Acoust. Soc. Am.*, vol. 100, no. 5, pp. 3061–3069, 1996.

[194] A. Alcázar-López and J. A. Méndez-Bermúdez, "Disorder-to-chaos transition in the conductance distribution of corrugated waveguides," *Phys. Rev. E*, vol. 87, p. 032904, Mar 2013.